Fiber tracking uncertainty visualization for neurosurgery

Siddiqui, F.P.

DOI
10.4233/uuid:26158a6d-3f2e-4ec8-a2f1-f32fe0e4add4

Publication date
2025

Document Version
Final published version

Citation (APA)
Siddiqui, F. P. (2025). *Fiber tracking uncertainty visualization for neurosurgery*. [Dissertation (TU Delft), Delft University of Technology]. https://doi.org/10.4233/uuid:26158a6d-3f2e-4ec8-a2f1-f32fe0e4add4

FIBER TRACKING UNCERTAINTY VISUALIZATION FOR NEUROSURGERY

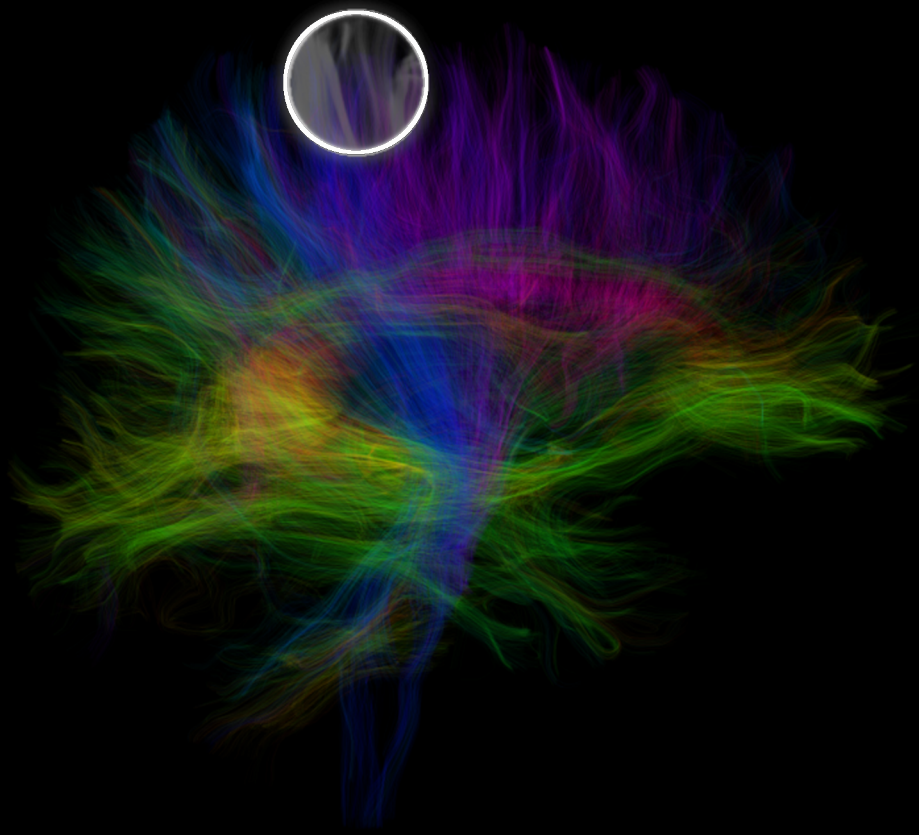

Faizan Pervez Siddiqui

FIBER TRACKING UNCERTAINTY VISUALIZATION FOR NEUROSURGERY

FIBER TRACKING UNCERTAINTY VISUALIZATION FOR NEUROSURGERY

Dissertation

for the purpose of obtaining the degree of doctor
at Delft University of Technology
by the authority of the Rector Magnificus, prof. dr. ir. T.H.J.J. van der Hagen,
chair of the Board for Doctorates
to be defended publicly on
Tuesday 9 September 2025 at 15:00 o'clock

by

Faizan Pervez SIDDIQUI

Master of Science in Electrical and Electronics Engineering,
Özyeğin Üniversitesi, Türkiye
born in Karachi, Pakistan.

This dissertation has been approved by the promotors.

Composition of the doctoral committee:

Rector Magnificus,	chairperson
Prof. dr. A. Vilanova Bartroli,	Delft University of Technology / Eindhoven University of Technology, *promotor*
Prof. dr. E. Eisemann,	Delft University of Technology, *promotor*
Dr. T. Höllt,	Delft University of Technology, *copromotor*
Independent members:	
Prof. dr. B.P.F Lelieveldt,	Delft University of Technology
Prof. dr. I. Hotz,	Linköping University, Sweden
Prof. dr. T. Schultz,	University of Bonn, Germany
Dr. F. M. Vos,	Delft University of Technology

This research was conducted at TU Delft and ASCI Graduate School.
It was part of the research program *"Diffusion MRI Tractography with Uncertainty Propagation for the Neurosurgical Workflow"*, project number 16338, funded (partially) by the Netherlands Organization for Scientific Research (NWO).

This work was carried out in collaboration with Eindhoven University of Technology and the Elisabeth-TweeSteden Hospital.

Keywords: Fiber Tracking, Uncertainty Visualization, Diffusion MRI, Neurosurgical Planning

Printed by: ...

Cover by: ...

ISBN 000-00-0000-000-0

An electronic copy of this dissertation is available at
https://repository.tudelft.nl/.

Contents

SUMMARY

Fiber tracking enables the in-vivo reconstruction of white matter pathways in the brain and has significant potential in clinical workflows such as neurosurgical planning. However, its broader clinical adoption remains limited due to the high degree of uncertainty that arises throughout the processing pipeline, from diffusion MRI acquisition to modeling, tracking, and visualization. These uncertainties are rarely communicated in current clinical visualizations, which often present results as definitive, potentially misleading clinicians and affecting critical decisions.

This thesis explores the integration of fiber tracking uncertainty visualization into neurosurgical workflow, aiming to enhance the interpretability and transparency of the results in a clinical context. A key challenge lies in balancing computational complexity with clear representation, while ensuring the solutions remain aligned with clinical workflows.

To address this, we introduce interactive and computationally efficient visualization approaches that represent uncertainties and support clinicians in understanding how fiber tracking results may vary with inherent uncertainties. These techniques are evaluated through collaborations with medical experts and incorporated into decision-making studies to assess their practical relevance.

The contributions presented in this thesis advance the integration of uncertainty into clinical fiber tracking visualization and highlight how embracing uncertainty, rather than ignoring it, can lead to safer and more informed clinical decisions.

SAMENVATTING

Fiber tracking maakt het mogelijk om de witte stofbanen in de hersenen in vivo te reconstrueren en biedt daarmee belangrijke mogelijkheden binnen klinische toepassingen, zoals neurochirurgische planning. De brede klinische toepassing blijft echter beperkt door de aanzienlijke onzekerheden die optreden in de gehele verwerkingspijplijn—van diffusie-MRI-acquisitie tot modellering, tracking en visualisatie. Deze onzekerheden worden zelden gecommuniceerd in de huidige visualisaties, die de resultaten vaak als eenduidig presenteren. Dit kan artsen misleiden en invloed hebben op cruciale beslissingen.

Dit proefschrift richt zich op de integratie van onzekerheidsvisualisatie binnen fiber tracking in de neurochirurgische workflow, met als doel de interpretatie en transparantie van de resultaten in een klinische context te verbeteren. Een belangrijke uitdaging hierbij is het vinden van een balans tussen computationele complexiteit en heldere representatie, terwijl aansluiting bij bestaande klinische processen behouden blijft.

Om deze uitdaging aan te pakken, introduceren we interactieve en computationeel efficiënte visualisatietechnieken die onzekerheden expliciet maken. Deze ondersteunen clinici bij het begrijpen van hoe fiber tracking-resultaten kunnen variëren als gevolg van onzekerheden in de modellering en parameterkeuzes. De ontwikkelde technieken zijn geëvalueerd in samenwerking met medische experts en zijn opgenomen in besluitvormingsstudies om hun klinische relevantie te toetsen.

De bijdragen van dit proefschrift bevorderen de integratie van onzekerheidsinformatie in de visualisatie van witte stof en onderstrepen hoe het expliciet maken van ambiguïteit, in plaats van deze te negeren, kan bijdragen aan veiligere en beter onderbouwde klinische besluitvorming.

1

INTRODUCTION

Recent advancements in Magnetic Resonance Imaging (MRI) technology have led to the development of various remarkable techniques for interpreting brain anatomy. Among these, Diffusion-Weighted Imaging (DWI) has emerged as a key non-invasive technique for assessing brain white matter connectivity. White matter, consisting of bundles of myelinated axons, serves as the communication network of the brain, facilitating the transfer of information between different regions.

DWI exploits the anisotropic diffusion of water molecules to map the orientation of these white matter structures. The imaging and interpretation of molecular diffusion have advanced significantly with the development of the modeling techniques such as Diffusion Tensor Imaging (DTI), Diffusion Spectrum Imaging (DSI), Q-Ball Imaging (QBI) which provide deeper insights into white matter architecture. Among these, DTI allows direct in-vivo examination of the fibrous structure in the brain at a relatively low acquisition cost. This makes DTI particularly suitable for clinical applications, where it is valuable in visualizing structural connectivity in the brain and supporting the diagnosis of neurological conditions.

Diffusion Tensor Imaging, as any other measurement, is inherently susceptible to uncertainties across its processing pipeline—from MRI data acquisition to diffusion modeling, and visualization. These uncertainties can arise from various factors, such as noise in the data, the limitations of the tensor model, inaccuracies in fiber tracking algorithms, and challenges in visualizing complex fiber structures. Due to the complexity of the pipeline, it is often difficult for users to pinpoint the sources of errors. Addressing these uncertainties is particularly critical in clinical contexts, where precise and reliable information is vital for decision-making. This thesis explores the role of uncertainty visualization in white matter, with a specific focus on the neurosurgical workflow.

Traditional representations of DTI often fail to convey the inherent uncertainties, instead presenting the results as definitive truths. This lack of information can mislead clinicians and influence critical decisions. White matter visualization is crucial in clinical contexts, such as surgical planning for tumor resection. To enhance decision-making,

incorporating uncertainty visualization can ensure that clinicians are aware of the inherent risks and ambiguities in the data. The absence of uncertainty representation in standard white matter visualizations means that clinicians are often unaware of the reliability or potential errors in the data, making it difficult to fully assess the risks associated with their decisions. The visualization of uncertainty can provide a more transparent and informed view of the data, making it possible for clinicians to assess the confidence in the results and adapt their decisions accordingly.

The motivation behind this thesis is to bridge the gap between the technical advances in uncertainty visualization and their practical application in clinical settings. By addressing the challenges associated with uncertainty visualization in DTI pipeline and offering effective visualization solutions, this work seeks to contribute to safer and more informed clinical decision-making processes.

Several state-of-the-art reports exist on DWI visualization, [5, 7, 8, 9]. However, none of them gives an overview of uncertainty, or they simply focus on some specific aspects. Furthermore, most of the visualization literature on uncertainty focuses on issues related to visual representation rather than sources of error involved in the pipeline [3, 4, 7]. Moreover, the explicit visualization of uncertainty, particularly tailored to the clinical workflow, remains largely under explored. Without clear and intuitive ways to visualize the uncertainty in the results, clinicians may make decisions without an accurate understanding of the inherent errors. Some techniques have also been introduced in the literature specifically addressing the uncertainty visualization in DWI, [1, 2, 6]. However, the significant computational resources required to implement these methods effectively in a clinical setting pose a major challenge. This often makes them unsuitable for real-time applications and integration into clinical workflows. Addressing the entire DWI pipeline cohesively remains a challenge.

Even when uncertainty is incorporated into the visualization, interpreting it effectively poses a significant challenge. Clinicians may struggle to understand or integrate the uncertainty information into their decision-making processes, particularly when traditional representations fail to contextualize these ambiguities within the broader clinical workflow. Misinterpretations of uncertainty can compromise the reliability of critical decisions.

The aim of this thesis is to address these challenges by focusing on the development of uncertainty visualization techniques specifically tailored to the clinical DTI pipeline. By integrating uncertainty visualization into the standard workflow, this work aspires to enhance the interpretability of uncertainty, making it a part of clinical practice rather than an overlooked aspect. Ultimately, this research seeks to bridge the gap between technical advancements in uncertainty visualization and practical clinical applications.

In this thesis the research begins with a literature review of existing uncertainty visualization techniques for both DTI and non-DTI methods. This review identifies various sources of error at each stage of the pipeline and examines their impact on the resulting visualizations and interpretations. This foundation study leads to the development of innovative uncertainty visualization techniques aimed at enhancing the visual representation of the uncertainty in DTI and their integration of uncertainty into clinical workflows. The first core study focuses on addressing computational cost for modeling and visualizing uncertainty. It introduces a progressive visualization approach that facil-

itates addressing the computational costs, enabling uncertainty computations to occur in the background while providing users with an interactive interface to explore and interpret uncertainty in real time. The uncertainty quantification and visualizations are adapted to handle the progressiveness of the solution. This combination of computational efficiency and interactivity can help in incorporating uncertainty visualization into standard clinical DTI pipelines.

The second study investigates the uncertainty that arises due to the sensitivity of the fiber tracking parameters. It introduces sensitivity maps to highlight regions where fiber tracking results exhibit high uncertainty, providing clinicians with actionable insights to optimize the placement of regions of interest. This study also prioritizes computational efficiency, facilitating real-time analysis potentially in clinical environments.

These techniques provide representations of uncertainties involved in different stages of the DTI pipeline, enhancing clinicians' understanding of potential errors and ambiguities in DTI results. Feedback from clinicians played a crucial role in refining these techniques and ensuring their practical relevance. Following these studies, an evaluation was conducted to assess the impact of uncertainty visualization on clinical decision-making processes during neurosurgical procedures.The primary objective of this study was to assess the impact of uncertainty visualization on clinical decision-making. Conducted in collaboration with neurosurgeons and researchers, the study involved presenting participants with an interactive questionnaire containing a series of clinical questions. The findings highlight that integrating uncertainty visualization into the neurosurgical workflow influences clinical decision-making. However, other factors that also impact clinical decisions were not considered in this study.

The development of these uncertainty visualization techniques was guided by a thorough understanding of the practical requirements and constraints of the clinical neurosurgical workflow. The studies were carried out in close collaboration with our clinical partners, including neurosurgeons, clinicians, and researchers, ensuring that the techniques were both relevant and applicable to real-world clinical workflow and decision-making scenarios. By addressing the gap between processing and visualization techniques and their practical application in clinical settings, this work contributes to making uncertainty information accessible and actionable for clinicians.

This thesis is structured to systematically address the background, challenges and advancements in uncertainty visualization within the context of diffusion tensor imaging (DTI). The thesis is organized as follows:

Chapters 2 and 3 provide the foundation. Chapter 2 covers the Medical Background, including brain anatomy and clinical applications of DTI. Chapter 3 explains the technical background, detailing the DTI pipeline. Chapters 4, 5, 6, and 7 present the core research. Chapter 4 focuses on Uncertainty in DTI, discussing sources of uncertainty, uncertainty modeling, and visualization techniques. Chapter 5 introduces a Progressive Approach for uncertainty visualization and a visual analytics pipeline. Chapter 6 explores Interactive Visualization of Sensitivities in fiber tracking. Chapter 7 examines the Impact of Uncertainty Visualization on Neurosurgical Decision-Making, based on clinical feedback. Finally, Chapter 8 summarizes the main contributions of the thesis and outlines potential directions for future research.

1

REFERENCES

[1] Ralph Brecheisen et al. “Illustrative uncertainty visualization of DTI fiber pathways”. In: *The Visual Computer* 29.4 (2013), pp. 297–309.

[2] Frank Enders et al. *Visualization of white matter tracts with wrapped streamlines*. IEEE, 2005.

[3] Mathias Goldau and Mario Hlawitschka. “Multi-modal visualization of probabilistic tractography”. In: *Visualization in Medicine and Life Sciences III*. Springer, 2016, pp. 195–218.

[4] Tobias Isenberg. “A survey of illustrative visualization techniques for diffusion-weighted MRI tractography”. In: *Visualization and Processing of Higher Order Descriptors for Multi-Valued Data*. Springer, 2015, pp. 235–256.

[5] ALEXANDER Leemans. “Visualization of diffusion MRI data”. In: *Diffusion MRI* (2010), pp. 354–379.

[6] Thomas Schultz, Holger Theisel, and Hans-Peter Seidel. “Topological visualization of brain diffusion MRI data”. In: *IEEE Transactions on Visualization and Computer Graphics* 13.6 (2007), pp. 1496–1503.

[7] Thomas Schultz and Anna Vilanova. “Diffusion MRI visualization”. In: *NMR in Biomedicine* 32.4 (2019), e3902.

[8] Thomas Schultz et al. “Fuzzy fibers: Uncertainty in dMRI tractography”. In: *Scientific Visualization*. Springer, 2014, pp. 79–92.

[9] Anna Vilanova et al. “An introduction to visualization of diffusion tensor imaging and its applications”. In: *Visualization and Processing of Tensor Fields*. Springer, 2006, pp. 121–153.

2

Medical Background

This chapter provides a background on basic concepts to understand the clinical significance of DTI. We will begin by exploring the anatomy of the brain, with a particular focus on white matter, its structure, and its crucial role in various cognitive functions. Following this, we will delve into the clinical applications of DTI, with an emphasis on its role in neurosurgery.

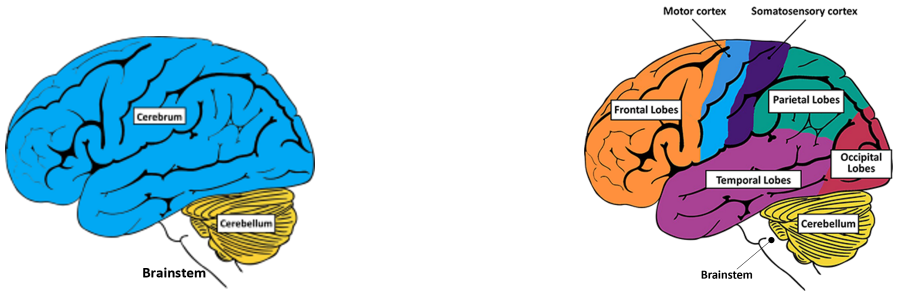

(a) (b)

Figure 2.1: Structural organization of the brain [2].

2.1. BRAIN ANATOMY

The human brain is a complex organ composed of various structures that work together to support a wide range of functions. This section provides a brief overview of the brain's anatomical structure.

2.1.1. STRUCTURAL OVERVIEW OF THE BRAIN

Structurally, human brain is broadly divided into three main regions: the cerebrum, cerebellum, and the brainstem, as shown in Figure 2.1a.

- The **cerebrum** is the largest part, responsible for higher cognitive functions such as reasoning, problem-solving, and emotional regulation. It is split into two hemispheres connected by the corpus callosum, which facilitates communication. Each hemisphere is divided into the following lobes which specializes in different functions. Figure 2.1b shows the organization of these lobes within cerebrum.
  - **Frontal Lobe** handles executive functions, voluntary motor control, and emotional regulation.
  - **Parietal Lobe** processes sensory information and spatial awareness.
  - **Motor cortex** helps plan, control, and execute voluntary movement, like moving your arm or kicking a ball.
  - **Somatosensory cortex** receives information about temperature, taste, touch, and movement from the rest of the body.
  - **Temporal Lobe** involved in auditory processing, memory, and language comprehension.
  - **Occipital Lobe** primarily responsible for visual processing.
- Beneath the cerebrum, the **cerebellum** coordinates voluntary movements, balance, and motor learning.
- The **brainstem**, connecting the brain to the spinal cord, controls essential functions like breathing and heart rate.

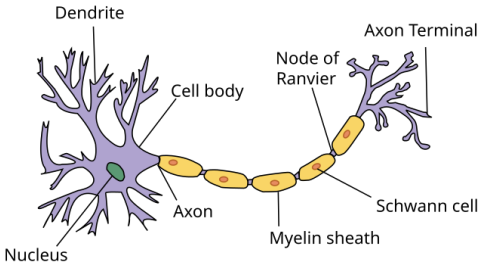

(a)

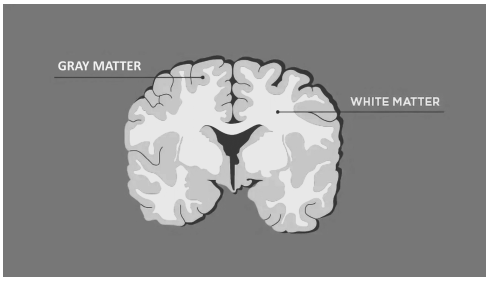

(b)

Figure 2.2: (a) Neuron (Wikipedia, 2017b). *(Credit: Quasar Jarosz at English Wikipedia, CC BY-SA 3.0)* (b) The arrangement of white and gray matter in the brain. *(Credit: Technology Networks).*

2.1.2. WHITE MATTER AND GRAY MATTER

The human brain consists of billions of neurons, which are electrically excitable cells that interconnect in complex networks through electrical and chemical signaling. A typical neuron possesses a cell body and dendrites, which are thin branches extending from the cell body and connecting to hundreds of other neurons, as shown in Figure 2.2a. Besides dendrites, each neuron also has a single axon which is a special extension of the cell body transporting electrical signals across large distances to remote parts of the body. Axons are encapsulated by a myelin sheath whose primary function is to speed up signal transmission. Regions containing neuron cell bodies and dendrites are collectively known as gray matter, while regions composed of myelinated axons are referred to as white matter, shown in Figure 2.2b.

Gray Matter is primarily found in the outer layers of the brain, forming the cerebral cortex, which is a vital layer of tissue coating the surface of the cerebrum and the cerebellum. Gray matter is responsible for processing and integrating information. It plays a critical role in functions such as perception, cognition, and voluntary movement. The density and organization of gray matter can influence cognitive abilities and is often a focal point in studies of neurological disorders.

White Matter are long projections of neurons that transmit signals between different brain regions. The myelin sheath, a fatty substance that insulates these axons, facilitates faster signal transmission, allowing for efficient communication within the brain. White matter forms the inner layer of the brain and is organized into various tracts that connect different areas of gray matter, enabling coordinated activity across the brain.

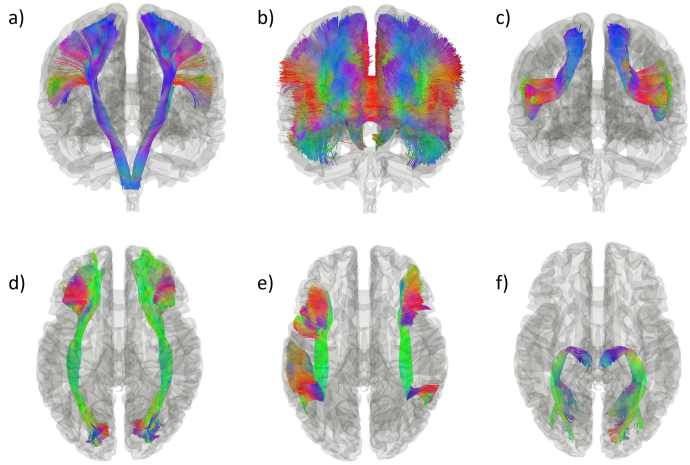

Figure 2.3: Major white matter Tracts a) Corticospinal Tract b) Corpus Callosum c) Frontal Aslant Tract d) Inferior Longitudinal Fasciculus e) Arcuate Fasciculus f) Optic Radiation. *(Credit: The images are adapted from the Human Connectome Project [3], CC BY-SA 4.0).*

The balance and health of both gray and white matter are crucial for normal brain function. Disruption or degeneration of white matter pathways can lead to a range of cognitive and motor impairments, highlighting the importance of white matter integrity in maintaining overall brain health. Diffusion tensor imaging is particularly useful for studying white matter, as it allows for the visualization of the direction and integrity of the brain's white matter.

2.1.3. MAJOR WHITE MATTER TRACTS

White matter bundles interconnect different gray matter regions and are also associated with specific brain functions. For the purpose of this thesis, we limit ourselves to a description of only the major white matter bundles which are described below. As these bundles are also discussed in the following chapters, we consider them to be the most relevant. Figure 2.3 illustrate these bundles. For a complete overview of the other white matter tracts, we refer the reader to the white matter atlas published by Oishi et al. [1].

CORTICOSPINAL TRACT:

This tract runs from the motor cortex in the frontal lobe to the spinal cord and is crucial for voluntary motor control, as shown in Figure 2.3a. It mediates the transmission of signals that execute movement, particularly fine motor skills.

CORPUS CALLOSUM:

The largest white matter structure in the brain, the corpus callosum connects the left and right hemispheres, allowing for interhemispheric communication, as shown in Fig-

ure 2.3b. It plays a critical role in coordinating activities between the two sides of the brain, facilitating functions such as language, sensory perception, and motor control.

FRONTAL ASLANT TRACT:

This bundle connects regions within the frontal lobe, specifically linking the supplementary motor area (SMA) with parts of the inferior frontal gyrus, as shown in Figure 2.3c. It is associated with speech initiation, planning and decision-making.

INFERIOR LONGITUDINAL FASCICULUS:

This tract connects the occipital lobe to the anterior temporal lobe and is involved in visual processing and object recognition, as shown in Figure 2.3d. It plays a key role in integrating visual information with memory and emotional responses, contributing to the recognition of familiar objects and faces.

ARCUATE FASCICULUS:

A significant white matter tract that connects the frontal lobe with the temporal lobe, as shown in Figure 2.3e. The arcuate fasciculus is vital for language processing and production. It enables the integration of auditory information with speech production, making it crucial for fluent communication.

OPTIC RADIATION:

It is a critical white matter pathway in the visual system. It transmits visual information to the primary visual cortex located in the occipital lobe, as shown in Figure 2.3e. This tract plays a pivotal role in processing visual signals received from the retina, enabling the brain to interpret and respond to visual stimuli.

2.2. WHITE MATTER VISUALIZATION IN NEUROSURGERY

White matter visualization is widely used in neurology and neurosurgery. In this thesis, the focus is on its application in the neurosurgical workflow using DTI. In neurosurgery, visualizing white matter is crucial for preoperative planning, intraoperative navigation, and postoperative prognosis. This is especially true for complex procedures like tumor resection, which is the primary focus of this thesis.

Tumor resection surgery is a critical procedure aimed at removing brain tumors, which are abnormal growths that can disrupt normal brain function. Among these, gliomas are the most common type of primary brain tumor. Gliomas originate from the brain's supportive cells and are known for their ability to grow and spread surrounding brain structures, and care must be taken not to damage nearby critical functional structures in order to avoid severe and permanent neurological deficits.

The primary goal of tumor resection surgery is to remove as much of the tumor as possible while preserving essential brain functions. This is especially important for gliomas, which often grow near regions of the brain responsible for movement, speech, or vision.

Prior to the surgery, white matter maps can be created using DTI, allowing neurosurgeons to identify and preserve essential pathways during procedures. For example, knowledge of the location of the corticospinal tract is vital when removing brain tumors

in the vicinity to minimize the risk of postoperative motor deficits. White matter visualization also aids in delineating the relationship between tumors and adjacent white matter tracts, helping formulate surgical strategies that maximize tumor removal while minimizing damage to critical areas. However, the presence of tumor, affect the behavior of water diffusion in the brain, which is the fundamental property measured by DTI. Additionally, tumors can directly impact the underlying fiber structures. For instance, a tumor may displace, infiltrate, or disrupt fiber bundles. Some types of tumors are also surrounded by fluid, known as edema, which can interfere with fiber tracking algorithms, even when the fiber structure itself remains intact. In Chapter 4 we will discuss probabilistic fiber tracking algorithms which attempt to deal with such problems.

Intraoperatively, white matter visualization, created by DTI, are frequently integrated with neuronavigation systems to provide real-time guidance. This is particularly important for surgeries involving eloquent brain regions, where even minor damage to critical tracts can lead to significant neurological deficits. One of the applications of DTI is in awake brain surgery, a technique often employed for removing tumors located in areas responsible for speech or motor control. During these procedures, DTI-derived maps are used alongside cortical and subcortical stimulation to identify and preserve functional pathways while monitoring the patient's neurological responses in real time. This approach try to potentially minimize functional impairments during tumor resection procedure. In Chapter 7, we examined the potential influence of decision-making process for employing awake brain surgery in patients with gliomas.

2.3. CONCLUSION

In this chapter, we explained the medical background which is needed for understanding the clinical context of the research to be discussed in later chapters. Understanding these concepts sets the stage for Chapter 3, where we will explore the technical principles of DTI.

REFERENCES

[1] Kenichi Oishi et al. *MRI atlas of human white matter*. Academic Press, 2010.

[2] Beth E. Trapp. "National Institute of Neurological Disorders and Stroke". In: *Journal of Consumer Health on the Internet* 14.2 (2010), pp. 167–174. DOI: 10.1080/15398281003784638. URL: http://www.ninds.nih.gov.

[3] Fang-Cheng Yeh et al. "Population-averaged atlas of the macroscale human structural connectome and its network topology". In: *Neuroimage* 178 (2018), pp. 57–68.

3

Technical Background

In the previous chapter, we focus on the medical background, discussing the basic concepts of brain anatomy and and the significance of the knowledge of white matter in clinical applications. Chapter 3 transitions to the technical foundation of DTI. This chapter will delve into the pipeline that transforms raw imaging data into the representations of white matter architecture. In this chapter, we will discuss each aspect of the DTI pipeline in detail, presenting the key principles and associated techniques.

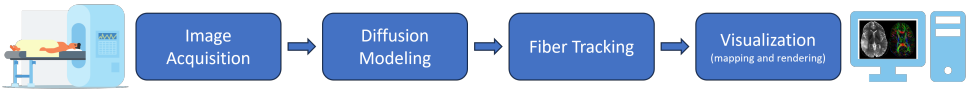

Figure 3.1: The DTI pipeline including acquisition of DW-MR image, diffusion tensor modeling, fiber tracking and visualization.

3

3.1. DTI PIPELINE

The DTI pipeline consists of several interconnected stages that transform MRI acquired diffusion-weighted images into representations of white matter architecture. This pipeline, as shown in Figure 3.1, encompasses image acquisition, diffusion modeling, fiber tracking, and visualization, each playing a critical role in transforming the MRI data into valuable insights about white matter structure.

The first step in the pipeline is the acquisition of diffusion-weighted magnetic resonance (DW-MR) images. This stage involves applying specific imaging protocols to capture the diffusion patterns of water molecules within the brain, which reflect the orientation and integrity of white matter fibers. Following acquisition, the diffusion modeling phase applies models to characterize the diffusion properties of tissue. In DTI, this stage estimates the diffusion tensor that describes the water diffusion at each voxel in the brain. For other acquisition modalities, different modeling techniques are used, such as, Spherical Deconvolution or Q-ball imaging.

Once the diffusion tensor is determined, fiber tracking is performed to reconstruct the trajectories of white matter tracts, offering visual representation of its structural organization. Finally, the visualization phase employs various techniques to present the reconstructed fiber tracts, facilitating interpretation and analysis. Next, we will describe each steps of the pipeline in more detail.

3.2. IMAGE ACQUISITION

DW-MRI aims to measure the directional Brownian movement of water molecules in tissue. Here we discuss the fundamental concepts of diffusion and MRI that underlie DWI acquisition.

3.2.1. WATER DIFFUSION

Diffusion is the process by which molecules move randomly due to thermal energy, a phenomenon known as Brownian motion. This molecular movement, which leads to a gradual spread from areas of high to low concentration, is particularly informative in biological tissues, where the local structure influences diffusion patterns. Water molecules move differently depending on whether they encounter barriers like cell membranes or myelin in white matter. In unrestricted fluid, the water molecules moves freely, having isotropic diffusion with a constant diffusion coefficient D, as shown in Figure 3.2a. In tissues, however, water diffusion is directionally constrained, or anisotropic, as their movement is restricted by physical barriers such as cell membranes or cytoskeletal structures (Figure 3.2b). In this case, the diffusion coefficient is reduced because of the re-

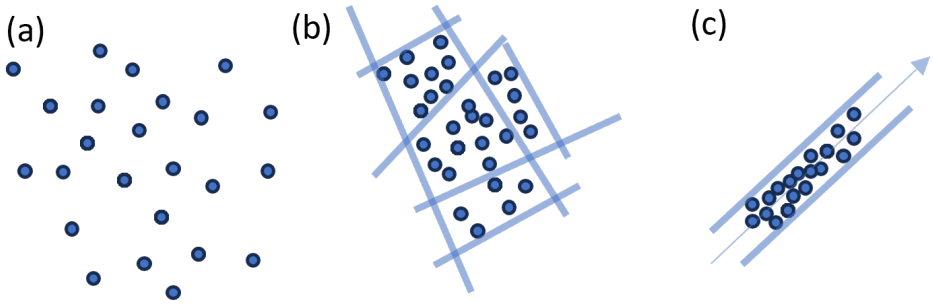

Figure 3.2: Isotropic diffusion without physical barriers. (b) Restricted isotropic diffusion without preferred orientation. (c) Restricted anisotropic diffusion with preferred orientation.

stricted movement. In fibrous tissues, water diffusion shows orientational dependency. Molecules tend to move along the length of axonal fibers rather than across them, as shown in Figure 3.2c. This anisotropic diffusion allows infering the orientation and integrity of these fibers locally. In the next section we describe how the Brownian motion can be measured with MRI.

3.2.2. PRINCIPLES OF MRI

Magnetic Resonance Imaging (MRI) is a non-invasive imaging technique that utilizes strong magnetic fields and radio frequency pulses to generate detailed images of the body's internal structures. The underlying principle of MRI is based on the behavior of hydrogen nuclei (protons), which are abundant in biological tissues, particularly water and fat.

When placed in a magnetic field, protons align with the direction of the field. A radiofrequency pulse is then applied, causing the protons to absorb energy and temporarily shift their alignment. Once the pulse is turned off, the protons gradually return to their original alignment, releasing energy in the process. This released energy is detected and converted into an image. The time it takes for protons to return to equilibrium, known as relaxation time, varies depending on the tissue type and its micro environment.

3.2.3. DIFFUSION WEIGHTED MRI AND SENSITIZING GRADIENTS

Building on the principles of MRI, diffusion MRI extends conventional imaging to capture the random motion of water molecules within tissue. While MRI measures anatomical structures and tissue properties, diffusion MRI specifically focuses on the random displacement of water molecules, as explained in Section 3.2.1.

Bihan et al. [13] introduced diffusion MRI for clinical applications. The degree to which water molecules diffuse is captured through the application of diffusion-sensitizing gradients. The relationship between diffusion and the measured MR signal is described by the equation below derived by Stejskal and Tanner [21], they observed the anisotropic diffusion of water molecules in tissues and investigated the related modeling of the diffusion effects using MRI.

$$S(g_i) = S_0 \cdot e^{-bD_i} \tag{3.1}$$

In this equation, $S(\mathbf{g}_i)$ represents the signal acquired in the presence of a gradient applied in direction $\mathbf{g_i}$, S_0 is the baseline signal without diffusion-sensitized gradient, b is the diffusion sensitivity factor, and D_i is the so-called apparent diffusion coefficient for the specific gradient direction g_i. The term b is influenced by the gradient strength, duration, and the time interval between the gradient pulses, which allows for the quantification of diffusion coefficient in the specified direction, within a given time interval. The amount of gradient directions and computed b-values define the acquisition type. In DTI, images are typically acquired with 6 to 30 gradient directions and a b-value of approximately 1000 s/mm². In contrast, HARDI acquisition requires a substantially larger number of diffusion directions, typically at least 60–90 and for DSI, images are acquired with 15-500 gradient directions. Higher gradient direction acquisition can capture more complex information of the diffusion, however, it leads to longer scan times, higher computational complexity, and greater susceptibility to noise. DTI remains widely preferred in clinical setting due to its simplicity, computational efficiency, and lower acquisition requirement.

3.3. DIFFUSION MODELING

The spatial distribution of water molecule movement within a voxel is termed as **diffusion profile** which describes how water diffuses in different directions, which is influenced by the microstructural properties of the surrounding tissue. There are many methods for the modeling of the diffusion profile, e.g. Diffusion Tensor Imaging (DTI), Q-ball Imaging (QBI), Constrained Spherical Deconvolution (CSD) etc. In this thesis, we are focusing on DTI.

In DTI, water diffusion in tissue is modeled using a second-order symmetric positive semidefinite tensor, a 3x3 matrix that characterizes diffusion process in three-dimensional (3D) space. This modeling represents the diffusion as a 3D Gaussian distribution, capturing various profiles such as isotropic (spherical), planar, and anisotropic (ellipsoidal).

The diffusion tensor D, introduced by Basser et al. [1], is a symmetric positive semidefinite tensor represented by a 3 × 3 matrix, with scalar elements denoted by D_{ij} as follows:

$$D = \begin{bmatrix} D_{xx} & D_{xy} & D_{xz} \\ D_{yx} & D_{yy} & D_{yz} \\ D_{zx} & D_{zy} & D_{zz} \end{bmatrix} \tag{3.2}$$

In this matrix, the diagonal elements D_{xx}, D_{yy}, and D_{zz} represent the diffusion coefficients along the principal axes, while the off-diagonal elements (D_{xy}, D_{xz}, D_{yx}, etc.) capture the correlation of diffusion between different axes.

For any specific gradient direction, g_i, the apparent diffusion coefficient can be calculated as:

$$D_i = \boldsymbol{g_i}^T D \boldsymbol{g_i} \tag{3.3}$$

To estimate the elements of the diffusion tensor matrix D from the measured diffusion-weighted magnetic resonance imaging data, the Stejskal and Tanner equation can be used as given in Equation 3.1. Since the diffusion tensor is symmetric we need at least 6 diffusion measurements $S(g_i)$ in each voxel to reconstruct it. To estimate the diffusion tensor D, we can combine Equation 3.1 and Equation 3.3 and solve system of equations for N instances. Each equation is given by:

$$\log\left(\frac{S(\boldsymbol{g_i})}{S_0}\right) = -b\,\boldsymbol{g_i}^T D \boldsymbol{g_i} \tag{3.4}$$

This system of equations can be simplified as follows.

$$\boldsymbol{s} = B \cdot d \tag{3.5}$$

where **s** is a vector containing the signal values for each gradient direction, $\boldsymbol{s} = \log\left(\frac{S(\boldsymbol{g_i})}{S_0}\right)$, B is the B-matrix containing direction-dependent b-value and gradient information, and d is a vector containing the 6 unique values of the diffusion tensor. If N = 6, Equation 3.5 has the exact solution $d = B^{-1}s$. To reduce noise effects, however, in DTI, the applied gradients are commonly more than 6 directions. In this case, solving the matrix equation becomes a least-squares problem.

3.4. TENSOR SHAPE AND DIFFUSION METRICS

The diffusion matrix D can be represented as a diffusion ellipsoid, where the shape of the ellipsoid depends on the three eigenvectors (e_1, e_2, e_3) and the corresponding eigenvalues (λ_1, λ_2, λ_3) determined by the eigen analysis of matrix D. The orientation of the ellipsoids represents the direction of the major eigenvector, while the length represents the corresponding eigenvalue, as shown in Figure 3.3a. The 3D shape of water diffusion in living tissues reveals valuable information about the underlying tissue structure. As discussed in Section 3.2.1, areas where the tissue structure does not have barriers, has isotropic diffusion. In this case, the diffusion tensor takes spherical shape within a voxel. Conversely, in areas where tissue has a single dominant orientation, such as brain white matter tracts, the diffusion tensor becomes elongated and ellipsoidal. However, the brain's white matter also contains complex fiber arrangements, including crossing, kissing, bending, and diverging fibers. In this case, there is more than one dominant diffusion direction. The second-order diffusion tensor cannot resolve these complex structures instead represents them with a disk-like or planar shape. For the purpose of analysis of diffusion tensor, several geometric measures exist to quantify tensor shape, as presented by Westin [24]. These metrics provide insights into the structure and organization of the brain tissue, and they can be particularly useful for clinical and research purposes. Following are some commonly used diffusion metrics:

MEAN DIFFUSIVITY (MD):

Mean diffusivity is calculated as the average of the eigenvalues of the diffusion tensor and provides an overall measure of the diffusion capacity within a voxel. It is given by:

$$MD = \frac{\lambda_1 + \lambda_2 + \lambda_3}{3}$$

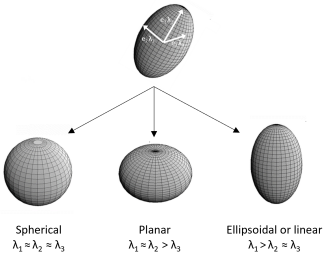

(a) Diffusion tensor shapes with three eigenvectors (e_1, e_2, e_3) and the corresponding eigenvalues (λ_1, λ_2, λ_3).

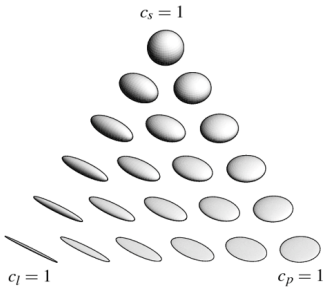

(b) Ellipsoid glyphs (Westin [24]).

Figure 3.3: Shapes of the 2nd-order Diffusion tensor.

where $\lambda_1, \lambda_2, \lambda_3$ are the eigenvalues of the diffusion tensor. Increased MD values may indicate tissue edema or damage, while decreased MD may suggest restricted diffusion associated with healthy, densely packed tissues, as shown in Figure 3.2.

FRACTIONAL ANISOTROPY (FA):

Fractional anisotropy quantifies the degree of anisotropy in diffusion, reflecting the directional dependence of water diffusion. It is the most widely used scalar measure in diffusion tensor imaging [2] and represents the extent of the diffusion anisotropy. A low FA value indicates that the diffusion is free (FA=0; isotropic) while a high value of FA implies that the diffusion is restricted to a single direction (FA=1; anisotropic). FA is calculated using the formula:

$$FA = \frac{\sqrt{3}}{2} \frac{\sqrt{(\lambda_1 - MD)^2 + (\lambda_2 - MD)^2 + (\lambda_3 - MD)^2}}{\sqrt{\lambda_1^2 + \lambda_2^2 + \lambda_3^2}}$$

FA is commonly used to assess white matter integrity, where higher values typically indicate healthier, more organized fiber tracts. However, FA cannot distinguish between linear and planar shapes of diffusion because it only measures the overall deviation from isotropic and not the specific geometry of the diffusion tensor.

C_L, C_P, C_S:

Westin et al. [24] proposed additional anisotropy measures to distinguish between linear, planar and spherical diffusion:

$$C_L = \frac{\lambda_1 - \lambda_2}{\lambda_1 + \lambda_2 + \lambda_3}$$

$$C_P = \frac{2(\lambda_2 - \lambda_3)}{\lambda_1 + \lambda_2 + \lambda_3}$$

$$C_S = \frac{3\lambda_3}{\lambda_1 + \lambda_2 + \lambda_3}$$

Each of these measures has a range between [0; 1] and $C_L + C_P + C_S = 1$. Figure 3.3b represents the barycentric space of diffusion tensor shapes in which the three extremes (linear, planar, and spherical) are at the corner of triangles.

Many other scalar measures have been proposed based on more complex behaviour of molecular diffusion and are explained in detail in surveys by Novikov et al. [18], Rajagopalan et al. [20] and Vilanova et al. [22].

3.5. FIBER TRACKING

The most exciting stage in the DTI pipeline is the reconstruction of the 3D pathways by utilizing the per-voxel information about the orientation of the underlying neural tracts. The process of virtual reconstruction of the neural fiber tract on the basis of the diffusion tensor is named Fiber Tracking or Tractography. It involves tracing 3D paths through diffusion tensor field. The main eigen vector (e_1) of the diffusion tensor D, represents the principle fiber direction at each voxel. One of the most straight forward and widely used technique is steamline tracing, which is a common concept and well known in fluid dynamics [9] and flow visualizations [6]. In second-order diffusion tensor fields, streamline follow the principal eigenvectors of the voxel [3]. Vector field integration is performed using various schemes to define the streamlines in the eigenvector field. The implementation of the fiber tracking algorithm typically involves these four major steps:

REGION DEFINITION AND FILTERING:

Regions are usually defined by the user to start, end or control the fiber pathways. The seeding region refers to the starting point of the tracking process and defines the initial conditions for numerical integration. Regions are also used to extract a specific bundle of interest and filter out others to avoid visual clutter.

NUMERICAL APPROXIMATION:

Different types of numerical approximation schemes can be implemented in the fiber tracking algorithm. Euler integration is the most straight forward technique [16]. Higher-order methods, such as 2^{nd} or 4^{th} order Runge-Kutta methods [3], are typically less sensitive to noise and can be used for more accurate results.

INTERPOLATION:

During the numerical approximation process, the sample position after each integration step often lies between volume grid points, hence, interpolation is needed to estimate values, based on the neighboring grid points. Commonly, linear interpolation is used but other methods exists with different pros and cons, as explained by Kindlmann [12]

STOPPING CRITERIA:

These prevent the algorithm from tracing into regions where the main eigen vector is not reliably defined. In DTI, this can occur in areas of planar or isotropic diffusion, such as brain gray matter. Different scalar measures, such as FA, MD, Cl or curve angle can be used as stopping criteria in the fiber tracking process.

3.5.1. FIBER TRACKING TECHNIQUES

In principle, fiber tracking techniques can be divided into the following two main categories:

DETERMINISTIC FIBER TRACKING

Deterministic algorithms, given the same input, always produce the same output. There are many deterministic fiber tracking algorithms that can be selected for DTI fiber tracking when the discrete fiber directional information is given. For example, the fiber assignment by continuous tracking (FACT) algorithm, is widely adopted and has been implemented in several fiber tracking software packages [17]. It uses the conventional voxel concept and its core propagation algorithm is close to Euler's streamline integration method for extremely fast tracking speed.

PROBABILISTIC FIBER TRACKING

Probabilistic fiber tracking approach generates multiple possible fiber paths from each seed point, based on a statistical distribution of diffusion orientations instead of selecting the most probable orientation from the measurements. By sampling the diffusion direction from a probability distribution derived from the diffusion tensor, probabilistic tracking can provide a representation of fiber pathways, especially in areas with crossing fibers. This method is beneficial for visualizing complex anatomical structures, though it can be computationally intensive and require additional parameters for accurate interpretation. We defer an extensive discussion of probabilistic methods to Chapter 4. Various techniques has been presented in the literature, and is summarized in the review article by [10].

3.6. VISUALIZATION

Visualization of diffusion tensor imaging data is essential for translating diffusion information into interpretable images, aiding both research and clinical applications. Following we discuss several techniques employed to visualize DTI data, each offering insights into different aspects of diffusion.

3.6.1. VOLUME RENDERING

Volume rendering is a technique commonly used to visualize three-dimensional scalar fields. In the context of DTI, volume rendering allows for the representation of the entire voxel space, providing an overview of the underlying anatomical structures and diffusion properties. This can be done by converting tensor to one scalar quantity e.g, FA at each voxel. This technique utilizes transfer function to convey different attributes of the data. A transfer function maps data values to visual properties such as color and opacity, enabling the differentiation of structures and features within the volume.

By manipulating the transfer functions, clinicians and researchers can emphasize particular regions or features of interest. Transfer functions for diffusion tensor was first defined by Westin [23] and used for the direct volume rendering of diffusion data. For further elaboration, lighting effects were added by Kindlmann et al. [12], that account for tensor anisotropy and diffusion orientation, as shown in Figure 3.4. Hlawitschka et al. [8] presented a novel method that allows the interactive exploration of the volumetric

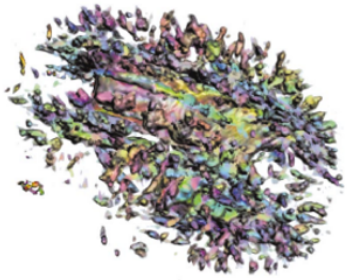

(a) Lit-Tensors Kindlmann et al. [12].

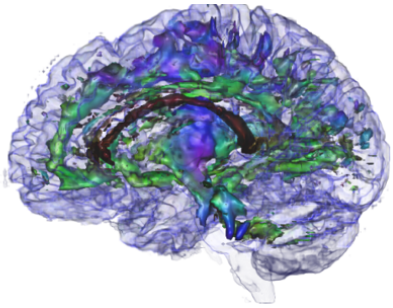

(b) Interactive Volume rendering Hlawitschka et al. [8].

Figure 3.4: Volume rendering techniques used for visualizing DTI data.

DTI data sets. Despite its usefulness, volume rendering technique also has certain limitations. One major downside is the loss of information, as volume rendering visualizes scalar fields rather than the full tensor data. Additionally, the technique suffers from occlusion and overlap, as it displays the entire dataset simultaneously, making it difficult to distinguish individual fiber tracts or regions of interest. As a result, alternative methods such as glyph-based or line-integration-based visualizations are generally preferred for their ability to represent the directional and structural details of white matter.

3.6.2. GLYPH-BASED VISUALIZATIONS

Glyph-based visualizations offer an alternative approach to represent diffusion data by utilizing geometric shapes, or glyphs, to encode the local information of the diffusion tensor. Data information is mapped to glyph characteristics such as shape and color. Glyphs provide a way to represent the full six-dimensional information of a diffusion tensor by mapping the eigenvectors and eigenvalues to the orientation and shape of a geometric primitive. The most straight forward approach to visualize the diffusion tensor are ellipsoidal glyphs, used by Pierpaoli and Basser [19] as shown in Figure 3.3b. Among several other proposed techniques, the super quadratic glyph is considered state-of-the-art for glyph-based tensor visualization. Instead of interpolating between ellipsoidal shapes, Kindlmann [11] represents the diffusion by superquadrics with shape parameters defined by the barycentric coordinates. Ellipsoids differing in shape can be confusing, from certain viewpoints, because of similarities in profile and shading. Superquadric glyphs, on the other hand, addresses the problems of asymmetry and ambiguity with a new tunable continuum of glyphs based on superquadric surfaces. The glyph based visualization provide the detailed directional information of the tensor locally. However, for the global connectivity information, as needed for fiber tract visualization, line-integration based approaches are used, as discussed in the next section.

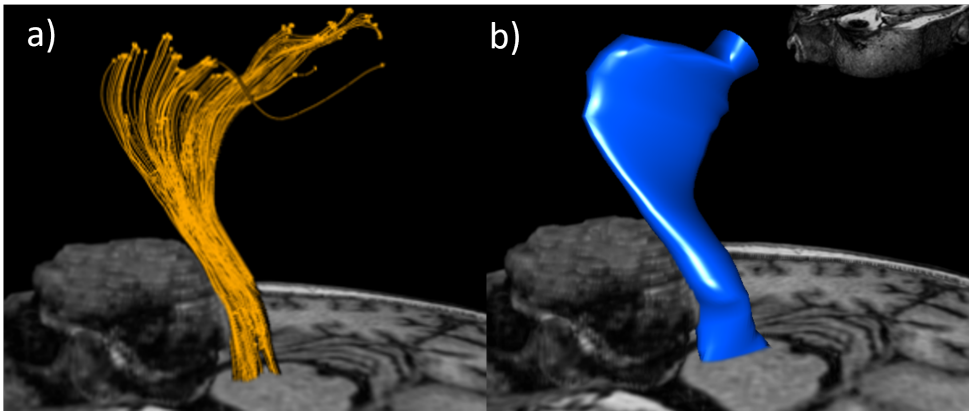

Figure 3.5: a) Traditional polyline visualization. (b) Hull-based visualization [7].

3.6.3. LINE-INTEGRATION-BASED VISUALIZATIONS

Line-based visualization is a widely adopted technique for representing the results of fiber tracking algorithms in diffusion imaging (See Section 3.5). This approach visualizes white matter tracts as a collection of polylines directly, where each poly line corresponds to the computed fiber tract. Numerous strategies have been introduced, such as thin polylines [15], illuminated streamlines [26] or cylindrical tubes [4]. Zhang et al. [25] introduced streamtubes to encode the local diffusion tensor information along the cross-section of the fiber tracts at each voxel. The spaghetti plot visualization has several shortcomings. Most importantly, it suffers from clutter and occlusion, making it difficult to distinguish between areas with a single fiber sample compared to number of densely distributed ones. To reduce clutter, Enders et al. [7] presented a technique to wrap the fiber bundles within a surface hull, as shown in Figure 3.5. Similar techniques have been used by Merhof et al. [14] and Chen et al. [5]. We further discuss the more complex line-integration-based visualization in Section 4.3.2.

CONCLUSION

This chapter provided a basic technical overview of diffusion tensor imaging (DTI), from acquisition principles to diffusion modeling and visualization. We introduced key elements of the DTI pipeline, explaining MRI-based diffusion measurement, the diffusion tensor model, and its fitting process. Diffusion metrics derived from these models for characterizing white matter structure. We also discussed fiber tracking methods and visualization techniques, including volume rendering, glyphs, and line based visualization.

The DTI pipeline involves several complex stages, therefore, it is prone to uncertainty from various sources, impacting the reliability of data interpretation. In the next chapter, we will examine the uncertainties involved in DTI, focusing on uncertainty visualization that aid clinicians and researchers in making more informed assessments.

REFERENCES

[1] Peter J Basser, James Mattiello, and Denis LeBihan. “Estimation of the effective self-diffusion tensor from the NMR spin echo”. In: *Journal of Magnetic Resonance, Series B* 103.3 (1994), pp. 247–254.

[2] Peter J Basser and Carlo Pierpaoli. “Microstructural and physiological features of tissues elucidated by quantitative-diffusion-tensor MRI”. In: *Journal of magnetic resonance* 213.2 (2011), pp. 560–570.

[3] Peter J Basser et al. “In vivo fiber tractography using DT-MRI data”. In: *Magnetic resonance in medicine* 44.4 (2000), pp. 625–632.

[4] Philipp G Batchelor et al. “Study of connectivity in the brain using the full diffusion tensor from MRI”. In: *Biennial International Conference on Information Processing in Medical Imaging*. Springer. 2001, pp. 121–133.

[5] Weri Chen et al. “Abstractive representation and exploration of hierarchically clustered diffusion tensor fiber tracts”. In: *Computer Graphics Forum*. Vol. 27. 3. Wiley Online Library. 2008, pp. 1071–1078.

[6] Akhil Datta-Gupta. “Streamline Simulation: A Technology Update (includes associated papers 71204 and 71764)”. In: *Journal of petroleum technology* 52.12 (2000), pp. 68–84.

[7] Frank Enders et al. *Visualization of white matter tracts with wrapped streamlines*. IEEE, 2005.

[8] Mario Hlawitschka et al. *Interactive volume rendering of diffusion tensor data*. Springer, 2009.

[9] Thomas JR Hughes and Michel Mallet. “A new finite element formulation for computational fluid dynamics: III. The generalized streamline operator for multidimensional advective-diffusive systems”. In: *Computer methods in applied mechanics and engineering* 58.3 (1986), pp. 305–328.

[10] Ben Jeurissen et al. “Diffusion MRI fiber tractography of the brain”. In: *NMR in Biomedicine* 32.4 (2019), e3785.

[11] Gordon Kindlmann. “Superquadric tensor glyphs”. In: *Proceedings of the Sixth Joint Eurographics-IEEE TCVG conference on Visualization*. Eurographics Association. 2004, pp. 147–154.

[12] Gordon Kindlmann, David Weinstein, and David Hart. “Strategies for direct volume rendering of diffusion tensor fields”. In: *IEEE transactions on Visualization and Computer Graphics* 6.2 (2000), pp. 124–138.

[13] Denis Le Bihan et al. “MR imaging of intravoxel incoherent motions: application to diffusion and perfusion in neurologic disorders.” In: *Radiology* 161.2 (1986), pp. 401–407.

[14] Dorit Merhof et al. “Isosurface-based generation of hulls encompassing neuronal pathways”. In: *Stereotactic and functional neurosurgery* 87.1 (2009), pp. 50–60.

[15] Susumu Mori, Barbara J Crain, and Peter CM Van Zijl. “3D brain fiber reconstruction from diffusion MRI”. In: *NeuroImage* 7.4 PART II (1998), S710. DOI: 10.1016/S1053-8119(18)31543-X.

[16] Susumu Mori and Peter CM Van Zijl. “Fiber tracking: principles and strategies–a technical review”. In: *NMR in Biomedicine: An International Journal Devoted to the Development and Application of Magnetic Resonance In Vivo* 15.7-8 (2002), pp. 468–480.

[17] Susumu Mori et al. “Three-dimensional tracking of axonal projections in the brain by magnetic resonance imaging”. In: *Annals of Neurology: Official Journal of the American Neurological Association and the Child Neurology Society* 45.2 (1999), pp. 265–269.

[18] Dmitry S Novikov et al. “Quantifying brain microstructure with diffusion MRI: Theory and parameter estimation”. In: *NMR in Biomedicine* 32.4 (2019), e3998.

[19] Carlo Pierpaoli and Peter J Basser. “Toward a quantitative assessment of diffusion anisotropy”. In: *Magnetic resonance in Medicine* 36.6 (1996), pp. 893–906.

[20] V Rajagopalan et al. “EA Basic Introduction to Diffusion Tensor Imaging Mathematics and Image Processing Steps”. In: *Brain Disord Ther* 6.229 (2017), p. 2.

[21] Edward O Stejskal and John E Tanner. “Spin diffusion measurements: spin echoes in the presence of a time-dependent field gradient”. In: *The journal of chemical physics* 42.1 (1965), pp. 288–292.

[22] Anna Vilanova et al. “An introduction to visualization of diffusion tensor imaging and its applications”. In: *Visualization and Processing of Tensor Fields*. Springer, 2006, pp. 121–153.

[23] C -F Westin et al. “Image processing for diffusion tensor magnetic resonance imaging”. In: *Medical Image Computing and Computer-Assisted Intervention–MICCAI’99: Second International Conference, Cambridge, UK, September 19-22, 1999. Proceedings 2*. Springer. 1999, pp. 441–452.

[24] C-F Westin. “Geometrical diffusion measures for MRI from tensor basis analysis”. In: *Proc. ISMRM’97* (1997).

[25] Song Zhang, Cagatay Demiralp, and David H Laidlaw. “Visualizing diffusion tensor MR images using streamtubes and streamsurfaces”. In: *IEEE Transactions on Visualization and Computer Graphics* 9.4 (2003), pp. 454–462.

[26] Malte Zockler, Detlev Stalling, and H-C Hege. “Interactive visualization of 3D-vector fields using illuminated stream lines”. In: *Proceedings of Seventh Annual IEEE Visualization’96*. IEEE. 1996, pp. 107–113.

4

UNCERTAINTY VISUALIZATION IN DTI

In the previous chapter, we presented the DTI pipeline, detailing its four main stages. Each stage, however, relies on assumptions, parameters, and estimations that introduce significant uncertainties. These uncertainties can propagate through the pipeline, leading to variability in the final output. In this chapter, we focus on examining the uncertainties inherent in the DTI pipeline, particularly in the context of its clinical applications. We briefly cover the approaches used for quantification of uncertainties and review state-of-the-art strategies for uncertainty visualization in DTI. We compare their main characteristics and drawbacks. We explore various methodologies for uncertainty visualization in other domains that have not yet been applied to DTI or, more broadly, to DWI, and discuss how these techniques can be adapted for use in this field. This chapter is based on the paper:

Siddiqui, F., Höllt, T., and Vilanova, A. (2021). Uncertainty in the DTI Visualization Pipeline. In Anisotropy Across Fields and Scales (pp. 125-148). Springer International Publishing.
https://doi.org/10.1007/978-3-030-56215-1_6.

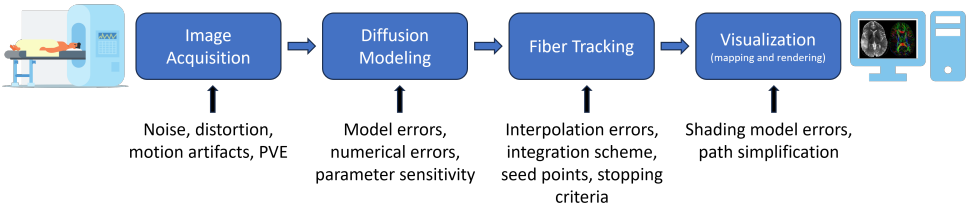

Figure 4.1: The DTI processing pipeline with sources of uncertainties at each step.

The DTI processing pipeline, as discussed in the previous chapter, involves complex stages of mathematical modeling, analysis, mapping, and rendering strategies, therefore, it is prone to uncertainty from various sources. Noise, patient movement, modeling residuals, and distortion from imaging artifacts produce uncertainty in the orientation of the diffusion tensor and are detrimental to fiber tracking algorithms. These uncertainties hamper the link between the data being measured and visualized.

4.1. SOURCES OF UNCERTAINTY

In this section we extend the Figure 3.1 by adding sources of uncertainty involved at each stage of the DTI pipeline, as shown in Figure 4.1. Following, we will go through this pipeline and discuss the sources of error present at each stage. While our focus is on the DTI modality, many sources of uncertainty also arise in DWI pipelines that extend beyond DTI.

4.1.1. IMAGE ACQUISITION

MRI-based techniques usually suffer from various acquisition errors such as noise, motion artifacts, partial volume effects, etc. Signal to noise ratio in DWI sequences is relatively high given that signal attenuation is being measured. The effect of noise on the DTI output has been widely studied in literature [2, 36, 47]. There has been a growing trend of increasing the gradient direction in DTI acquisition to improve the tractography quality. However, this further increases the acquisition time. In HARDI, the gradient directions for acquisition are much higher than that of DTI and, therefore, it needs more time. With higher acquisition time, it is more likely that the subject move during the scan, which in turn, introduces misalignment in the acquired image. These kinds of artifacts are known as motion artifacts. Providentially, these misalignments can be corrected during the registration process. Several automated techniques have been introduced to remove this artifact [77]. The finite resolution of the results also affects the output of the process. The resolution of a clinical DWI acquisition is typically in the order of millimeter (mm) in each direction, which is much lower than that of actual axons. Therefore, the signal values have to be averaged to be able to fit in a single image voxel. This loss of information is called the partial-volume effect (PVE). Several studies have been conducted in neurological literature to investigate the PVE in DTI [58, 59, 68]. Other sources of error during image acquisition involve Magnetic Distortion, Scanner setting and others [11].

4.1.2. DIFFUSION MODELING

In DTI, the diffusion of a water molecule is mathematically represented by a second-order tensor, known as the diffusion tensor. Numerous measurements are performed along various gradient directions to determine the molecular diffusion at each voxel. The least-squares method is the most commonly used fitting technique to calculate the diffusion tensor, but other more accurate regression procedures can also be used [3, 4]. This fitting procedure introduces both a fitting error and a model selection step, contributing to variability in the outcomes of the DTI process. DTI technique can only estimate one dominant diffusion direction per voxel, and thus, is incapable of determining the structure where the multi-fiber direction is present and, therefore, results in unreliable outcomes. HARDI models emerge to overcome this limitation and able to model complex fibrous regions of the brain. It provides a way to estimate the multi-fiber populations that can then be used for robust tractography. HARDI models are more complex and usually introduce more parameters and choices to be determined than DTI.

4.1.3. FIBER TRACKING

Fiber tracking involves the reconstruction of the fibrous structure of the brain white matter by gradually following the local fiber orientation estimated from the diffusion tensor, as explained in Section 3.5.1. As discussed, there are several parameters in fiber tracking algorithm to control the tracking process, however, these parameters add variability to the fiber tracking results. There are four major sources of uncertainties in the fiber tracking algorithm:

1. Region definition and filtering
2. Numerical approximation
3. Interpolation
4. Stopping criteria

Region definition and filtering: The region definition in the fiber tracking process can add variation in the outcome. Usually, these regions are defined manually, and therefore introduce an implicit user bias. A minor variation in the definition, can result in largely different pathways. Recently, several techniques have been proposed to minimize the effect of seed region in the fiber tracking algorithms [17, 36, 69].

Numerical approximation: The integration method, or the chosen step size, can further affect the quality of these integration schemes [66], discussed in Section 3.5.1. Different schemes can lead to the different outcome, hence, adds variability in the results.

Interpolation: Several studies have been conducted to address the effect of interpolation in fiber tracking [24, 74]. Various kinds of interpolation schemes are present, each result in different pathways, and therefore, add variability in the results.

Stopping criteria: Fiber tracking algorithms are often highly sensitive to these values, meaning that a very small variation in the stopping criteria can lead to a very large change in the resulting fiber [66]. Brecheisen et al. [13] propose a visual exploration tool that allows users to investigate the behavior and sensitivity of DTI fiber tracking to stopping criteria.

In fiber tracking algorithms for HARDI models the principal directions are extracted from a multifiber representation which adds another layer of complexity to the algorithms.

4.1.4. VISUALIZATION

The visualization stage involves the mapping of the data into a geometric representation or visual primitives that are finally rendered on to the screen. This process can be another source of the uncertainty. Various photo-realistic rendering techniques are used to simulate real world lighting as exact as possible, but this further complexity adds uncertainty in the outcome. Lighting models and shadows enhance the structural perception of the fibers and as such improve the recognition of the spatial relations between tracts; however, the controlling parameters can add further variability in the final results.

4.2. UNCERTAINTY MODELING

As discussed in the previous section, many sources of uncertainties are present at each stage of the DTI visualization pipeline that affect the outcome of the process. These uncertainties propagate through the pipeline adding uncertainty in the derived quantities including diffusion tensor and fiber orientations. Estimating the error distribution of different sources is not a straight forward task. Different approaches have been used to model the uncertainty, however, each with pros and cons. We have classified the methods used for the uncertainty quantification into two categories:

1. Analytical methods
2. Stochastic methods

4.2.1. ANALYTICAL METHODS

Analytical methods refer to approaches that provide an explicit mathematical formulation of the error distribution. These modeling techniques are based on the Bayes theorem [45] and were first introduced by Behrens et al. [8] in DWI. They estimated the probability distribution function (PDF) of the fiber orientation by a Bayesian model. The main disadvantage of this modeling technique is that they rely on the assumption of prior and noise present in the data. These techniques are computationally inexpensive, however, their dependence on the prior assumption limit their widespread use. Most of the Bayesian model-based techniques are often combined with random sampling methods, such as Markov Chain Monte Carlo (MCMC), to determine the distribution of model parameters [8, 9, 25]. The application of Bayesian model based methods in DTI and HARDI has been reported several times [37, 43, 49].

Shortest path algorithms are another useful approach for quantifying structural brain connectivity and were first introduced by O'Donnell et al. [55]. This approach

relies on computing the connections between regions of interest rather than connections from a seed. Schober et al. [62] presented the distribution of the shortest path as a Gaussian process over the solution to an ordinary differential equation (ODE). This strategy offers novel ways to quantify and visualize uncertainty arising from the numerical computation and allow marginalization over a space of feasible solutions. Hauberg et al. [32] extended this work and incorporated data uncertainty in DTI by sub-sampling the diffusion gradients and solving the noisy ODE. Several other studies using the shortest path algorithms in fiber tracking can be found in the literature [31, 48].

4.2.2. STOCHASTIC METHODS

Describing the probability distribution analytically and propagating it through the pipeline is extremely difficult and often not feasible. The alternative and the most straight forward way to estimate the probability distribution function is to repeat the acquisition multiple times, this approach is called the bootstrap method [20]. However, for robust estimation of the PDFs, hundreds of data sets are required, which is not practical in a clinical setting. Several stochastic techniques were proposed to overcome this limitation [16]. Among them, the most widely used technique is wild bootstrapping [71].

WILD BOOTSTRAPPING

Wild bootstrapping requires only a single DTI scan at the expense of certain simplifying assumptions [40]. In Section 3.3, we described the fundamental principle behind diffusion modeling and specified how the diffusion tensor $\mathbf{D}$ is estimated using Equation 3.5. As mentioned in Section 3.3, the 6 unique elements of the diffusion tensor $\mathbf{D}$, can be estimated using ordinary least squares fitting method.

Once the matrix $\mathbf{D}$ is determined, the model predicted signal value $s'(\mathbf{g_i})$ can be calculated using Equation 3.1, which corresponds to the fitted tensor. A residual value $r(\mathbf{g_i})$ is then calculated with

$$r(\mathbf{g_i}) = s'(\mathbf{g_i}) - s(\mathbf{g_i}). \tag{4.1}$$

A new signal per orientation at each voxel, $s''(\mathbf{g_i})$, is then stochastically generated according to $s''(\mathbf{g_i}) = s(\mathbf{g_i}) + \text{sign}(r(\mathbf{g_i}))$, where the sign()-function randomly multiplies the residual by 1 or -1. A new tensor sample of the diffusion tensor, $\mathbf{D}'$, is estimated for each voxel independently multiple times by fitting a tensor to the generated $s''(\mathbf{g_i})$ signals. By perturbing residuals randomly, each tensor fit will be different from the previous one. This repetitive estimation of the tensor for each voxel is carried out for all voxels of the tensor volume multiple times, resulting in an ensemble of tensor volumes. The wild bootstrapping method generates multiple DTI volumes, enabling the estimation of uncertainty arising from acquisition noise and diffusion modeling. However, it is computationally expensive. To address this limitation, we introduce the Progressive Visual Analytics (PVA) pipeline, which will be explained in Chapter 5.

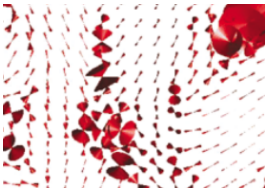

(a) Uncertainty cones [39].

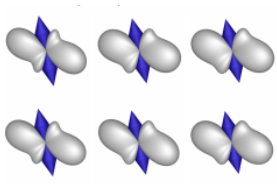

(b) HiFiVE Glyphs [64].

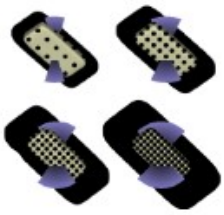

(c) Decomposed ensemble representation [76].

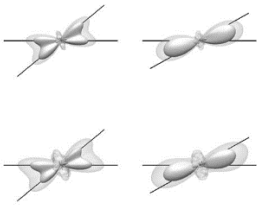

(d) ODF glyphs [67].

Figure 4.2: Glyphs with uncertainty encoding.

RANDOM SAMPLING

Another set of stochastic algorithms were introduced to incorporate uncertainty in fiber tracking by adding randomness in the tracking process [9, 61, 65]. These algorithms estimate the probability density function of the fiber orientation at each voxel and determine the propagation direction by drawing random samples from the distribution. This technique is preferable in most cases as it takes uncertainty into account and can estimate the confidence interval for each reconstructed pathway [8, 19]. Koch et al. [46] propose to use Monte Carlo random walks for the estimation of the fiber connectivity. The fiber tracking algorithm proceeds through each randomly selected neighboring voxel depending on the angle between the voxel's main eigenvector and its connecting angle with the neighboring voxels. A similar approach has been used in other studies to establish a connectivity map in a probabilistic sense [7, 10, 26, 57]. Monte Carlo methods have also been used to generate fiber tracks based on random particle movement [30]. The PDF obtained from the analytical methods can be used to perform tractography with these stochastic techniques [25, 37]. These studies are based on DTI, however, the concept is extendable to HARDI as well, but they are not used much in this context [49].

4.3. UNCERTAINTY VISUALIZATION

So far, we have discussed the sources of uncertainty present in the visualization pipeline and the methods used for their quantification. Visualization provides a way to communicate data effectively and efficiently, however, uncertainty is often omitted in the process. Visualizing uncertainty information in DWI can help assess the accuracy of the acquisition and modeling, which ultimately guide the users in making critical decision. However, the visualization of complex data in itself is not straightforward, adding uncertainty representation to it further complicates the process. Issues of visual cluttering

and loss of anatomical context are some of the few complications when visualizing uncertainties.

In this section, we will survey the strategies used for the visualization of the uncertainties in DTI and also discuss some related techniques used in the HARDI model. We also summarize these strategies in Table 4.1. The modeling column refers to the uncertainty quantification techniques, such as stochastic, bootstrapping, or analytical methods. Domain indicates the application area of the study and ensemble column categorizes the method into the local or global level. The representation specifies the measure used for the aggregations of the ensemble, and finally, the visualization column indicates the technique used to display the uncertainties. The visualization of uncertainty in DTI can roughly be divided into two categories.

1. Local uncertainty visualization
2. Global uncertainty visualization

4.3.1. LOCAL UNCERTAINTY VISUALIZATION

Local representations of the uncertainty depict variation per voxel inside the vector or tensor fields. Glyphs are typically used to depict the voxel-wise information of the data. Several glyph-based techniques have been proposed to visualize the inherent local uncertainty in DTI. Jones et al. [39] proposed a method to represent the confidence interval of the main fiber direction by rendering an uncertainty cone, as shown in figure 4.2a. Basser et al. [6] used a similar technique to represent the main eigenvector and their associated uncertainties. This visualization approach allows the representation of the main diffusion direction and the confidence interval concurrently, also desccribed in Table 4.1 Schultz et al. [64] demonstrate a new glyph design, called HiFiVE, that provides a more detailed impression of the uncertainty. It represents the variation corresponding to the main eigenvector by rendering a double cone (blue color) and the density estimation of the uncertainty around it (represented as a gray surface), as shown in Figure 4.2b.

Another way to represent the uncertainty in multivariate data is to estimate its covariance. It does not only express the variance in each coefficient but also indicates their linear dependencies. Since the diffusion tensor is a second-order tensor, its covariance is represented by a fourth-order tensor, however, the visualization of the fourth order tensor is rather difficult in this context. Basser et al. [5] presented a novel technique for the spectral decomposition of the fourth-order covariance tensor and introduced the concept of tensorial normal distribution. They proposed a glyph representation, called radial glyphs, which depicts the overall variance and a composite glyph for representing the eigentensor of the fourth-order covariance. They visualized the expected mean tensor and its standard deviation as three isosurfaces. Abbasloo et al. [1] highlight that the radial glyph does not convey the correlation with the mean tensor and also suffers from high visual complexity in the tensor field. They proposed a more intuitive approach for the visualization of the covariance by using multiple levels of detail. Unlike Basser et al., Abbasloo et al. visualize the confidence interval at each eigenmode separately by glyph overlays and used animation to visualize the differences at each mode. Gerrits et al. [27] pointed out the shortcoming in both of these visualization techniques and proposed a

generic approach that incorporates all the coefficients of the mean tensor and covariance in a single glyph.

Various studies has been published concerning the representation of the tensor ensemble directly. Jones et al. [42] visualize the ensemble data simply by overlaying several glyphs. Although the superposition depicts the overall picture of the data, it adds visual clutter and occlusion during display. To remedy this, Zhang et al. [75] used transparency to minimize the occlusion. Abbasloo et al. [1] tried to minimize this problem by rendering the superimposed glyphs in complementary colors. Zhang et al. [76] proposed an approach to decompose the tensor data into three properties (i.e., scale, shape, and orientation), representing the structure of the underlying fibers, and measure the variation per property. A glyph based representation has been presented in this study to visualize the ensemble effectively. The variation in the ensemble is represented by Halo and texture over the surface as shown in Figure 4.2c

The orientation distribution function (ODF), associated with HARDI, specifies the overall amount of diffusion in a given direction. Unlike the diffusion tensor model, ODFs can have multiple maxima, and therefore are capable of modeling complex fibrous structure more accurately than DTI. However, this technique is computationally expensive. The representation of the ODF itself is a challenging task and adding uncertainty information only increases the complexity. Jiao et al. [38] proposed a technique to visualize uncertainty over polar ODF glyphs by using a volume rendering technique. They introduced shape inclusion probability (SIP) function to represent the orientation uncertainty of the tensor. Tournier et al. [67] presented a method to visualize uncertainties associated with ODFs by using semitransparent glyphs. They represent the mean ODF by the opaque surface and the mean + standard deviation by the transparent surface, as shown in Figure 4.2d.

The visualization of uncertainty in a diffusion tensor is similar to the uncertainty representation in a vector field where orientation is considered important. Several glyph-based techniques exists in this scope. Wittenbrink et al. [73] presented a glyphs based representation of the uncertainty for atmospheric and oceanographic data. Likewise, Hlawatsch [34] and Lodha et al. [50] visualize the local uncertainty in a fluid flow field using glyph. Zuc et al. [78] proposed a glyph design to provide uncertainty information in a bidirectional vector field. These techniques rely on the representation of the vector direction and magnitude with encoded uncertainties to depict the local uncertainty present in the field.

4.3.2. GLOBAL UNCERTAINTY VISUALIZATION

In contrast to the local strategies, global uncertainty visualization in DTI aims at providing information on how accurate fiber tract information is throughout the complete tensor field, and how the inherent uncertainties accumulate during the tracking process. In DWI independently of DTI or HARDI models being used, probabilistic tractography is often used to incorporate these uncertainties. The most widely used approach to visualize fibers obtained through probabilistic tractography is to superimpose the resulting fibers in a so-called spaghetti plot [10, 18, 40], see Figure 4.3a. This visualization technique, however, does not depict a clear view of the region-wise fiber connections and its uncertainty and suffers from strong cluttering. Color coding the fiber tracts according to

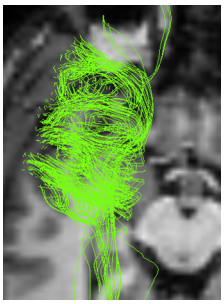

(a) Spaghetti plot [40].

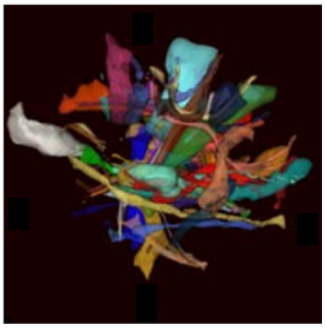

(b) Wrapped streamlines [15].

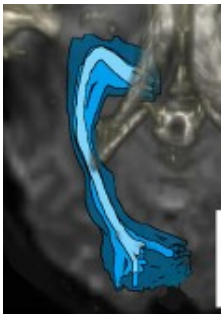

(c) Illustrative visualization [12].

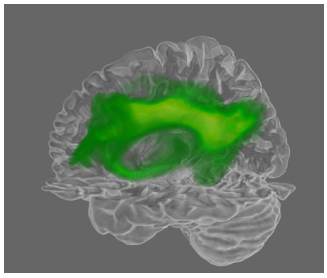

(d) Connectivity mapping [44].

Figure 4.3: Global uncertainty visualization strategies.

their seed points [18] does not suffice to minimize the complexity of the visualization. Schober et al. [62] and Hauberg et al. [32] used wobbly spaghetti plot that emphasize the fact that the individual resulting paths cannot be considered as real fibers in the brain which is a common misinterpretation in spaghetti plot. Instead, they are uncertain estimates of fibers.

To overcome the complexity and clutter caused by the multiple superimposed tracts, Enders et al. [22] presented a technique to group the fibers related to a certain nerve tract and generate a surface that wraps the resulting fibers. Similarly, Mehrof et al. [53] and Chen et al. [15] presented a method to cluster the fiber with a proximity-based algorithm and generate hulls encompassing the fiber bundles, as shown in Figure 4.3b. The anatomical grouping helps the user to understand the underlying fibrous structure. Outside of DTI, Frest et al. [23] used a similar technique to visualize uncertainty in flow field ensembles. They performed principal component analysis to cluster the streamlines in a low dimensional space and determine the mean and confidence interval in an ensemble. These representations are visualized with a line enclosed by a transparent surface. The geometrical hulls and enclosed surfaces reduce clutter, however, they cannot resolve complex cluster shapes. To alleviate these problems, Illustrative techniques have been proposed to represent the confidence interval of the fiber bundle by creating silhouette, outline, and contours [12, 56], as shown in Figure 4.3c.

To improve the understanding of ensembles of curves, it has been proposed to visualize the statistical information such as mean or confidence intervals rather than the direct ensemble visualization as spaghetti plot s. Table 4.1 indicates the various representations used by the studies. These representations, e.g mean and confidence interval, are the summarization of the raw samples. Unlike scalar values, the statistical measures are not well defined for curves, and therefore, several approaches have been proposed for the estimation of these terms. Brecheisen et al. [12] proposed to compute median and confidence intervals based on pre-selected distance measures between curves. In the field of fluid dynamics, a band-depth concept [51] has been introduced to analyze curve ensembles in two-dimensions [70] and three-dimensions [54]. This concept provides a way to determine centrality within the present curves and estimate the variations. Sanyal et al. [60] visualize the uncertainty in the wind trajectories by creating a ribbon along the ensemble mean. The width of a ribbon represents the variability at each point.

A widely used approach for the visualization of the global uncertainty is to represent and visualize measures derived from the probabilistic tractography. Voxel-wise fiber density computes the probability that a fiber tract traverses a voxel for a given seed region [14]. Voxel-wise fiber density [21, 30] helps to infer the anatomical connections. Another measure is the connectivity probability, which represents the probability of a fiber tract crossing a given voxel while connecting two fixed anatomical regions [63]. Von Kapri et al. [44] and McGraw et al. [52] used volume rendering for the visualization of density maps, as shown in Figure 4.3d. The global visualization of the fiber tracts does not provide the local tensor information. To visualize the local uncertainty along with the probabilistic tracts, a stream tube technique has been proposed [41, 72], which maps the local uncertainty measure onto the cross-section of the tube.

A common problem with the three-dimensional approaches is that the geometrical representation often occludes the underlying information, hampering its interpretation. Various slice-based methods have been proposed for the visualization of probabilistic fibers [46, 57]. These techniques have been used in neuroscience as they provide a way to directly visualize the anatomical information, making it easy to interpret anatomical context. Goldou et al. [28, 29] presented a novel slice based approach for visualizing the probability by rendering fiber stipples. The number of stipples, present at a particular region depicts the fiber density. Hlawitschka et al. [35] proposes to use poisson-disk sampling for the generation of the fiber stipples.

Table 4.1 summarizes the survey indicating the domain, representation, and visualization strategies used to display the uncertainty. The table covers the approaches used for local and global uncertainty visualization in both the DWI and non-DWI domain.

4.4. CONCLUSION

In this chapter, we explored uncertainty in the various stages of the DTI pipeline. Several of the problems and solutions discussed throughout this chapter are also valid for other models beyond Diffusion tensor, such as HARDI models. Even though we have not covered the technical background, where applicable, we have discussed the applicability of the strategies beyond DTI. Further, we have reviewed applicable uncertainty visualization techniques beyond the DWI domain.

DWI is still a growing field, considering the recent advancements and the frequent

development of new techniques, this survey should not be considered complete, it rather should be enhanced in the future. Studies on uncertainty visualization so far are mostly focused on the research aspect, however, no uncertainty visualization solution exists to specifically support clinical DTI pipeline. In the following chapters we present interactive visualization techniques that are specifically designed keeping clinical constraints and applicability in consideration.

Table 4.1: Summary of uncertainty representation and visualization strategies

References	Modeling	Domain	Ensemble	Representation	Visualization
Jones et al. [39]	Stochastic	DWI	Local	Direction interval	Interval glyph
Basser et al. [6]	Stochastic	DWI	Local	Direction interval	Interval glyph
Schultz et al. [64]	Stochastic	DWI	Local	Probability distribution	HIfive glyph
Jones et al. [42]	Stochastic	DWI	Local	Mean and median	Overlay glyph
Zhang et al. [76]	-	DWI	Local	Mean and variance	Halo and texture
Zhang et al. [75]	-	DWI	Local	Difference encoding	Overlay glyph
Tournier et al. [67]	Stochastic	DWI	Local	ODF mean and variance	Semi-transparent glyph
Jiao et al. [38]	Stochastic	DWI	Local	ODF SIP	Volume rendered glyph
Basser et al. [5]	Analytical	DWI	Local	Mean and covariance	Superimpose glyph
Abbasloo et al. [1]	Analytical	DWI	Local	Mean and covariance	Overlay/Animation glyph
Gerrits et al. [27]	Analytical	Both	Local	Mean and covariance	Superimpose glyph
Wittenbrink et al. [73]	Bootstrap	Non-DWI	Local	Mean and variance	Flow-field glyph
Zuk et al. [78]	Bootstrap	Non-DWI	Local	Probability distribution	Flow-field glyph
Hlawatsch et al. [34]	Bootstrap	Non-DWI	Local	Mean and variance	Flow-field glyph
Lodha et al. [50]	Bootstrap	Non-DWI	Local	Interval	Flow-field glyph
Otten et al. [56]	-	DWI	Global	Line and interval	Illustrative
Hermosilla et al. [33]	-	DWI	Global	Line and interval	Illustrative
Brecheisen et al. [12]	Stochastic	DWI	Global	Line and interval	Illustrative
Corouge et al. [18]	Bootstrap	DWI	Global	Ensembles	Spaghetti plot
Bjornemo et al. [10]	Stochastic	DWI	Global	Ensembles	Spaghetti plot
Jones et al. [40]	Stochastic	DWI	Global	Ensembles	Spaghetti plot
Hangmann et al. [30]	Stochastic	DWI	Global	Ensembles	Color-coded spaghetti plot
Ehricke et al. [21]	Stochastic	DWI	Global	Ensembles	Color-coded spaghetti plot
Enders et al. [22]	-	DWI	Global	Fiber clusters	Wrapped geometrical hull
Chen et al. [15]	-	DWI	Global	Fiber clusters	Wrapped geometrical hull
Merhof et al. [53]	-	DWI	Global	Fiber clusters	Wrapped geometrical hull
Jones et al. [41]	Bootstrap	DWI	Global	Ensemble/local estimates	Streamtubes
Wiens et al. [72]	Stochastic	DWI	Global	Ensemble/local estimates	Streamtubes
Goldau et al. [29]	Stochastic	DWI	Global	Fiber density	Stipples glyphs
Hlawitschka et al. [35]	Stochastic	DWI	Global	Fiber density	Stipples glyphs
Goldau et al. [28]	Stochastic	DWI	Global	Fiber density	Stipples glyphs
Brown et al. [14]	Stochastic	DWI	Global	Fiber density	Confidence region
Schultz et al. [63]	Stochastic	DWI	Global	Connectivity Probability	Confidence region
Kapri et al. [44]	-	DWI	Global	Connectivity Probability	Volume rendering
McGraw et al. [52]	Stochastic	DWI	Global	Connectivity Probability	Volume rendering
Koch et al. [46]	Stochastic	DWI	Global	Connectivity Probability	Density map
Parker et al. [57]	Stochastic	DWI	Global	Connectivity Probability	Density map
Kaden et al. [43]	Analytical	DWI	Global	Connectivity Probability	Density map
Schober et al. [62]	Analytical	DWI	Global	Ensembles	Wobbly Spaghetti plot
Hauberg et al. [32]	Analytical	DWI	Global	Ensembles	Wobbly spaghetti plot
Mirzargar et al. [54]	Bootstrap	Non-DWI	Global	Band Depth	Wrapped geometrical hull
Whitaker et al. [70]	Bootstrap	Non-DWI	Global	Band Depth	Contour lines
Ferstl et al. [23]	Bootstrap	Non-DWI	Global	Line and interval	Wrapped geometrical hull
Sanyal et al. [60]	Bootstrap	Non-DWI	Global	Mean and std. deviation	Ribbon

REFERENCES

[1] Amin Abbasloo et al. “Visualizing tensor normal distributions at multiple levels of detail”. In: *IEEE transactions on visualization and computer graphics* 22.1 (2015), pp. 975–984.

[2] Adam W Anderson. “Theoretical analysis of the effects of noise on diffusion tensor imaging”. In: *Magnetic Resonance in Medicine: An Official Journal of the International Society for Magnetic Resonance in Medicine* 46.6 (2001), pp. 1174–1188.

[3] Peter J Basser, James Mattiello, and Denis LeBihan. “Estimation of the effective self-diffusion tensor from the NMR spin echo”. In: *Journal of Magnetic Resonance, Series B* 103.3 (1994), pp. 247–254.

[4] Peter J Basser, James Mattiello, and Denis LeBihan. “MR diffusion tensor spectroscopy and imaging”. In: *Biophysical journal* 66.1 (1994), pp. 259–267.

[5] Peter J Basser and Sinisa Pajevic. “Spectral decomposition of a 4th-order covariance tensor: Applications to diffusion tensor MRI”. In: *Signal Processing* 87.2 (2007), pp. 220–236.

[6] Peter J. Basser. “Quantifying Errors in Fiber-Tract Direction and Diffusion Tensor Field Maps Resulting from MR Noise”. In: *Fifth Annual meeting of ISMRM, Vancouver*. 2007, p. 1740.

[7] Philipp G Batchelor et al. “Study of connectivity in the brain using the full diffusion tensor from MRI”. In: *Biennial International Conference on Information Processing in Medical Imaging*. Springer. 2001, pp. 121–133.

[8] Timothy EJ Behrens et al. “Characterization and propagation of uncertainty in diffusion-weighted MR imaging”. In: *Magnetic Resonance in Medicine: An Official Journal of the International Society for Magnetic Resonance in Medicine* 50.5 (2003), pp. 1077–1088.

[9] Timothy EJ Behrens et al. “Probabilistic diffusion tractography with multiple fibre orientations: What can we gain?” In: *Neuroimage* 34.1 (2007), pp. 144–155.

[10] Mats Björnemo et al. “Regularized stochastic white matter tractography using diffusion tensor MRI”. In: *International Conference on Medical Image Computing and Computer-Assisted Intervention*. Springer. 2002, pp. 435–442.

[11] Ralph Brecheisen. “Visualization of uncertainty in fiber tracking based on diffusion tensor imaging”. PhD thesis. Technische Universiteit Eindhoven, Department of Biomedical Engineering, 2012.

[12] Ralph Brecheisen et al. “Illustrative uncertainty visualization of DTI fiber pathways”. In: *The Visual Computer* 29.4 (2013), pp. 297–309.

[13] Ralph Brecheisen et al. “Parameter sensitivity visualization for DTI fiber tracking”. In: *IEEE Transactions on Visualization and Computer Graphics* 15.6 (2009), pp. 1441–1448.

[14] Colin J Brown, Brian G Booth, and Ghassan Hamarneh. “Uncertainty in tractography via tract confidence regions”. In: *Computational Diffusion MRI and Brain Connectivity*. Springer, 2014, pp. 129–138.

[15] Weri Chen et al. “Abstractive representation and exploration of hierarchically clustered diffusion tensor fiber tracts”. In: *Computer Graphics Forum*. Vol. 27. 3. Wiley Online Library. 2008, pp. 1071–1078.

[16] SungWon Chung, Ying Lu, and Roland G Henry. “Comparison of bootstrap approaches for estimation of uncertainties of DTI parameters”. In: *NeuroImage* 33.2 (2006), pp. 531–541.

[17] O Ciccarelli et al. “From diffusion tractography to quantitative white matter tract measures: a reproducibility study”. In: *Neuroimage* 18.2 (2003), pp. 348–359.

[18] Isabelle Corouge et al. “Fiber tract-oriented statistics for quantitative diffusion tensor MRI analysis”. In: *Medical image analysis* 10.5 (2006), pp. 786–798.

[19] Maxime Descoteaux et al. “Deterministic and probabilistic tractography based on complex fibre orientation distributions”. In: *IEEE transactions on medical imaging* 28.2 (2008), pp. 269–286.

[20] Bradley Efron and Robert J Tibshirani. *An introduction to the bootstrap*. CRC press, 1994.

[21] Hans-H Ehricke, Uwe Klose, and Wolfgang Grodd. “Visualizing MR diffusion tensor fields by dynamic fiber tracking and uncertainty mapping”. In: *Computers & Graphics* 30.2 (2006), pp. 255–264.

[22] Frank Enders et al. *Visualization of white matter tracts with wrapped streamlines*. IEEE, 2005.

[23] Florian Ferstl, Kai Bürger, and Rüdiger Westermann. “Streamline variability plots for characterizing the uncertainty in vector field ensembles”. In: *IEEE Transactions on Visualization and Computer Graphics* 22.1 (2015), pp. 767–776.

[24] Luc Florack, Tom Dela Haije, and Andrea Fuster. “Direction-controlled DTI interpolation”. In: *Visualization and Processing of Higher Order Descriptors for Multi-Valued Data*. Springer, 2015, pp. 149–162.

[25] Ola Friman, Gunnar Farneback, and C-F Westin. “A Bayesian approach for stochastic white matter tractography”. In: *IEEE transactions on medical imaging* 25.8 (2006), pp. 965–978.

[26] Daniel Gembris, Helmut Schumacher, and Dieter Suter. “Solving the diffusion equation for fiber tracking in the living human brain”. In: *Proc. of the International Society for Magnetic Resonance Medicine (ISMRM)*. Vol. 9. 2001, p. 1529.

[27] Tim Gerrits, Christian Rössl, and Holger Theisel. “Towards Glyphs for Uncertain Symmetric Second-Order Tensors”. In: *Computer Graphics Forum*. Vol. 38. 3. Wiley Online Library. 2019, pp. 325–336.

[28] Mathias Goldau and Mario Hlawitschka. “Multi-modal visualization of probabilistic tractography”. In: *Visualization in Medicine and Life Sciences III*. Springer, 2016, pp. 195–218.

[29] Mathias Goldau et al. “Fiber stippling: An illustrative rendering for probabilistic diffusion tractography”. In: *2011 IEEE Symposium on Biological Data Visualization (BioVis)*. IEEE. 2011, pp. 23–30.

[30] Patric Hagmann et al. “DTI mapping of human brain connectivity: statistical fibre tracking and virtual dissection”. In: *Neuroimage* 19.3 (2003), pp. 545–554.

[31] Xiang Hao, Ross T Whitaker, and P Thomas Fletcher. “Adaptive Riemannian metrics for improved geodesic tracking of white matter”. In: *Biennial International Conference on Information Processing in Medical Imaging*. Springer. 2011, pp. 13–24.

[32] Søren Hauberg et al. “A random riemannian metric for probabilistic shortest-path tractography”. In: *International Conference on Medical Image Computing and Computer-Assisted Intervention*. Springer. 2015, pp. 597–604.

[33] Pedro Hermosilla et al. “Uncertainty visualization of brain fibers”. In: (2012).

[34] Marcel Hlawatsch et al. “Flow radar glyphs—static visualization of unsteady flow with uncertainty”. In: *IEEE Transactions on Visualization and Computer Graphics* 17.12 (2011), pp. 1949–1958.

[35] Mario Hlawitschka et al. “Hierarchical Poisson-disk sampling for fiber stipples”. In: (2013).

[36] Hao Huang et al. “Analysis of noise effects on DTI-based tractography using the brute-force and multi-ROI approach”. In: *Magnetic Resonance in Medicine: An Official Journal of the International Society for Magnetic Resonance in Medicine* 52.3 (2004), pp. 559–565.

[37] Saad Jbabdi et al. “A Bayesian framework for global tractography”. In: *Neuroimage* 37.1 (2007), pp. 116–129.

[38] Fangxiang Jiao et al. “Uncertainty visualization in HARDI based on ensembles of ODFs”. In: *2012 IEEE Pacific Visualization Symposium*. IEEE. 2012, pp. 193–200.

[39] Derek K Jones. “Determining and visualizing uncertainty in estimates of fiber orientation from diffusion tensor MRI”. In: *Magnetic Resonance in Medicine: An Official Journal of the International Society for Magnetic Resonance in Medicine* 49.1 (2003), pp. 7–12.

[40] Derek K Jones. “Tractography gone wild: probabilistic fibre tracking using the wild bootstrap with diffusion tensor MRI”. In: *IEEE transactions on medical imaging* 27.9 (2008), pp. 1268–1274.

[41] Derek K Jones et al. “PASTA: pointwise assessment of streamline tractography attributes”. In: *Magnetic Resonance in Medicine: An Official Journal of the International Society for Magnetic Resonance in Medicine* 53.6 (2005), pp. 1462–1467.

[42] Derek K Jones et al. “Spatial normalization and averaging of diffusion tensor MRI data sets”. In: *Neuroimage* 17.2 (2002), pp. 592–617.

[43] Enrico Kaden, Thomas R Knösche, and Alfred Anwander. “Parametric spherical deconvolution: inferring anatomical connectivity using diffusion MR imaging”. In: *NeuroImage* 37.2 (2007), pp. 474–488.

[44] Anette von Kapri et al. “Evaluating a visualization of uncertainty in probabilistic tractography”. In: *Medical Imaging 2010: Visualization, Image-Guided Procedures, and Modeling*. Vol. 7625. International Society for Optics and Photonics. 2010, p. 762534.

[45] Maurice George Kendall et al. “The advanced theory of statistics. Vols. 1.” In: *The advanced theory of statistics. Vols. 1*. 1.Ed. 4 (1948).

[46] Martin A Koch, David G Norris, and Margret Hund-Georgiadis. “An investigation of functional and anatomical connectivity using magnetic resonance imaging”. In: *Neuroimage* 16.1 (2002), pp. 241–250.

[47] Mariana Lazar and Andrew L Alexander. “An error analysis of white matter tractography methods: synthetic diffusion tensor field simulations”. In: *Neuroimage* 20.2 (2003), pp. 1140–1153.

[48] Christophe Lenglet, Rachid Deriche, and Olivier Faugeras. “Inferring white matter geometry from diffusion tensor MRI: Application to connectivity mapping”. In: *European Conference on Computer Vision*. Springer. 2004, pp. 127–140.

[49] Ronghua Liang et al. “Visual exploration of HARDI fibers with probabilistic tracking”. In: *Information Sciences* 330 (2016), pp. 483–494.

[50] Suresh K Lodha et al. “UFLOW: Visualizing uncertainty in fluid flow”. In: *Proceedings of Seventh Annual IEEE Visualization'96*. IEEE. 1996, pp. 249–254.

[51] Sara López-Pintado et al. “Simplicial band depth for multivariate functional data”. In: *Advances in Data Analysis and Classification* 8.3 (2014), pp. 321–338.

[52] Tim McGraw and Mariappan Nadar. “Stochastic DT-MRI connectivity mapping on the GPU”. In: *IEEE transactions on visualization and computer graphics* 13.6 (2007), pp. 1504–1511.

[53] Dorit Merhof et al. “Isosurface-based generation of hulls encompassing neuronal pathways”. In: *Stereotactic and functional neurosurgery* 87.1 (2009), pp. 50–60.

[54] Mahsa Mirzargar, Ross T Whitaker, and Robert M Kirby. “Curve boxplot: Generalization of boxplot for ensembles of curves”. In: *IEEE transactions on visualization and computer graphics* 20.12 (2014), pp. 2654–2663.

[55] Lauren O'Donnell, Steven Haker, and Carl-Fredrik Westin. “New approaches to estimation of white matter connectivity in diffusion tensor MRI: Elliptic PDEs and geodesics in a tensor-warped space”. In: *International Conference on Medical Image Computing and Computer-Assisted Intervention*. Springer. 2002, pp. 459–466.

[56] Ron Otten, Anna Vilanova, and Huub Van De Wetering. “Illustrative white matter fiber bundles”. In: *Computer Graphics Forum*. Vol. 29. 3. Wiley Online Library. 2010, pp. 1013–1022.

[57] Geoffrey JM Parker, Hamied A Haroon, and Claudia AM Wheeler-Kingshott. “A framework for a streamline-based probabilistic index of connectivity (PICo) using a structural interpretation of MRI diffusion measurements”. In: *Journal of Magnetic Resonance Imaging: An Official Journal of the International Society for Magnetic Resonance in Medicine* 18.2 (2003), pp. 242–254.

[58] Timo Roine et al. “Isotropic non-white matter partial volume effects in constrained spherical deconvolution”. In: *Frontiers in neuroinformatics* 8 (2014), p. 28.

[59] Lauren E Salminen et al. “Reducing CSF partial volume effects to enhance diffusion tensor imaging metrics of brain microstructure”. In: *Technology and innovation* 18.1 (2016), p. 5.

[60] Jibonananda Sanyal et al. “Noodles: A tool for visualization of numerical weather model ensemble uncertainty”. In: *IEEE Transactions on Visualization and Computer Graphics* 16.6 (2010), pp. 1421–1430.

[61] Tabinda Sarwar, Kotagiri Ramamohanarao, and Andrew Zalesky. “Mapping connectomes with diffusion mri: deterministic or probabilistic tractography?” In: *Magnetic resonance in medicine* 81.2 (2019), pp. 1368–1384.

[62] Michael Schober et al. “Probabilistic shortest path tractography in DTI using Gaussian Process ODE solvers”. In: *International Conference on Medical Image Computing and Computer-Assisted Intervention*. Springer. 2014, pp. 265–272.

[63] Thomas Schultz, Holger Theisel, and Hans-Peter Seidel. “Topological visualization of brain diffusion MRI data”. In: *IEEE Transactions on Visualization and Computer Graphics* 13.6 (2007), pp. 1496–1503.

[64] Thomas Schultz et al. “HiFiVE: a hilbert space embedding of fiber variability estimates for uncertainty modeling and visualization”. In: *Computer Graphics Forum*. Vol. 32. 3pt1. Wiley Online Library. 2013, pp. 121–130.

[65] J Donald Tournier, Fernando Calamante, and Alan Connelly. “Improved probabilistic streamlines tractography by 2nd order integration over fibre orientation distributions”. In: *Proceedings of the international society for magnetic resonance in medicine*. Vol. 18. Ismrm. 2010, p. 1670.

[66] J-D Tournier et al. “Limitations and requirements of diffusion tensor fiber tracking: an assessment using simulations”. In: *Magnetic Resonance in Medicine: An Official Journal of the International Society for Magnetic Resonance in Medicine* 47.4 (2002), pp. 701–708.

[67] J-Donald Tournier et al. “Direct estimation of the fiber orientation density function from diffusion-weighted MRI data using spherical deconvolution”. In: *NeuroImage* 23.3 (2004), pp. 1176–1185.

[68] Sjoerd B Vos et al. “Partial volume effect as a hidden covariate in DTI analyses”. In: *Neuroimage* 55.4 (2011), pp. 1566–1576.

[69] Setsu Wakana et al. “Fiber tract–based atlas of human white matter anatomy”. In: *Radiology* 230.1 (2004), pp. 77–87.

[70] Ross T Whitaker, Mahsa Mirzargar, and Robert M Kirby. “Contour boxplots: A method for characterizing uncertainty in feature sets from simulation ensembles”. In: *IEEE Transactions on Visualization and Computer Graphics* 19.12 (2013), pp. 2713–2722.

[71] Brandon Whitcher et al. “Using the wild bootstrap to quantify uncertainty in diffusion tensor imaging”. In: *Human brain mapping* 29.3 (2008), pp. 346–362.

[72] Vitalis Wiens et al. “Visualizing Uncertainty in HARDI Tractography Using Superquadric Streamtubes.” In: *EuroVis (Short Papers)*. 2014.

[73] Craig M Wittenbrink, Alex T Pang, and Suresh K Lodha. “Glyphs for visualizing uncertainty in vector fields”. In: *IEEE transactions on Visualization and Computer Graphics* 2.3 (1996), pp. 266–279.

[74] Feng Yang et al. “A comparative study of different level interpolations for improving spatial resolution in diffusion tensor imaging”. In: *IEEE journal of biomedical and health informatics* 18.4 (2014), pp. 1317–1327.

[75] Changgong Zhang et al. “Glyph-based comparative visualization for diffusion tensor fields”. In: *IEEE transactions on visualization and computer graphics* 22.1 (2015), pp. 797–806.

[76] Changgong Zhang et al. “Overview+ detail visualization for ensembles of diffusion tensors”. In: *Computer Graphics Forum*. Vol. 36. 3. Wiley Online Library. 2017, pp. 121–132.

[77] Zhenyu Zhou et al. “Automated artifact detection and removal for improved tensor estimation in motion-corrupted DTI data sets using the combination of local binary patterns and 2D partial least squares”. In: *Magnetic resonance imaging* 29.2 (2011), pp. 230–242.

[78] Torre Zuk et al. “Exploration of uncertainty in bidirectional vector fields”. In: *Visualization and Data Analysis 2008*. Vol. 6809. International Society for Optics and Photonics. 2008, 68090B.

5

A Progressive Approach for Uncertainty Visualization in Diffusion Tensor Imaging

The previous chapter has provided an overview of the different sources of uncertainty occurring in the DTI processing pipeline. In this chapter, we focus on the uncertainty in the first two stages of the pipeline, i.e., uncertainty that arises due to acquisition noise and errors in diffusion modeling. We propose an approach that addresses the high computational and memory costs of using wild-bootstrapping as uncertainty estimation by providing a progressive visual analytics paradigm. We present a local bootstrapping strategy, and provide fiber-tracking results in a progressive manner. We have also implemented a progressive aggregation technique that computes the distances in the fiber ensemble during progressive bootstrap computations. We present experiments with different scenarios to highlight the benefits of using our progressive visual analytic pipeline in a clinical workflow along with a use case and analysis obtained by discussions with our collaborators. This chapter is based on the paper:

Siddiqui, F., Höllt, T., and Vilanova, A. (2021, June). A progressive approach for uncertainty visualization in diffusion tensor imaging. In Computer Graphics Forum (Vol. 40, No. 3, pp. 411-422).
https://doi.org/10.1111/cgf.14317.

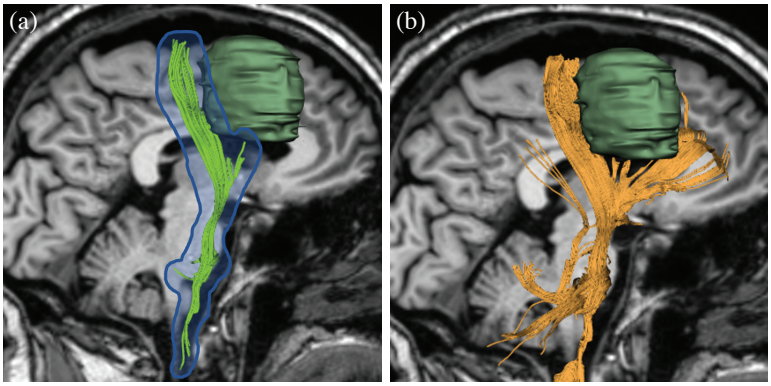

Figure 5.1: (a) Sagittal MRI slice showing a segmented frontal brain tumor (dark green) and deterministic streamline based fiber tracking of the nearby corticospinal tract. A fixed safety margin is drawn as an outline in blue. (b) 150 wild bootstrapping [12] iterations using the same parameters and region of interest as a), resulting in additional frontal and cerebellar pathways.

5.1. INTRODUCTION

The MRI-based acquisition suffers from artifacts such as noise, image distortion, motion artifacts, and partial volume effects (PVE) [1]. The modeling stage involves the estimation of the second order tensor using fitting techniques or higher-order regression models, adding further variation to the final results [13]. These uncertainties accumulate variations in the resulting visualization, influencing the decision making process.

In clinical applications, the visualization of uncertainty is often ignored, thereby hampering the user to make effective decisions. In the absence of uncertainty information, neurosurgeons may consider safety margins around critical brain structures [20] based on experience and prior knowledge (see Figure 5.1a). Such safety margins assume that there is a homogeneous distribution of the uncertainty, which is not the case (see Figure 5.1b). Uncertainty information becomes even more critical when fiber tracking is used in pathological anatomy, e.g., when fiber tracts are displaced or infiltrated by a tumor. In such cases, the experience and anatomical knowledge of the surgeon to estimate the uncertainty becomes even less effective. Figure 5.1 shows a fiber bundle affected by a tumor present in its vicinity. As can be seen, deterministic fiber tracking as used in the clinical workflow could not show the fibers going towards the frontal area of the tumor (Figure 5.1b). Missing the possibility that fibers can be in the frontal area of the tumor can lead to inadvertently damaging of the tracts during the surgery.

Wild bootstrapping is a stochastic method, used to approximate uncertainty in DTI. It approximates regular bootstrapping where multiple acquisitions are acquired [22] to model uncertainty. Wild bootstrapping requires only a single scan and simulates multiple acquisitions using probability distributions from the residuals that remain after fitting the diffusion tensors to the data. Computing a large number of such simulated scans allows to approximate a distribution, from which the output, together with its uncertainty, can be derived. This procedure, however, incurs substantial computational costs

and is difficult to be used in an interactive fiber tracking process, where parameters are defined through exploratory trial-and-error which is the current clinical workflow for the definition of fiber tracts in surgery planning. We propose a progressive approach that allows interactive estimation and exploration of fiber tracts and their corresponding uncertainty without pre-processing the data.

Wild bootstrapping provides an ensemble of fiber tracts (i.e., polylines) that cannot be effectively visualized directly. Aggregation strategies are used to effectively visualize this kind of data [2, 21]. However, these methods are not efficient when ensemble members are progressively generated. We modified an existing solution by Brecheisen et al. [2], to allow progressive fiber generation and synchronized visualization. The main contribution of this paper is a progressive visual analytics framework for stochastic based uncertainty visualization in DTI fiber tracking. The main aspects in this contribution are listed below:

- We have developed a progressive visual analytics (PVA) pipeline for local calculation of tensor bootstrap samples combined with simultaneous fiber tracking.
- We have adapted the ensemble-based fiber tract aggregation and visualization to work in a progressive framework.

The framework enables interactive generation, and visual analysis of fiber tracts with uncertainties. We analyze the computational benefits through experiments and illustrate the potential of the framework by a set of use-cases.

5.2. REQUIREMENT ANALYSIS

This work has been carried out in collaboration with clinical partners who want to incorporate uncertainty into their current tractography workflow for neurosurgery planning. We base our visualization pipeline on the methods used in their current workflow, which incorporates diffusion tensor imaging (DTI), combined with deterministic streamline generation of fiber tracts. While more sophisticated methods exist for modeling the diffusion, as well as fiber tracking, our proposed solution must work with the diffusion tensor model as well as deterministic fiber tract generation to maximize compatibility with the current clinical workflow. After acquisition and pre-processing of the data, radiologists define a region of interest (ROI) and generate the corresponding fiber bundle. Further, the proposed solution should minimize the time between acquisition and analysis. Therefore, we propose a progressive visual analytics (PVA) approach to generating the underlying bootstrap samples, as well as deriving fiber tracts. The proposed PVA pipeline is designed to allow the interactive estimation of uncertainty in the tractography and enables clinicians to define the regions of interest and explore the results interactively.

5.3. RELATED WORK

Several approaches are available in the literature that characterize, represent, and visualize uncertainties due to noise and modeling errors in fiber tracking, each with their own pros and cons. In this section, we present related work according to uncertainty estimation methods for fiber tracking and corresponding uncertainty visualization techniques.

To represent the error distribution within a fiber ensemble, statistical information, such as mean or confidence interval, are of interest. However, these measures are not as well defined for the curves as they are for scalar values. Several approaches to compute these statistical information for ensembles of curves exist. Whitaker et al. [21] and Mirzagar et al. [15] use the concept of band-depth to compute the centrality within the set of curves and estimate the variations. Ender et al. [6] compute the average of the curves in a bundle, resulting in the central fiber. Instead of computing the mean of the fibers, Brecheisen et al. [2] compute the median and confidence interval of the curve by calculating the distances among fiber pairs based on a chosen measure. This approach enables the visualization of the complex fiber structure along with the uncertainty information. Here, we adopt a similar technique to calculate the most representative fiber and the percentile of variation and modify it such that it can be incorporated in a progressive visualization framework.

In our work, we address computational cost and latency issues that are part of the uncertainty visualization pipeline for DTI fiber tracking. We base our approach on wild bootstrapping and streamline fiber tracking that we adapt the the Progressive Visual Analytics (PVA) paradigm introduced by Mühlbacher et al. and Stolper et al. [17, 19] and later formalized by Fekete and Primet [8]. PVA provides intermediate results that help users to understand the evolution of a lengthy computation, such as the wild bootstrapping simulation, allowing to start the exploration of the data during the computation without a need to wait until the end of the simulation. Further, PVA allows steering the computations, similar to interactive program steering [9] and computational steering [11] approaches. Here, we introduce progressive generation and aggregation of the fiber samples combined with immediate, interactive uncertainty visualization. To the best of our knowledge, there is no related work that proposes using a progressive strategy for the purpose of uncertainty visualization in DTI fiber tracking.

5.4. TOWARDS A PROGRESSIVE VISUAL ANALYTICS PIPELINE

In our work we focus on stochastic methods that simulate sample variations and facilitate the propagation through the pipeline. We have chosen wild bootstrapping for the presented framework to estimate and propagate the uncertainty in the data acquisition and diffusion modeling steps from a single DTI scan. Wild bootstapping method is explained in detail in Section 4.2.2. We have chosen wild bootstraping for our framework given its use and demonstrated similarity to bootstraping in the DTI context [12]. The naive pipeline is based on pre-computing the ensemble of tensor volumes followed by deterministic fiber-tracking, i.e., streamline generation (see Figure 5.2). For each tensor volume sample and a seed point, a new fiber sample is generated. Once all the fiber samples are tracked, we obtain a fiber ensemble to be visualized. This process is able to show the variations in the obtained fiber tracts. However, the pre-computation of the whole tensor volumes ensemble requires long computation times and a large memory footprint.

Accessibility within the clinical workflow is a major limitation for the use and evaluation of uncertainty information in practice. The lack of availability of the tools and the complexity in achieving the visualization of the uncertainty is one of the main bottlenecks in their clinical use, despite its enormous potential. In neurosurgical applications,

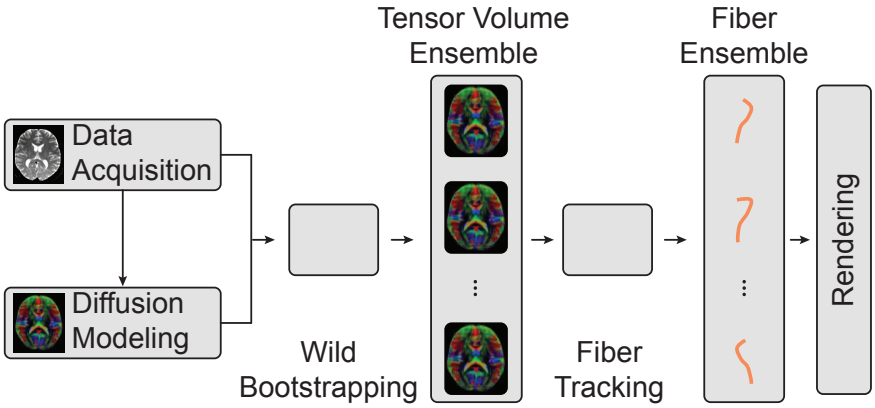

Figure 5.2: Standard wild bootstrapping and deterministic fiber tracking approach, pre-computing the tensor volume ensemble.

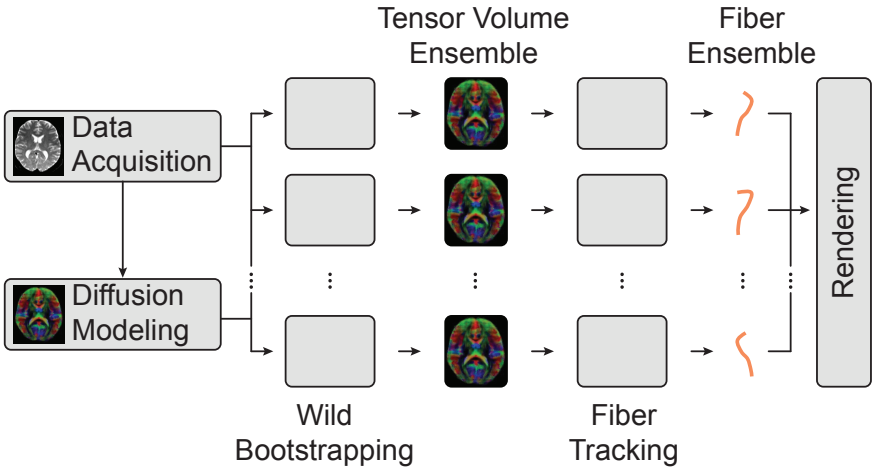

Figure 5.3: Processing pipeline of naive progressive approach, creating a complete volume per iteration.

for example, in pre-surgical planning, generating the fiber pathways is often a trial and error process. It needs various iteration and requires constant tuning of fiber tracking regions of interest and parameters to meet the expectations of the clinician. The large preprocessing times of uncertainty modeling add latency in the visualization which breaks the clinical workflow. We introduce a progressive approach that reduces the latency between acquisition and visualization and allow users to explore and interact with fiber tracking parameters and their uncertainties directly during the computations. We identify and the bottlenecks present in the clinical workflow and provides a first step towards making uncertainty visualization more accessible to the user. We do realise that our proposed approach needs clinical validation and evaluation, just as tractography does in general. However, we consider a clinical evaluation as future work.

In uncertainty modeling through bootstrapping, it is not known in advance how many bootstrap samples will lead to an accurate enough result. Many factors, including the shape of the bundles themselves, the area of the brain and the level of noise and artifacts introduce variation in the number of required samples. Modeling uncertainty for one bundle may require fewer bootstrap iterations than another. Computing a predefined number of iterations 'N', either misrepresents the uncertainty or wastes resources and time. To circumvent this problem, a progressive visualization approach allows the user to see intermediate results, observe the uncertainty simulation's evolution, and ultimately identify when the results are stable enough on-the-fly, saving valuable time.

In the following, we start our discussion with a naive progressive visual analytic pipeline, identify drawbacks, and proceed to our proposed local bootstrapping and fiber tracking approach.

5.4.1. NAIVE PROGRESSIVE APPROACH

The first step towards a progressive visual analytics pipeline is to visualize the fiber samples during the wild bootstrapping calculations without a need to pre-compute all tensor volumes. For this purpose, bootstrap sample calculation and fiber tracking stage are combined. Figure 5.3 illustrates the pipeline of the naive progressive bootstrapping and fiber tracking approach for a given seed point. In the progressive approach, a tensor volume is generated at each iteration by using the wild bootstrap technique. Based on the newly created sample, fiber tracking from a given seed point is performed. Each iteration results in a unique fiber sample, which can directly be visualized. The variations in the fiber samples represent the effect of the noise and modeling errors. The bootstrap iterations repeat continuously which increases the reliability in the estimation of the uncertainty. The user can start the evaluation of the data immediately and define when to take a decision given a perceived visual stability of the results.

The progressive approach reduces the memory footprint of the wild-bootstrapping method, as no pre-computed tensor volumes need to be stored. However, computing each complete diffusion tensor volume takes in the order of several seconds, which is still too long to be used in an interactive system, making this progressive pipeline impractical.

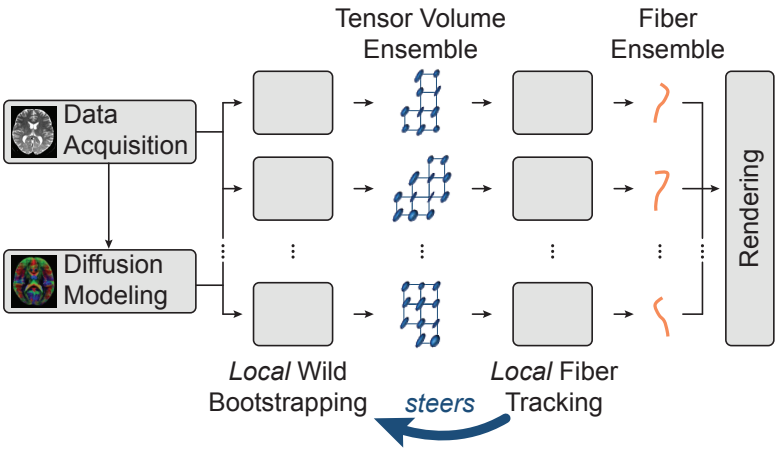

Figure 5.4: Processing pipeline of local bootstrapping and fiber tracking.

5.4.2. LOCAL BOOTSTRAPPING AND FIBER TRACKING

In most applications of fiber tracking, the users are mostly interested in a specific fiber bundle or a particular region of the brain. In these cases, calculating the bootstrap sample for the whole volume is a large waste of computation resources, since just a small portion will be used. However, the precise region of interest for the tracing is not known in advance, and cannot be computed in pre-processing time. Taking this into consideration, we propose a novel approach for accelerating the computations of the progressive bootstrap method presented in previous section. Here, we combine wild bootstrapping with fiber tracking and the computations are performed only for those cells that are necessary for the currently tracked fiber. The pipeline for the local bootstrapping and fiber tracking is illustrated in Figure 5.4.

The streamline algorithm is initiated with specific seed points. During the numerical integration of the corresponding streamlines, we need to obtain the diffusion tensor that defines the vector field at a specific position in the volume. We use tensor component-wise trilinear interpolation [5] for the estimation of the diffusion tensor at any point in the volume. For trilinear interpolation, we need the diffusion tensors at the eight voxels of the cell containing the current position. These voxel tensor values are determined by performing wild bootstrapping calculations at the specific voxels as described in Section 4.2.2. While tracing the streamlines in a single bootstrap sample, we keep track of the voxels that have been already computed and store the corresponding tensor wild-bootstraping sample. Every time a previously computed voxel is required, it is fetched, without the need for re-computation. This ensures coherence through the streamline integration steps. We also reuse the stored voxel tensors within a wild-bootstrapping iteration when fiber samples from different seed points are traced. This preserves the coherence between fibers, and produces the same results as the naive pipeline.

The resulting fiber samples (shown by the red lines in Figure 5.4) are then progressively visualized after being calculated. The bootstrap iterations repeat, resulting in multiple fiber samples for each seed point.

5.5. UNCERTAINTY VISUALIZATION

So far, we have discussed a method to progressively generate bootstrap fiber samples. This progressiveness has no use if we cannot visualize the resulting fiber ensemble in an effective and progressive manner. Directly rendering thousands of fiber samples in a spaghetti plot adds cluttering and occlusion, making it difficult to effectively obtain relevant information. We developed a progressive aggregation method to indicate the relevant uncertainty information, and an interactive visualization approach for effective exploration of the uncertainties.

5.5.1. PROGRESSIVE FIBER AGGREGATION

Many techniques for effective visualization of uncertainty in curve-like ensemble data sets have been reported in literature [2, 3, 6, 14]. Most of these techniques, rely on the availability of the complete data to create uncertainty aggregations similar to a boxplot (e.g., median fiber, outliers, bounds definition) [2, 15, 21]. The progressive fiber generation and simultaneous visualization in our work pose extra challenges to the application of such methods. In our approach, each bootstrap iteration generates a new fiber sample that is added to the existing ensemble. Consequently, the uncertainty aggregation needs to be updated after every bootstrap iteration. An efficient method for aggregation that can be iteratively updated, rather than requiring a full re-computation from scratch with every added sample is desired. The existing algorithms for aggregation rely on sorting and ordering based on distance calculations between fibers. Making such calculations progressive is not straight forward. In the following, we adapt the work by Brecheisen et al. [2] to the progressive context.

Brecheisen et al. proposed to determine a representative fiber using pairwise distances between all fiber samples. The representative fiber is the fiber with the minimum accumulated distance to all the other fibers in the ensemble and as such can be seen as the most central fiber. In addition, all other fibers are ordered according to their accumulated distances such that intervals of uncertainty can be defined.

To calculate the pairwise distances, Brecheisen et al. [2] used the mean of the closest point distance [16]. We modify this approach presented by Brecheisen et al. to be used within the scope of a progressive approach as follows.

We assign a distance score S_i to each fiber sample F_i which is the accumulated distance of F_i to all other available fiber samples as

$$S_i = \sum_{j \neq i}^{N} d(F_i, F_j), \tag{5.1}$$

where d defines a distance measure between fibers, in our case the closest point distance. With each bootstrap iteration, a new fiber sample F_k is generated and added. As the distance score S_i is a simple sum it can be updated easily. We only have to compute $d(F_i, F_k)$ for each already computed fiber sample F_i and add it to the corresponding existing distance score S_i. Additionally, S_k is computed by summation of all newly computed $d(F_i, F_k)$ using Equation 5.1. We keep the scores in an sorted table such that the lowest score, corresponding to the sample that has a minimum distance to all the others, is selected as the representative fiber. Higher scores indicate that the samples are further

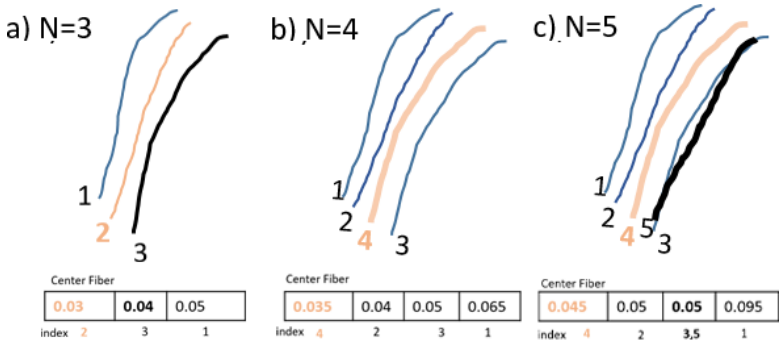

Figure 5.5: Updates in a confidence score table with an inclusion of a new fiber sample at each iteration.

away from the rest and can be interpreted as having higher uncertainty. Despite being of linear order, the computation of $d(F_i, F_k)$ is computationally costly. Therefore, we progressively update the existing distance scores, as well as the new distance score S_k, in order of the distance score of the fiber samples. Furthermore, to avoid unnecessary distance computations, if the distance $d(F_i, F_k)$ is smaller than a pre-defined threshold, we assume that the fiber samples F_i and F_k are similar enough to not need a higher precision in the distance calculation. By keeping track of all computed distances, we can avoid the costly distance calculations $d(F_j, F_k)$ for the remaining samples F_j, by simply using the existing distance $d(F_j, F_i)$.

We illustrate the progressive updates of the distance score table in Figure 5.5. After the third iteration ($N = 3$, Figure 5.5a), three fiber samples are present with the second sample as the center line. During the fourth iteration ($N = 4$, Figure 5.5b), a new sample is added to the existing ones. The distance scores are re-computed and the representative fiber is updated accordingly. At $N = 5$ (Figure 5.5c), another sample is added with a distance less than a predetermined threshold to the existing fiber sample 3. In this case, the distance score table is updated according to the distances of the similar fiber and the new fiber is added to the same table entry as sample 3. Notice that the more fiber samples we calculate the higher the costs of keeping the score table but also the higher the chance of finding a similar fiber sample. An evaluation on the performance gain and the accuracy is presented in section 7.

5.5.2. PROGRESSIVE RENDERING

Once the representative fiber and the aggregations have been determined, an effective visualization is needed. We draw the representative fibers as red tubes and the remaining fiber samples, representing the ensemble variation, as illuminated polylines in orange. We use multi-layered rendering to avoid occlusion of the representative fibers by the other fiber samples. We first render the fiber samples, followed by a second pass to render the representative fibers on top, as shown in Figure 5.7.

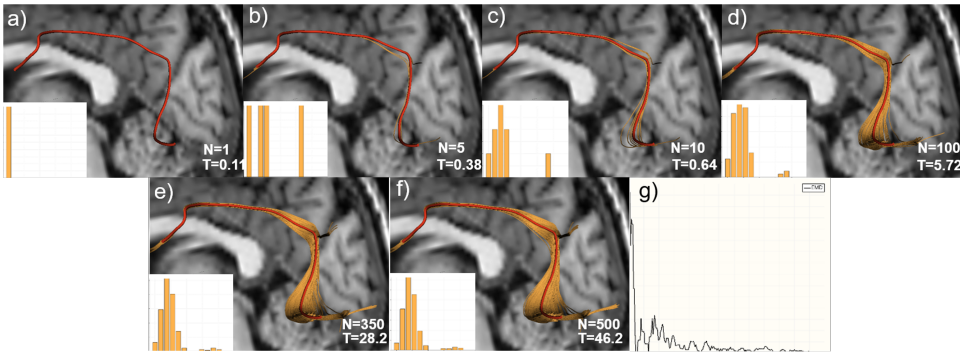

Figure 5.6: Progressive simulation and visualization of a single fiber, originating from Arcuate Fasciculus showing the histogram and convergence behaviour of the simulation. a) to f) show the results of the simulation after N iterations. T represents the total elapsed time of the simulation in seconds. g) shows the histogram stability plot.

In this way, the representative fibers are always visible, regardless of occlusion by other fiber samples As a result, the depth perception of those samples in relation to the representative fibers is less clear. However, we deem the visibility of the representative fibers more important, while the fiber samples provide context.

As the simulation progresses, changes of the representative fiber and fiber samples can be observed by the user in the progressively updating visualization. For further exploration of the fiber aggregation, intervals can be specified similar to the work by Brecheisen et al. [2] to show variation from the representative fiber. An interval can be expressed as a percentage range of the distance score table, e.g., $0-50\%$ closest fiber samples. The selected fiber samples are rendered in blue. We have chosen the color scheme for the representative fiber, fiber samples and selection, using the red to blue diverging color map from ColorBrewer [10]. By using colors from one end of the color map for the representative fiber and fiber samples we indicate their connection, while using the other end for the selection provides a clear highlight.

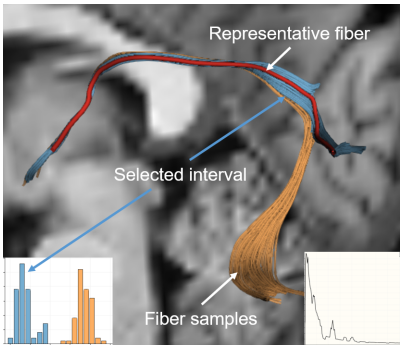

Figure 5.7: Visualization with multi-layered rendering. Representative fibers are rendered on the top layer, followed by the selected interval and fiber samples at the bottom. The histogram widget shows the selected interval, while the line plot shows the Earth Mover's Distance (EMD) between the last two consecutive histograms plotted against the number of iterations.

To draw the selection in the multi-layered approach, described above, we use a third layer, between the complete set of fiber samples and the representative fibers. As a result, selected fibers are shown on top of the complete set but may be occluded by the representative fibers, as shown in Figure 5.7.

5.5.3. LINKED DISTANCE SCORE HISTOGRAM

Selecting fibers based on the interval ranges, as described in Section 5.5.2 allows the user to gain an impression of the variance of the samples from the representative fiber, for example, to identify outliers. To provide further insight into the distribution of the generated fiber samples, we compute the distance of each sample from its corresponding representative fiber and show these in a histogram (inset, Figure 5.7). The fiber distribution in the histogram is represented so that the left part of the histogram depicts the fiber samples closer to the representative fibers, while the extreme right part denotes the fibers further away.

We further allow the user to select intervals visually, by brushing in the histogram view, providing an intuitive way to understand the uncertainty distribution. We use the same color scheme used for the 3D representation (Section 5.5.2) to indicate fiber samples and selections in the histogram. Together with the stability of the actual fiber visualization, the continuously updating histogram is an indicator of the stability of the estimated uncertainty. Over time, it is expected that the histogram will have fewer fluctuations, indicating that the addition of samples has less influence on the final uncertainty estimation. To aid the evaluation of the stability of the uncertainty estimation beyond animation, we calculate the earth mover's distance (EMD) [18] between the histograms of consecutive bootstrap iterations. The EMD quantifies the differences in the distribution for the two consecutive histograms. Hence after several iterations, the histogram becomes more stable, consequently the distance between the histograms reduces depicting the stability of the simulation. We show these values in an optional, on-demand line plot, shown in the bottom right corner of Figure 5.7.

5.6. RESULTS

In this section, we evaluate the developed framework and discuss the interactivity of the progressive simulation, uncertainty estimation, and rendering. We used two DW-MRI data sets, one from a healthy subject, one of a patient with a brain tumor, provided by our collaborators. During separate sessions with two clinical collaborators, we extracted several fiber tract bundles (i.e., Inferior Front Occipital Fasciculus (IFOF), Corticospinal Tract (CST), Arcuate Fasciculus (AF), Optic Radiation (OR)) from these datasets, using our tool. The original volume datasets comprise of $112 \times 112 \times 70$ voxels, with a resolution of $2 \times 2 \times 2\text{mm}^3$, a b-value of 1,000, and 56 gradient directions. All computations were performed using an Intel (R) Core i7-4820K CPU at 2.6 GHz. Our framework is implemented in C++, as a plug-in for the open-source medical image processing and visualization framework 3D Slicer [7].

5.6.1. PROGRESSIVE SIMULATION

In clinical applications, generating the specific fiber tract requires constant tuning of the parameters, especially the regions of interest (ROIs). Our framework allowed our clinical partners to generate and manipulate the fiber tracking regions of interest during the progressive generation of fiber samples. The interactions provided in our framework were found to be useful to create the fiber tracts.

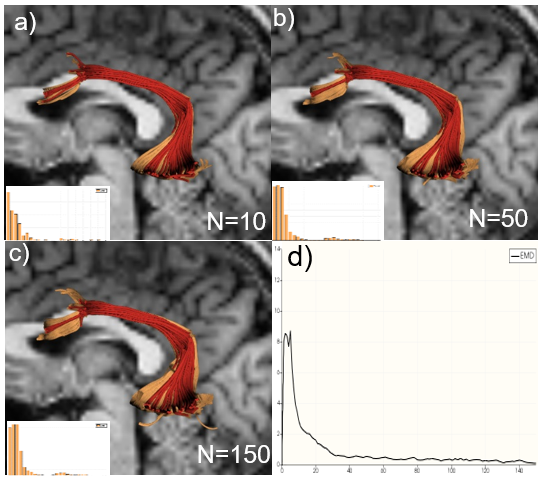

Figure 5.8: Progressive simulation and visualization of the Arcuate Fasciculus. a) to c) show the results of the simulation after N iterations. d) shows the histogram stability plot.

Figure 5.6 illustrates the progressive computation and visualization of a representative fiber and the corresponding variation for a single seed point. The fiber is part of the Arcuate Fasciculus (AF) bundle as was defined by our collaborators. At each bootstrap iteration, a new fiber sample is generated from the seed point, which in turn updates the distance score table, and subsequently the representative fiber. The variation in the representative fiber and inclusion of the new fiber samples can be seen in Figures 5.6b-f, illustrating the result after 5, 10, 100, 350, and 500 iterations, respectively. In Figures 5.6a-d, it can be seen that the 3D representation and the histogram changes significantly between the different snapshots. As the number of similar fiber samples increases within an ensemble, the representative fiber updates accordingly. After an adequate number of bootstrap iterations, the overall structure of the fiber tract, along with its variations, becomes stable, as indicated in Figures 5.6e and f. As can be seen, there are no major changes in the fiber structure and histograms, and the simulation can be considered as converged. The stability of the histogram can also be analyzed with the histogram stability plot as discussed in Section 5.5.3. With increasing number of iterations, the histogram becomes stable and consequently the distance among the consecutive histograms diminishes, as shown in the line plot in Figure 5.6g. However, it should be noted that the stability plot alone is not an indicator of the convergence of the simulation, rather it only depicts how stable histogram is. Convergence of the simulation is always observed in combination with analyzing the 3D shape of the fiber structure and the stability of the histogram.

Figure 5.8 shows the convergence behavior when using a seed region instead of a single seed point in the AF tract. As the simulation proceeds, the inclusion of more fiber samples stabilizes the distribution. Since the bundle is rather compact and is not strongly affected by noise, there are consistent updates in the fiber structure from the beginning of the simulation. The distance distribution and the fiber samples shows no major changes even as early as 50 iterations. The structure of the fiber tract samples seems stable from the early stage of the simulation, and hence, one can estimate that only few bootstrap iterations are required for estimating the uncertainty in this case. Figure 5.8d shows the histogram stability plot which further clarifies the consistency of the histogram, as evident from the plot, the histogram distributions remains homogeneous from the early stage of the simulation.

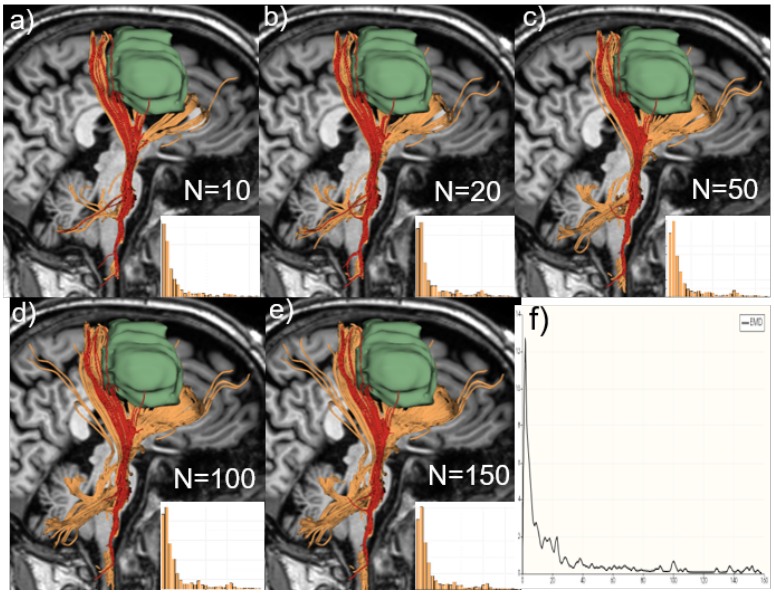

Figure 5.9: Progressive simulation and visualization of the part of corticospinal tract with tumor in the vicinity. Figures a) to e) show the results of the simulation after N iterations. f) shows the histogram stability plot.

Figure 5.9 shows a second example, using region-based seeding to generate the CST tract as defined by our collaborators. Here, a tumor causes displacement of the CST tract. Initially, the distance distribution and the representative fibers update more rapidly because insufficient fiber samples are present. This can be seen from the samples and histogram in Figures 5.9a-c. The histogram stability plot, shown in Figure 5.9f further shows the large distance among the histogram distribution in the early stage of the simulation. As the simulation proceeds, the inclusion of more fiber samples stabilizes the distribution.

The examples shown indicate that convergence, as indicated by our partners, is reached after a different number of iterations. With our progressive framework, the users do not need to define the total number of iterations in advance and wait for the results. They can directly analyze the progressive results according to their stability estimated from the 3D visualization and the histogram.

EXPERT FEEDBACK

We have conducted multiple feedback sessions with our collaborators, including two radiology operators and a surgeon in training. Our collaborators generated the core fiber bundles presented in this paper using our tool and provided feedback, both informally, as well as through a questionnaire. They noted that using our framework improved their understanding of the uncertainty present in the data and the extracted bundles.

The stability of the simulations was identified by analyzing histogram stability and the 3D shape of the bundle. Our collaborators were enticed by the interactive definition

of bundles. However, they also remarked that they would need more experience with such methods and uncertainty in general, to be able to provide reliable evidence of the benefits. We also got feedback from a collaborating neurosurgeon, on the visualization of the uncertainty, discussed in more detail in section 5.6.2.

5.6.2. INTERACTIVE UNCERTAINTY EXPLORATION

Similar to strategies presented by [2], we provide the possibility to specify confidence intervals of fiber samples to be visualized. The interval can be selected based on a percentage of fiber samples closest to their corresponding representatives, similar to quantiles in scalar value distributions. Figure 5.10c shows the $0-50\%$ interval of the fiber samples closest to their representative for the AF tract. The selection is highlighted in blue. Figure 5.10d illustrates the $90-100\%$ interval, showing the 10% fibers that are farthest away from their representative fiber. The interval selection through the percentage of closest fibers has a direct interpretation on the chance to track a fiber within the region.

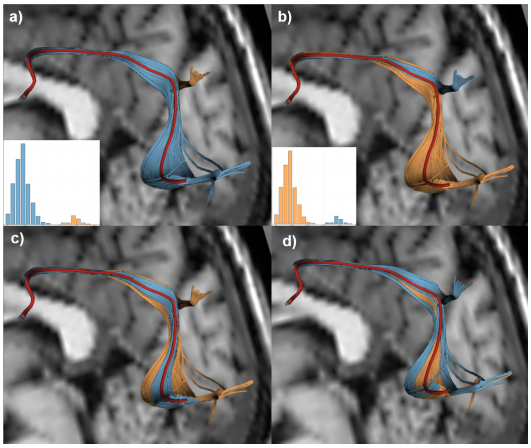

Figure 5.10: Visualization of fiber confidence intervals: a-b) selection of intervals based on the modes present in the distance score histogram c) $0-50\%$ and d $90-100\%$ closest fibers interval selection.

As explained in Section 5.5.3, our framework also allows to select interval based on the histogram distribution of the distances to the representative fiber. Figure 5.10a and 5.10b illustrate the selection using the distance score histogram. By observing the histogram, one can identify the branch present in the fiber ensemble. The selection in Figure 5.10a corresponds to the fiber samples that are closer to the representative while the selection in Figure 5.10b corresponds to the branch which is further away. As illustrated it is possible to identify deviations from a uni-modal distributions. Our representative-fiber calculation assumes that the distribution of fibers originating from a seed point is uni-modal. However this does not always hold and one calculated representative fiber is not adequate. The histogram is likely to show multiple peaks when this is the case (see Figure 5.7). In discussion with our collaborators, this interaction with the histogram helps in understanding the variations present in the bundle and identifying the outliers.

Figure 5.1a was generated together with our collaborators and would be the result of tracing the CST bundle with deterministic fiber tracking used in their common workflow. As illustrated in Figure 5.1, deterministic fiber tracking can miss relevant fiber tracts, and thereby has false-negatives.

Table 5.1: Comparison of the number of voxels used in the bootstrap computations per iteration for the Corticospinal tract (CST), Arcuate Fasciculuss (AF) and Optic Radiation (OR).

	Naive	Progressive		
		CST	AF	OR
μ voxels	1,540,096	324	288	209
σ voxels	-	39	31	30
μ time [ms]	4,650	4.5	4.1	3.9
σ time [ms]	-	0.6	0.55	0.52

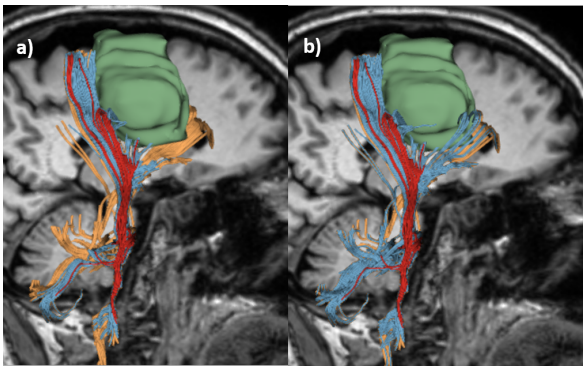

Figure 5.11: Visualization of the fibers with the interval selected from histogram for corticospinal tract (CST) with the tumor in the vicinity.

A fixed safety margin around deterministic fiber tracking results, which is indicated by the blue line in Figure 5.1a, is a common clinical practice used to determine the area of risk. The margin is equally distributed along the fibers however, it is not reliable as can be seen in Figure 5.1b. Our collaborators neurosurgeons indicated that false negative as the ones missed in Figure 5.1a are specially dangerous, as neurosurgeons may inadvertedly damage tracts and induce neurological deficits.

We further utilize histogram for interval selection to analyze uncertainties. Figure 5.11 illustrates the interval selection in the case where the CST bundle is affected by a tumor. Figure 5.11a illustrates the selection of the 40% fibers that are closest to representatives and Figure 5.11b represents the interval of 70%. As can be seen in the Figure 40% fibers are in the back area, however, on increasing the interval to 70%, the branch towards frontal area can be observed. As indicated from our collaborators, the interval selection helps define the risk area for planning tumor resection surgery.

5.6.3. COMPUTATIONAL ANALYSIS

To analyze the computational cost and acceleration, achieved with our progressive approach, we have generated three fiber ensembles, corresponding to different anatomical regions defined with our collaborators. First, we compare the number of voxels necessary to compute each fiber tract sample. As the computation per voxel is identical between methods, we decided to use the number of voxels, instead of the computation time for comparison. It should be noted that the naive approach can easily be parallelized even for a single fiber and member. However, this advantage can be offset by computing multiple fibers in parallel with our approach. As discussed earlier, the naive

bootstrap method computes the ensemble of the complete diffusion tensor field, hence, the number of voxels corresponds to all voxels comprising the volume (approximately 1.5 million). Our local bootstrap strategy only computes bootstrap samples for voxels along the fiber of interest. We provide an overview of the required mean (μ) number of voxels and the standard deviation (σ) per iteration of the same tract in Table 5.1. The mean and standard deviation are computed over 100 bootstrap iterations. In summary, our local bootstrap strategy significantly reduces the number of bootstrap computations required for each iteration. Consequently, the computation time for the required voxels as well as the required memory is significantly lower compared to the naive approach.

In typical applications, users are interested in fiber bundles consisting of multiple fiber tracts. Typically, those fiber tracts share a significant amount of voxels, meaning that as we increase the number of fiber tracts computed for the same seed regions, these shared voxels can be re-used. Figure 5.12 shows the number of voxels that need to be computed for the Corticospinal tract (CST,) and Arcuate Fasciculus (AF), with increasing seeding density. As can be seen in Figures 5.8 and 5.9, the fibers are much less spread in the AF compared to the CST. Consequently, the amount of voxels, needed for computing the bundle flattens out much quicker for the AF than for the CST (Figure 5.12). Nonetheless, in both cases, we can observe a flattening of the curves indicating that performance gains are even bigger for bundles, than for individual fibers.

Our framework consist of two major stages *progressive bootstrap and fiber tracking*, where fibers are generated, and *progressive fiber aggregation* where the derived data, such as the representative fiber are computed. The computation time for the bootstrap and fiber-tracking stage only varies, depending on variations in the data, i.e., tracts taking longer or shorter paths in the current iteration. The computation time for the progressive fiber aggregation stage, however, increases with each iteration, i.e., at iteration n, $n-1$ pairwise distances need to be computed. While this sums up to the same $N^2/2$ distances that need to be computed without the progressive approach, distributing the computations over the iterations reduces the wait time for the visualization significantly. Further, introducing the similarity threshold can drastically cut computation times. We illustrate the correlation between the cut off threshold and computation time in Figure 5.13. We performed the progressive aggregation for 1,000 bootstrap iterations with increasing threshold values. As can be seen, the computation time (green) drastically de-

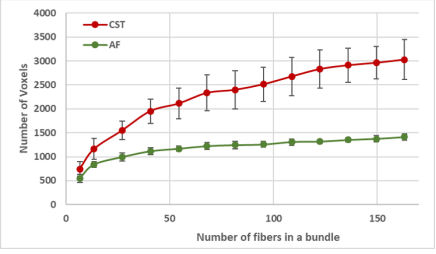

Figure 5.12: Number of voxels required to compute fiber tracts with increasing seeding density.

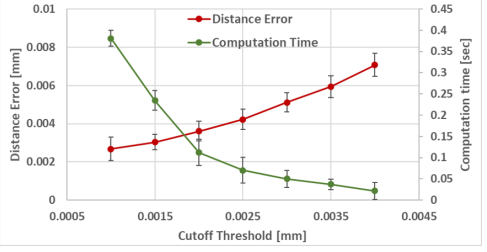

Figure 5.13: Computation time and Error.

creases, even for small threshold values. At the same time, the error (red line, Figure 5.13) compared to the exact computation without a threshold is increasing with larger threshold values. The error is calculated as the mean of the closest point distance between the exact representative fiber, and the representative fiber computed with the given threshold value. Since the fiber ensemble is computed using a stochastic process, we repeated the calculations 100 times, represented by the error bars in Figure 5.13. Given the curves in Figure 5.13, we estimate that a small cut off can provide significant speed up, with no noticeable reduction of accuracy.

5.7. CONCLUSION AND FUTURE WORK

In this chapter, we have presented a progressive visual analytics strategy for uncertainty visualization in DTI fiber tracking, based on stochastic modeling. We have modified the wild-bootstrapping and fiber-tracking pipeline to enable a progressive approach. In particular, we have designed a local wild-bootstrapping approach, integrated into and driven by interactive fiber tracking. Although we developed our progressive pipeline for DTI, the concept is extensible to HARDI and other models, as long as a local simulation method for uncertainty estimation is present such as [4].

Our clinical collaborators stress the relevance of adding uncertainty to their existing current workflow. However the lack of access to tools that show uncertainty makes it difficult to show its real benefit in practice. Our proposed progressive approach is a first step towards reducing the clinical bottleneck making uncertainty visualization more accessible to clinicians. As future direction we want to integrate the progressive uncertainty visualization in their workflow and evaluate whether and how uncertainty influences the decision making process. A progressive pipeline provides the possibility of immediate analysis at the danger of evaluating premature results. In this paper, we rely on the stability shown by the animation of the visualized results to indicate reliability of the results. However, more research is needed to evaluate the implications of the progressive pipeline. Despite positive anecdotal feedback from our clinical partners, the acceptance of our progressive framework by clinical users cannot be assumed, as the users are unaccustomed with uncertainty visualization and it requires some experience to adopt it in a routine workflow. The focus of this work was on the progressive computation rather than the visual representation. More sophisticated visual representations, integrated with the progressive aggregation method are an interesting avenue for future work. Furthermore, we have explored a limited amount of sources of uncertainty. The progressive framework can be extend to accommodate other sources of uncertainty coming from other stages of the pipeline.

REFERENCES

[1] Timothy EJ Behrens et al. “Characterization and propagation of uncertainty in diffusion-weighted MR imaging”. In: *Magnetic Resonance in Medicine: An Official Journal of the International Society for Magnetic Resonance in Medicine* 50.5 (2003), pp. 1077–1088.

[2] Ralph Brecheisen et al. “Illustrative uncertainty visualization of DTI fiber pathways”. In: *The Visual Computer* 29.4 (2013), pp. 297–309.

[3] Weri Chen et al. “Abstractive representation and exploration of hierarchically clustered diffusion tensor fiber tracts”. In: *Computer Graphics Forum*. Vol. 27. 3. Wiley Online Library. 2008, pp. 1071–1078.

[4] Julien Cohen-Adad, Maxime Descoteaux, and Lawrence L Wald. “Quality assessment of high angular resolution diffusion imaging data using bootstrap on Q-ball reconstruction”. In: *Journal of Magnetic Resonance Imaging* 33.5 (2011), pp. 1194–1208.

[5] Isabelle Corouge et al. “Fiber tract-oriented statistics for quantitative diffusion tensor MRI analysis”. In: *International Conference on Medical Image Computing and Computer-Assisted Intervention*. Springer. 2005, pp. 131–139.

[6] Frank Enders et al. *Visualization of white matter tracts with wrapped streamlines*. IEEE, 2005.

[7] Andriy Fedorov et al. “3D Slicer as an image computing platform for the Quantitative Imaging Network”. In: *Magnetic resonance imaging* 30.9 (2012), pp. 1323–1341.

[8] Jean-Daniel Fekete and Romain Primet. “Progressive Analytics: A Computation Paradigm for Exploratory Data Analysis”. In: *arXiv preprint arXiv:1607.05162* (2016).

[9] Weiming Gu, Jeffrey Vetter, and Karsten Schwan. “An annotated bibliography of interactive program steering”. In: *ACM Sigplan Notices* 29.9 (1994), pp. 140–148.

[10] Mark Harrower and Cynthia A Brewer. “ColorBrewer. org: an online tool for selecting colour schemes for maps”. In: *The Cartographic Journal* 40.1 (2003), pp. 27–37.

[11] Christopher R Johnson and Steven G Parker. “A computational steering model applied to problems in medicine”. In: *Supercomputing’94: Proceedings of the 1994 ACM/IEEE Conference on Supercomputing*. IEEE. 1994, pp. 540–549.

[12] Derek K Jones. “Tractography gone wild: probabilistic fibre tracking using the wild bootstrap with diffusion tensor MRI”. In: *IEEE transactions on medical imaging* 27.9 (2008), pp. 1268–1274.

[13] Cheng Guan Koay et al. “Investigation of anomalous estimates of tensor-derived quantities in diffusion tensor imaging”. In: *Magnetic Resonance in Medicine: An Official Journal of the International Society for Magnetic Resonance in Medicine* 55.4 (2006), pp. 930–936.

[14] Dorit Merhof et al. “Isosurface-based generation of hulls encompassing neuronal pathways”. In: *Stereotactic and functional neurosurgery* 87.1 (2009), pp. 50–60.

[15] Mahsa Mirzargar, Ross T Whitaker, and Robert M Kirby. “Curve boxplot: Generalization of boxplot for ensembles of curves”. In: *IEEE transactions on visualization and computer graphics* 20.12 (2014), pp. 2654–2663.

[16] Bart Moberts, Anna Vilanova, and Jarke J Van Wijk. “Evaluation of fiber clustering methods for diffusion tensor imaging”. In: *Proceedings of IEEE Visualization*. IEEE. 2005, pp. 65–72.

[17] T. Mühlbacher et al. “Opening the Black Box: Strategies for Increased User Involvement in Existing Algorithm Implementations”. In: *IEEE Transactions on Visualization and Computer Graphics* 20.12 (2014), pp. 1643–1652.

[18] Yossi Rubner, Carlo Tomasi, and Leonidas J Guibas. “A metric for distributions with applications to image databases”. In: *Sixth International Conference on Computer Vision (IEEE Cat. No. 98CH36271)*. IEEE. 1998, pp. 59–66.

[19] C.D. Stolper, A. Perer, and D. Gotz. “Progressive Visual Analytics: User-Driven Visual Exploration of In-Progress Analytics”. In: *IEEE Transactions on Visualization and Computer Graphics* 20.12 (2014), pp. 1653–1662.

[20] F Weiler et al. “Dealing with Inaccuracies in Multimodal Neurosurgical Planning-A Preliminary Concept”. In: *Proceedings of the 22nd Internal Congress and Exhibition of Computer Assisted Radiology and Surgery (CARS)*. Vol. 2008. 2008.

[21] Ross T Whitaker, Mahsa Mirzargar, and Robert M Kirby. “Contour boxplots: A method for characterizing uncertainty in feature sets from simulation ensembles”. In: *IEEE Transactions on Visualization and Computer Graphics* 19.12 (2013), pp. 2713–2722.

[22] Brandon Whitcher et al. “Using the wild bootstrap to quantify uncertainty in diffusion tensor imaging”. In: *Human brain mapping* 29.3 (2008), pp. 346–362.

6

INTERACTIVE VISUAL EXPLORATION OF REGION-BASED SENSITIVITIES IN FIBER TRACKING

While Chapter 5 focused on addressing uncertainty in the early stages of the DTI pipeline and visualizing it within the progressive visual analytics paradigm, this chapter shifts focus to the user-defined parameters in fiber tracking. One such parameter is the definition of seed-points, which plays an important role in shaping the results of fiber tracking. In this chapter, we explore how sensitivity analysis of seed-points can enhance the definition of regions of interest (ROI) and improve the accuracy of fiber tract generation. We present an interactive approach that leverages seed-point sensitivities to guide users in defining optimal ROIs, with a focus on clinical applications and visualization strategies for effective decision-making. This chapter is based on the paper:

Siddiqui, F., Höllt, T., and Vilanova, A. (2023). Interactive visual exploration of region-based sensitivities in fiber tracking. In Eurographics Workshop on Visual Computing for Biology and Medicine 2023 (pp. 13-22).
https://doi.org/10.2312/vcbm.20231208.

6.1. INTRODUCTION

In clinical fiber tracking applications, Regions of Interest (ROIs) like the seed region, are defined by users manually to extract a specific bundle, i.e., a coherent set of fibers connecting two specific regions in the brain. In most cases, users take guidance from anatomical imaging in combination with a 2D directional encoded color (DEC) map (see Figure 6.1a and 6.1b). A DEC map encodes the main tensor direction by mapping the (x, y, z)-components of the direction to RGB color channels, respectively, weighted by Fractional Anisotopy (FA) [32]. Interactive and automated ROI definition based on the local diffusion properties is well studied [43, 44].

Automatic ROI definition methods often require manual tuning and redefinitions, resulting in a trial and error process, requiring multiple iterations to extract the desired fiber tracts and meet the expectations of the clinician [44]. Relying solely on the DEC maps and the anatomical information is sometimes not enough for ROI definition since it only indicates the local directional and anatomical information. Figure 6.1 shows an example where both the anatomical image (Figure 6.1a) and the DEC map (Figure 6.1b) indicate homeogeneouos values within a potential ROI R. This could indicate that the fiber tracts seeded from this region may form a coherent bundle. However, the resulting fiber tracts generated from the region R are from two different bundles namely Arcuate Fasciculus (AF) bundle and the superior longitudinal fasciculus (SLF) bundle, as shown in Figure 6.1c. The resulting fiber demonstrates that there is a division in the region that is not visible on anatomical images and DEC maps, which are the common visualization techniques in a clinical setting.

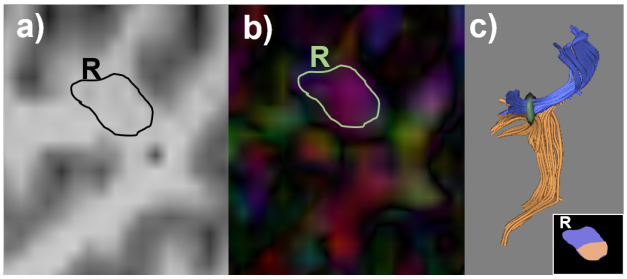

Figure 6.1: Potential ROI R overlaid on a T1 image (a) and DEC map (b). In both images, the values in R are homogeneous. However, the resulting fiber tract from the given seed region R is divided into two different fiber bundles (c, orange, and purple) corresponding to a division in the ROI shown in the inset.

In this paper, we explore the use of seed-point sensitivity as additional guidance for users. Seed-point sensitivity refers to the variation in fiber tract structures due to slight changes in the seed-point location. By quantifying and visualizing seed-point sensitivity, users can identify the boundaries of desired fiber bundles, aiding in the generation of optimal fiber tracking results. In the example, ROI R in Figure 6.1, such a measure would produce large sensitivity values in the region where the bundle diverges and as such, alleviate the adjustment of R. Our main contributions are:

- the identification and analysis of scenarios in which seed-point sensitivity can aid in ROI definition,
- corresponding ROI guidance and course of action per scenario for ROI optimization,
- visualization and interaction techniques to guide the definition of ROIs based on the defined scenarios and course of action.

6.2. CLINICAL WORKFLOW

To understand the fiber tracking workflow in the neurosurgical setting, we conducted exploratory sessions with our collaborators, which include neurosurgeons, radiologists, and researchers who use fiber tracking for planning tumor resection surgeries. Our clinical collaborators expressed a specific interest in reconstructing the core bundles: Arcuate Fasciculus (AF), Inferior Frontal Occipital Fasciculus (IFOF), Corticospinal Tract (CST), Optic Radiation (OR), and the Frontal Aslant Tract (FAT). These bundles are relevant for neural communication and function in visual perception, recognition, language processing, and motor movements.

Our collaborators employ both automatic and manual pipelines for fiber tracking during preoperative planning. In the manual clinical pipeline, the workflow starts with the image acquisition, followed by the preprocessing of the data, which includes correcting for motion artifacts and eddy currents and normalizing the data to a common space. After the data has been preprocessed, diffusion modeling takes place. The manual clinical pipeline relies on diffusion tensor imaging (DTI) [26]. However, in our work, other modeling techniques such as HARDI [42] can also be integrated. After diffusion tensor modeling, ROIs are defined using anatomical information and DEC maps. The ROIs include seed regions and AND regions that are used to filter irrelevant fibers [23, 25, 31, 37]. Using AND ROIs in fiber tracking improves the specificity and reliability of resulting fiber bundles, avoiding spurious fibers. Within the clinical workflow, users manually define ROIs to extract particular bundles. Typically, anatomical cues like T1 images and DEC maps offer partial guidance yet prove insufficient for accurate ROI definition. The task requires multiple iterations to adequately define ROIs, demanding expertise and anatomical insight for optimal accuracy. To circumvent this issue, a guidance strategy is needed to help users in defining desired ROIs. Our collaborators are also testing an automatic pipeline for use in the clinical workflow. Here, ROIs are defined automatically using Spatially Localized Atlas Network Tiles (SLANT) [20], which use deep learning to compute subject-optimized whole brain segmentations. Fiber tracking is performed using Constrained-Spherical Deconvolution (CSD) method [41]. Although ROIs are defined automatically, manual user input and tuning are needed when the generated results are not adequate.

Our work aims to provide interactive visual guidance in determining ROIs based on seed point sensitivity. Our framework can be used with any diffusion modeling and fiber tracking method that provides fiber tracts through ROI definitions, as we base our sensitivity computation solely on the resulting fiber tracts, i.e., the geometrical features of the fiber tracking results. We demonstrate the feasibility of our framework by utilizing both the manual and automatic workflows of our collaborating partners.

6.3. Related Work

In this section, we provide a comprehensive review of the literature that is relevant to our work, specifically focusing on studies that investigate fiber tracking parameters and their sensitivities, as well as the definition of ROIs. In addition, we also examine related work on the visual encoding of multiple scalar fields along with the discussion on coherence measures. Our primary emphasis is on papers that explore sensitivities and ROIs.

The fiber-tracking pipeline comprises several input parameters that control the tracking process. The most critical user-defined parameters are Fractional Anisotropy (FA) thresholds and ROIs. Taoka et al. [40] evaluated the influence of FA thresholds in measuring diffusion tensor parameters for tract-based analysis. Gutierrez et al. [15] presented a framework to optimize FA thresholds of fiber tracking algorithms using multi-objective optimization techniques. Brecheisen et al. [4] evaluated the sensitivity of FA thresholds in fiber-tracking algorithms and provided an interactive visualization for parameter exploration.

Schlaier et al. [36] studied the influence of seed regions to delineate cerebellar-thalamic fibers in deep-brain stimulation and analyze how seed regions affect the results in both deterministic and probabilistic fiber tracking. Huang et al. [18] assessed the effects of noise, ROI size, and location on DTI-based fiber reconstruction results for one-ROI (i.e., seed region only) and two-ROI approaches (i.e., seed region plus AND regions). They analyzed the differences in the resulting tracts by dilating the ROI size and perturbing the location. Even though the study was principally focused on comparing one- and two-ROI approaches, they concluded that the ROI placement could be a major source of poor reproducibility in fiber tracking. Several approaches have been proposed in the literature to automatically define ROIs [11, 19]. Weiler et al. [44] employed local diffusion parameters, such as fractional anisotropy and radial diffusivity, to generate automated ROIs for fiber tracking. Despite the existence of automatic methods, manual user input in ROI definition is still needed in complex cases. Schonberg et al. [38] propose to use functional MRI (fMRI) data to define ROIs for adequate fiber tracking results, especially when ROIs have to be placed within or in the vicinity of a lesion. The presence of lesions deforms the fiber structures, affecting the DEC map and T1 image and thus impeding ROI definition. In complex cases, fMRI data is also affected by edema or glioma. Voltoline et al. [43] proposed to combine shape and FA information and show them as glyphs to guide ROI definition. To the best of our knowledge, there has been no research on the inclusion of seed-point and ROI sensitivities.

The use of tensor lines to visualize tensor fields is closely related to vector field visualization using integral curves, modeling the trajectories of particles through the field. Visualizing the coherence of motion among neighboring particles has been studied in this context [7, 13, 27, 35]. These approaches locally express the change of the particle trajectory with a variation of the initial position. Hlawitschka et al. [17] presented an approach based on similar concepts applied to tensor lines. They introduced a coherence measure defined for fiber tracts and provided an effective visualization to represent the fiber coherence combined with the existing visualization. Moberts et al. [30] and Qazi et al. [33] discuss measures for the quantification of coherence of neighboring fibers in diffusion tensor data. In our work, we use existing coherence measures based on the

global geometrical shape to compute the sensitivity of seed point placement and provide guidance to the users to define an optimal ROI. To the best of our knowledge, no related work proposes using sensitivity analysis for ROI definition and guidance in fiber tracking workflow.

Numerous contributions have been presented in the literature concerning the visual encoding of multiple scalar fields, encompassing measures like coherence, hemodynamics, uncertainty, etc. Meuschke et al. [28] introduced a method for concurrently displaying two scalar fields for the visual analysis of aneurysm data, aiming to enhance insights into complex anatomical structures. The first attribute is color-coded, while the second utilizes an image-based hatching scheme. Building on this foundation, Meuschke et al. [29] further proposed a checkerboard visualization that facilitates the simultaneous exploration of diverse attributes. Hlawitschka et al. [17] adopt a continuous scalar map with distinct color scales to represent point-wise coherence measures. In our work, we embrace a similar concept, utilizing an interactive discrete color map for scalar field visualization to mitigate visual clutter and effectively portray sensitivity alongside anatomical information.

6.4. SENSITIVITY ANALYSIS

Based on the sensitivity definition [6], we present the seed-point sensitivity as the relation of a slight change, $\delta\mathbf{s}$, in the seed-point position, $\mathbf{s}$, and the amount of change of the resulting fiber tract, $f(\mathbf{s})$, i.e., amount of change of seed point, $||\delta\mathbf{s}||$ versus distance between resulting fiber tracts $d(f(\mathbf{s}+\delta\mathbf{s}), f(\mathbf{s}))$.

We calculate the seed point sensitivity in a predefined grid as a scalar field. To do so, we first assign a sensitivity value S_i to each seed-point position $\mathbf{s}_i$. S_i is defined as the mean of the distances of its corresponding fiber F_i to all other fiber samples within a radius $||\delta\mathbf{s}||$. The sensitivity S_c for each grid cell c in the field is then calculated by averaging the sensitivity values S_i of each seed point within the cell. The resolution of the grid can also be adjusted to achieve the desired precision. Seed points are distributed randomly within the cell based on the predetermined number of fibers per grid cell. However, when pre-computed fibers are utilized, the quantity of fibers per cell depends on the defined fiber density parameter.

There are various options to define the distance $d(f(\mathbf{s}+\delta\mathbf{s}), f(\mathbf{s}))$, depending on the goal. Here, we focus on definitions that consider the geometrical properties of the fiber tracts since the evaluation of the fiber bundle relies primarily on the geometry of the tracts. Other sensitivity parameters, e.g., diffusion properties [17], could also be incorporated. There has been a considerable amount of research on similarity measures between fiber tracts and, more generally, integral lines or curves in vector field [9, 14, 24]. The first category measures the Euclidean distance between pairs of points on two curves, such as the closest point measure, the Hausdorff distance [34], or the Fréchet distance [1]. A second category is the mean Euclidean distance along the run lengths of the curves, such as the mean distance of closest distances [8] or the mean threshold closest distances [45]. There are also distances computed based on Euclidean space embedding of the curves, such as the Gaussian kernel distance [5]. Each of these measures has its own strengths and limitations in terms of sensitivity and invariance. In our work, we focus on the coherent geometrical features of fiber tracts as it is considered an essential

criterion that characterizes bundles. A general assumption is that the fiber tracts belonging to the same bundle have smoothly changing geometrical properties. We explore distance-based metrics, as discussed by Moberts et al. [30] and Corouge et al. [10]. We compute the distance measure d between the fiber tracts F_i and F_j using the mean of the closest point distance, which is proven as a relevant distance measure for automatic clustering for bundle identification [10, 30]. The distance is defined as:

$$d_m(F_i, F_j) = \underset{\mathbf{p}_i \in F_i}{\text{mean}} \min_{\mathbf{p}_j \in F_j} ||\mathbf{p}_i - \mathbf{p}_j|| \tag{6.1}$$

where the minimum distance for each point $\mathbf{p}_i$ of F_i to the points $\mathbf{p}_j$ of F_j is computed, and then the mean of all closest distances of $\mathbf{p}_i$ to F_j is used. Notice that d_m is not symmetric; therefore, the distance between the two fiber tracts d is then computed by $\min(d_m(F_i, F_j), d_m(F_j, F_i))$. Using the minimum allows us to account for different fiber lengths. Other distance measures to calculate the similarity between two curves can be integrated into the pipeline. The choice depends on the specific case to be explored and the fiber tracking algorithm used.

6.5. Scenario Analysis

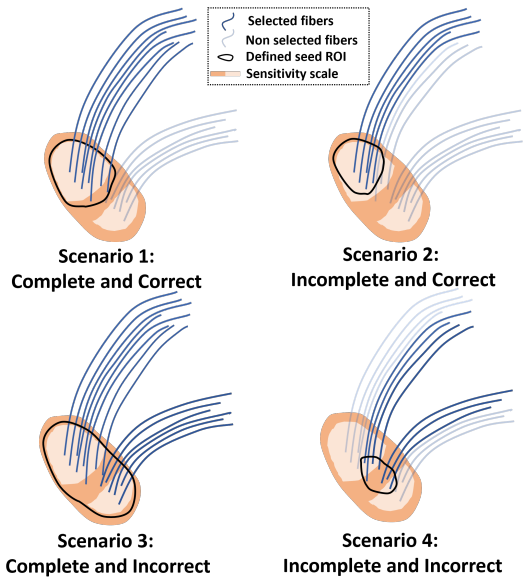

Figure 6.2: Illustrations of the possible scenarios for ROI definition.

To support ROI definition in a structured way, we analyze different scenarios in relation to the use of computed sensitivities for ROI definition. As discussed in Section 6.4, fiber tracts belonging to the same bundle generally have similar or smoothly changing geometrical features. Our assumption is that sensitivity can indicate potential boundaries of bundles that indicate relatively large sensitivity. In the following, we follow previous works [21, 22, 30] and use the terms **complete** and **correct** to evaluate the fiber tracts, resulting from a defined ROI. Here, correctness means that all produced fibers belong to the correct bundle, while completeness means that all fibers belonging to a specific bundle are produced. Given the absence of ground truth in fiber tracking data and our goal being to support the interactive definition of ROIs, correctness, and completeness rely on the specific user requirements and may differ from user to user. Hence, we provide the guidance strategy based on the defined assumptions of similarity of bundles but ultimately leave it to the user's discretion to decide.

Figure 6.2 illustrates four basic scenarios concerning sensitivity based only on the seeding ROI. To explain the possible scenarios, we give an example of a region where two different bundles are diverging and close to each other. We are interested in generating one fiber bundle. The area where the bundles meet can also be identified and investigated with the sensitivity map. For simplicity, we only show two sensitivity levels: dark for high sensitivity and light for low sensitivity. The black outline represents the seed ROI, and the blue curves depict fiber tracts. Solid curves show selected tracts, while transparent ones display filtered fibers based on defined ROIs.

Scenario 1 in Figure 6.2 shows the ideal case where all fibers of the desired bundle are produced, i.e., **complete and correct**. This situation occurs when the ROI extends to the boundary between a low and high-sensitive area without including parts of the high-sensitivity area. **Scenario 2** shows the case where the seed ROI does not produce the whole bundle, i.e., the produced fibers are **correct** but **incomplete**. The defined region needs to be *extended* to cover the complete bundle. In **Scenario 3**, the defined seed ROI has two low sensitivity areas divided by a high sensitivity area depicting that the resulting fibers are **complete**, but due to coverage of an incorrect region, some of the fibers are **incorrect**. The ROI needs to be *shrunk* to only one of the low sensitivity areas. **Scenario 4** shows the combination of Scenarios 2 and 3, where the seed ROI contains low and high sensitivity areas; hence, the resulting set of fibers is **incomplete and incorrect**.

As discussed in Section 6.2, users employ AND ROIs, in addition to the seed region in most clinical cases, to extract specific fiber bundles [2]. We extend the previously discussed scenarios by adding an AND region. We do not consider Scenario 4 as it is a local combination of other scenarios. The scenarios summarized in Figure 6.3 specify the characteristics of the defined ROIs and the corresponding fiber bundle selection. As previously discussed, we distinguish the ROIs in each scenario based on the completeness and correctness of the selected fiber bundle. In Scenario 1.1, both the Seed and AND ROIs generate complete and correct fiber tracts. The combination of these defined ROIs results in a complete and correct fiber bundle. All scenarios with the addition of an AND ROI (represented with the green area) are illustrated in Figure 6.4. The glyph on the top left shows the scenario according to Figure 6.3.

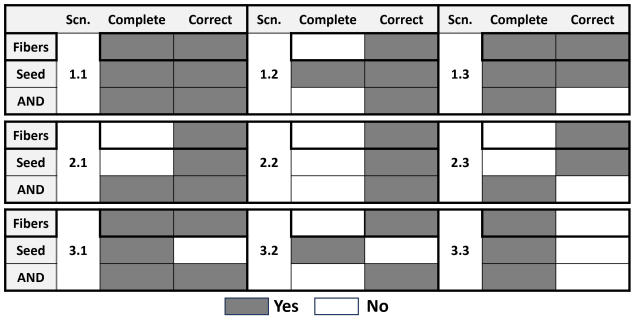

Figure 6.3: Summary of the characteristics of the Seed and AND ROIs and their combined effect for each scenario.

In Scenarios 1.x, the seed ROI is defined as complete and correct, as discussed earlier. Therefore, only a too-small AND ROI impact the result, thus producing an incomplete result (Scenario 1.2). Here, the AND region needs to be extended or removed.

In Scenarios 2.x, the seed ROI misses similar fibers which belong to the desired bun-

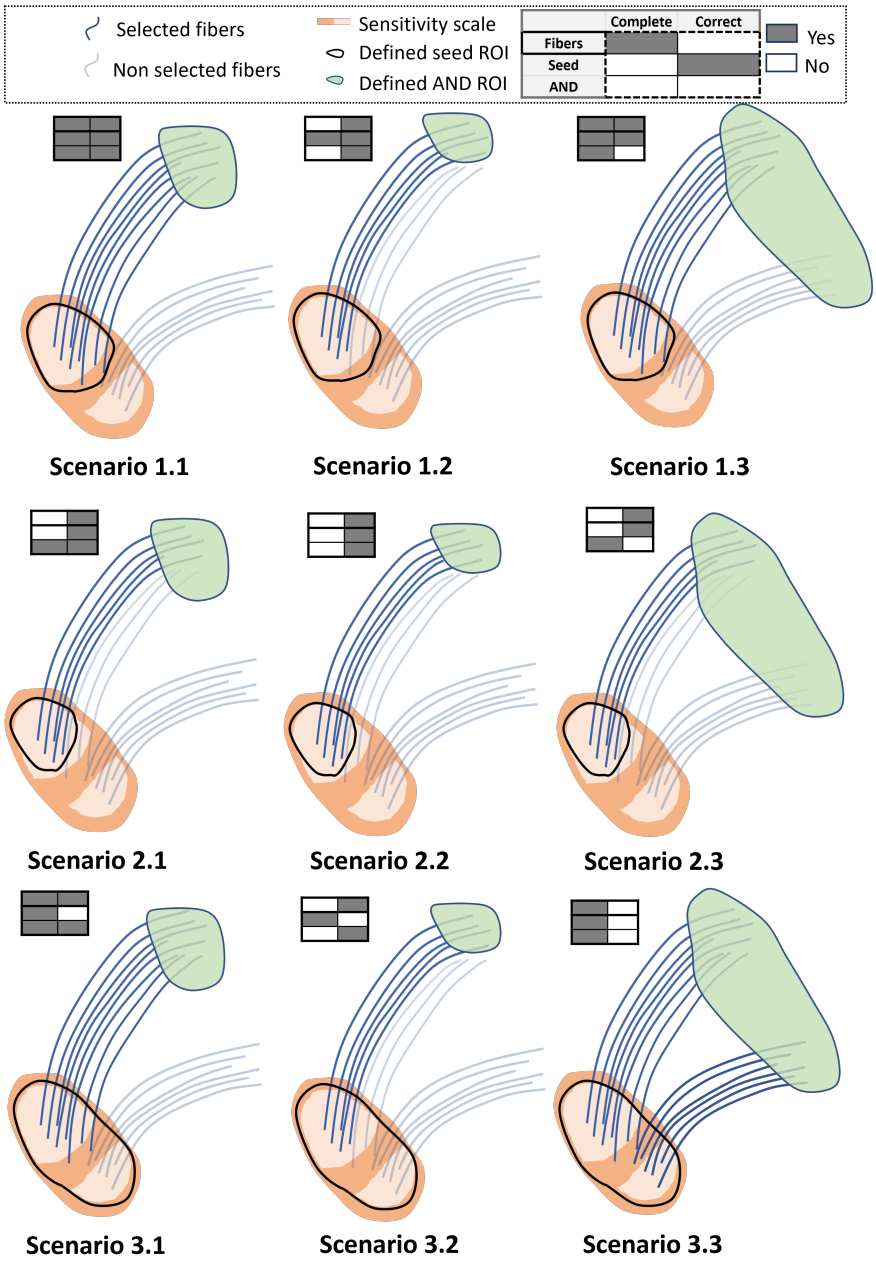

Figure 6.4: Illustrations of the possible scenarios for the definition of the seed and the AND ROI. The glyphs at the top left for each scenario refer to the scenarios illustrated in Figure 6.3.

dle. Therefore all scenarios are incomplete. This cannot be addressed by adjusting the AND ROIs. Thus, the user will want to extend the seed ROI to be complete and correct. The result will be the corresponding Scenarios 1.x.

In Scenarios 3.x, the seed ROI covers fiber tracts from different bundles generating complete but incorrect results. In Scenario 3.1, the AND ROI makes the result complete and correct being the only scenario in 3.x that generates such an outcome. In Scenario 3.2, the AND ROI is incomplete. In this scenario, a user can shrink the seed ROI to get Scenario 1.2 or extend the AND ROI to get Scenario 3.1. Similarly, in Scenario 3.3, both ROIs generate complete but incorrect results. The user can shrink one of the ROIs to get either Scenario 1.3 or 3.1. A summary of the corresponding courses of action to reach the complete and correct results (i.e., Scenarios 1.1, 1.3, and 3.1) is illustrated in Figure 6.5.

In this section, we discuss our proposed visualization design to facilitate the interpretation of sensitivities based on the scenarios and corresponding actions to aid the ROI definition described in Section 6.5. We used anonymized DW-MRI data sets of two different patients provided by our collaborators. The volume data sets comprise of $128 \times 128 \times 60$ voxels, with a resolution of $1.75 \times 1.75 \times 2\text{mm}^3$. The scanner parameters are b-value= 1,000 and gradient-directions= 32.

6.5.1. SENSITIVITY MAPS

Our aim is to provide sensitivity information, which we derive as a scalar field (Section 6.4), alongside the DEC map and anatomical information commonly used in clinical settings. This combination serves to provide guidance for ROI definition. Understanding the seed-point sensitivity within and near the ROI is the basis for identifying the course of action (Section 6.5).

6.6. VISUALIZATION DESIGN

A straightforward approach to visualize the calculated sensitivities is to use quantitative color maps. The maps can be overlaid on top of the anatomical slices or the DEC map. However, the overlaying of the color map occludes structures presented in the DEC map and the anatomical slice. To circumvent this problem, we propose to use a discrete color map with a limited number of bins (e.g., defined using ColorBrewer [16] for sequential data). Based on the proposed interactions and guidance strategy in the previous section, the focus is on identifying and visualizing the highly sensitive regions. Anatomical information, e.g., T1 images, use luminance

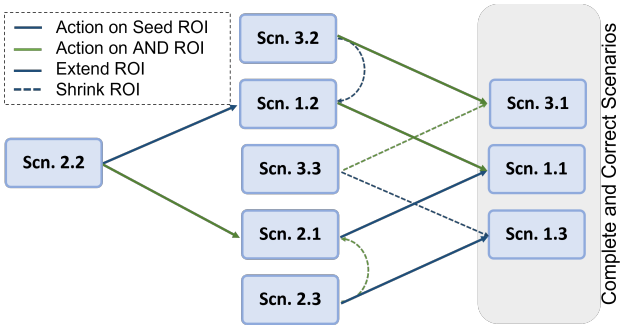

Figure 6.5: Action sequences to reach the complete and correct scenarios.

values to represent the data, while DEC maps use hue channels to encode the tensor directional information. To distinguish our sensitivity map when combined with the anatomical information and the DEC map, we chose a color map that is distinguishable and minimally interferes with the hue of the DEC map. Moreover, we enable users to interactively set and adjust the number of bins to be visualized such that they are more clearly recognizable. Commonly, a relatively low number of bins will be used, making the boundaries of the bundles more obvious. The user can adjust the transparency of each bin, which helps combine different information from the other scalar fields. Figure 6.6 illustrates the color overlay using the case shown in Figure 6.1. Figure 6.6a, Figure 6.6b, and Figure 6.6c show the sensitivity map for two different bins, 7 and 5, overlaid on T1 and the DEC map with adjusted transparencies. The sensitivity map is generated with 8x resolution and a neighborhood window of 5x5x5 voxels. We use the Colorbrewer *OrRd* color map, with the higher bins made more opaque while the lower bins are semi-transparent. In this way, only the regions with high sensitivities are highlighted. The color maps are shown at the bottom left insets in Figure 6.6 with a black border representing non-transparent bins.

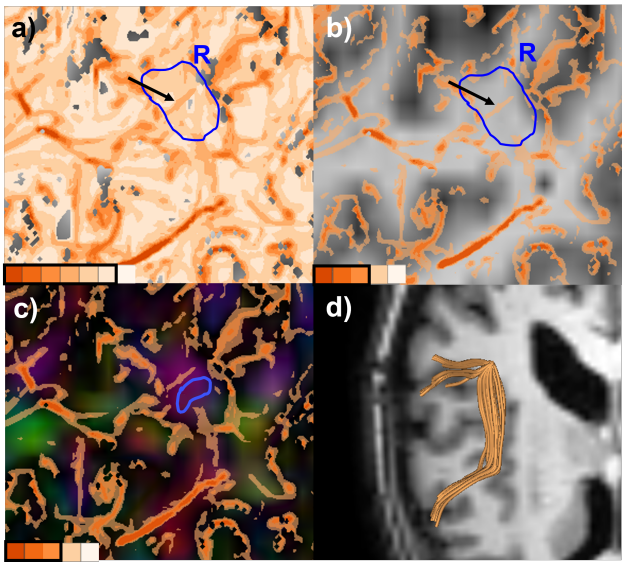

Figure 6.6: The sensitivity map is represented as a discrete color map with a) 7, b, c) 5 bins. The number of bins and transparency are adjusted to reduce cluttering. Seed ROI for different cases is represented with the blue curves, and the fiber tracts are rendered as shaded tubes shown on the 3D view in d). The black arrow highlights the high sensitivity area within the region *R*. The color scale is shown at the bottom left.

As can be seen in Figure 6.6a, a higher number of bins provides more detailed sensitivity distribution but makes the visualization overly complex and cluttered. The number of bins and transparency both are adjusted, as shown in Figure 6.6b and Figure 6.6c, making it easier to identify different sensitivity levels with less cluttering on the anatomical information. The same region *R* introduced in Figure 6.1 is selected as a seed region, which shows a uniform coloring in the DEC map and anatomical slice. Our sensitivity map shows a high-sensitivity region that suggests a boundary cutting the region in two, as shown in Figure 6.6. The black arrow points to the high sensitivity area within the region *R*, depicting that the ROI contains seeds for two different bundles (Scenario 3) as shown in Figure 6.1c. As expected, the generated fiber

tracts are diverging since the ROI encompasses two individual homogeneous sensitivity regions separated by high sensitive boundaries. The sensitivity map makes it easy for the user to identify the boundary between the two bundles and thus helps in optimizing the ROI. Following the guidance strategies as explained in Section 6.5, the ROI needs to be shrunk to extract a coherent set of fibers, as shown in Figures 6.6c and 6.6d.

It is important to note that the computation of the sensitivity as a scalar field can be computationally expensive, with the computation time dependent on both the neighborhood size and the sampling rate within each fiber. We use the same sampling as the integration step of each fiber. The overall computation time for the sensitivity calculation for each cell is around 0.025 seconds for the neighborhood size of $5 \times 5 \times 5$ voxels. To further accelerate the interactions, we enable progressive computation of the sensitivity map in the background, allowing users to continue exploring sensitivities and defining regions of interest (ROIs) without any delay. The computations start from a user-selected ROI progress throughout the plane until the desired area has been computed. The framework also supports the utilization of precomputed fiber tracts and sensitivity maps for ROI definition.

6.6.1. AND ROI PROJECTION

As discussed in Section 6.2, AND ROIs are used to filter the fiber tracts. The most relevant information for the user defining the seed ROIs is whether the region being analyzed is connected to the defined AND ROI. We provide this information by a projection of the AND ROI in the seed ROI area. The projection is calculated by marking the voxel if at least one fiber traced from the cell intersects the defined AND ROI. It is worth mentioning that the projections only rely on the slice being analyzed for seeding; hence, there can be areas of the AND ROI that are not projected. The projection is basically a binary mask that we use in combination with the seed ROI sensitivity. The computed projection is represented as a green semi-transparent area overlaid on the top of the sensitivity map and the anatomical slice, representing the complete area where the fiber tracts are connected to the defined AND ROI. We have used a green overlay on the top of *OrRd* color scale of the sensitivity map, combined with an anatomical slice according to the diverging color suggestion from Colorbrewer. Since the DEC map uses hue as a channel to encode the directional information and uses the full range of color tones,

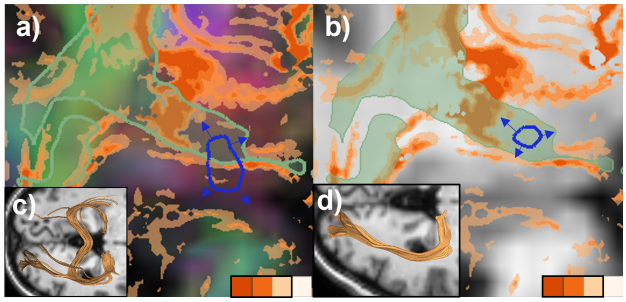

Figure 6.7: ROI projection is represented as a green semi-transparent overlay on the top of a) direction-weighted FA map b) T1 slice with overlaid sensitivity map. The defined seed ROI is represented with a blue curve. The corresponding fiber tracts are shown in c) and d), representing the 3D orthogonal views. Guiding glyphs are shown at the boundaries of the defined ROI.

there is interference. We outlined the binary map to make the projections more distinguishable and recognizable. We provide interactive means to define and optimize the seed and AND ROIs by simply brushing on the corresponding slices. Derived data, such as the AND region projection, are linked and updated interactively.

Figure 6.7 illustrates an example of the generation of OR bundle that connects the lateral geniculate nucleus (LGN) to the primary visual cortex and is responsible for transmitting visual information from the retina of the eye to the visual cortex. In most clinical cases, the AND ROIs are also needed to optimize the resulting fiber tracts. Figure 6.7a shows the initial seed ROI along with the AND ROI projection. The curved course, the sharp turn of the OR, and their proximity to other white matter tracts, including the uncinate fasciculus, the Inferior Fronto-Occipital Fasciculus (IFOF), and the inferior occipito-temporal fasciculus, make its ROI definition quite challenging. The defined seed ROI is represented with a blue curve, and the corresponding generated fiber tracts are shown in Figure 6.7c-d. As can be seen in Figure 6.7a, the defined seed ROI contains a high sensitivity region, corresponding to Scenario 4. The AND ROI in OR is usually fixed as the bundle terminates in the primary visual cortex. Given the projection information and guidance strategy from Scenario 3.3, the user can modify the seed ROI to get the adequate bundle, as shown in Figure 6.7d. The ROI can be further adjusted per suggestions to achieve the desired bundle.

6.6.2. GUIDING GLYPH

In addition to visualization of the sensitivity based on color maps, we provide further guidance based on Scenario 2 (see Section 6.5), which indicates that the sensitivity just outside the defined ROI is homogeneous. The ROI can be extended, suggesting coherent fiber tracts in the vicinity. We use glyph-based visual cues to convey the sensitivity information outside of the currently defined ROI and guide the user on where to extend the ROIs to encompass the coherent fibers. We use simple arrow-based glyphs placed orthogonal to the boundary of the defined ROI. The direction of the arrow indicates the potential direction of extension based on the sensitivity value at the given point, as shown in Figure 6.7. The length of the arrow indicates the inverse of the sensitivity at the given position, which means that if the sensitivity value is low, the arrow will be longer and vice-versa. The arrows are only visible when the sensitivity value at the given position is lower than a certain threshold and when there is no need to extend the ROI. This visual cue guides the user to extend the defined ROI until the sensitivity at the boundaries is high, as explained in seed ROI scenarios 2 and 4 in Section 6.5. As shown in Figure 6.7b, the defined seed ROI covers the incomplete OR bundle corresponding to Scenario 2 and is guided to extend the ROIs.

6.7. RESULTS

In this section, we present use cases of our visualization and initial feedback from our clinical partners with whom we developed the system. We have conducted feedback sessions with two of our collaborators during the course of this work. We explore the definition of ROIs for two fiber tract bundles using two different pipelines and fiber tracking techniques. We analyzed the Arcuate Fasciculus (AF) bundle generated with the man-

ual pipeline using DTI and the Frontal Aslant Tract (FAT) generated with the automatic pipeline using CSD. All computations were performed using an Intel (R) Core i9-9900K CPU (3.6 GHz). Our framework is implemented in C++ and Python as a plug-in for the open-source medical image processing and visualization framework 3D Slicer [12]. The parameters for the fiber tracking are suggested by our collaborators, which include the stopping FA threshold= 0.2, integration step length=0.5mm, and stopping curvature= 0.7.

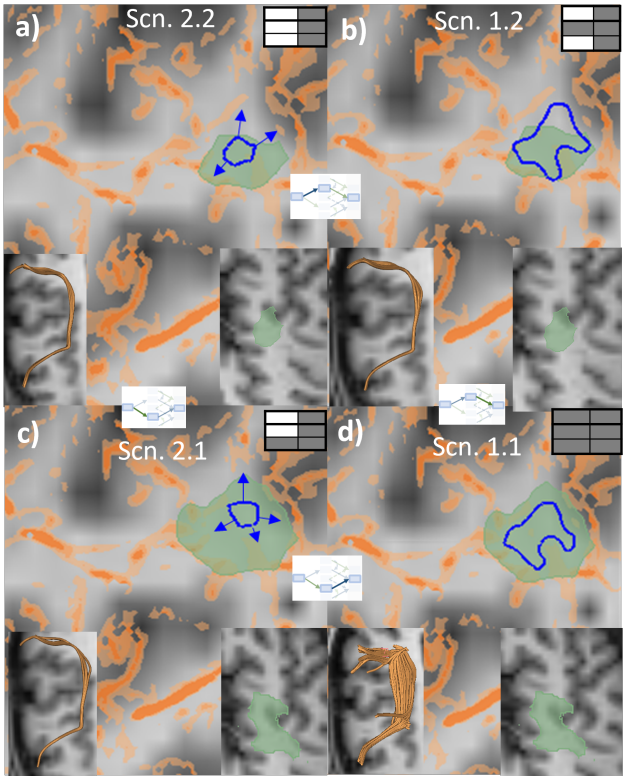

Figure 6.8: ROI definition for Arcuate Fasciculus (AF) bundle. The definition starts with incomplete ROIs and is guided till the complete and correct bundle is generated based on the provided guidance. The glyphs refer to the action sequence shown in Figure 6.5.

In Section 6.5.1, we explored the computed sensitivity map to adequately define seed ROI for Arcuate Fasciculus (AF) bundle. We start our analysis by defining the ROIs based on anatomical knowledge and utilizing the sensitivity map by interactively selecting the region and visualizing the corresponding fibers, as shown in Figure 6.6. It is to be noted that the region manipulation and visualization are interactive and are done in real time. As discussed, AND regions are also incorporated by users to filter out undesired fiber tracts during fiber bundle definition. To aid users in this process, our framework introduces a projection visualization of the AND region, which enables them to comprehend the connectivity of fiber tracts. Figure 6.8 depicts a use case where the user defines the ROIs based on the provided sensitivity visualization and guidance. The definition starts with an initial placement of ROIs, as discussed in Section 6.5.1. The initial AND ROI, shown at the bottom right, is defined by our collaborators based on anatomical knowledge. The projection of the AND region is shown as a green transparent surface on the top of the sensitivity map, along with the defined seed ROI and the anatomical information.

It can be observed that the AND and the seed ROIs do not cover the whole region

where the sensitivity is low, indicating that the case is potentially incomplete, corresponding to Scenario 2.2, as shown in Figure 6.8a. There is a homogeneous low sensitivity region outside of the boundaries. As fiber tracts within a low sensitivity region are assumed to have belonged to the same bundle, some desired tracts are missed in this case. The suggested actions is either to extend the seed ROI to achieve Scenario 1.2 (Figure 6.8b) and modify the AND region to reach Scenario 1.1 (Figure 6.8d). The other option is to extend the AND region first, as shown in Figure 6.8c, and then extend the seed ROI based on visual cues to achieve the final correct state, as shown in Figure 6.8d. The inset images between the figures represent the course of action to go from one scenario to another, as explained in Section 6.5.

In our second case, we employed our developed framework to refine the ROIs of the automated pipeline used by our collaborators. As detailed in Section 6.2, the automated pipeline employs SLANT for automatic ROI definition and subsequently utilizes the CSD method for fiber tracking.

Nevertheless, in certain scenarios, manual adjustment of the automatically generated ROI becomes necessary if the resulting fiber tracts are not adequate, especially in the presence of a tumor. The automatic pipeline is not interactive and requires repeated rerunning after each adjustment of the ROI. Here, we present a case on tuning ROIs for the Frontal Aslant Tract (FAT) bundle. Figure 6.9 shows the initial ROI represented with a blue curve overlaid on the DEC map and anatomical slice, which shows the homogeneous distribution. The resulting fiber tracts are displayed in the inset figure with coronal and axial views. It is observed by our collaborators that the resulting fiber tracts also encompasses the fibers from the neighboring bundle. We employed our visualization strategy to tune the ROIs aiming to achieve a complete and correct bundle. The sensitivity map is generated using 8x resolution and $5 \times 5 \times 5$ of neighborhood window. Figure 6.10 shows the computed sensitivity map overlaid on an anatomical T1 slice, while the resulting fiber tracts are displayed at the bottom section with coronal and axial views. As shown in Figure 6.10a, there are regions of high sensitivity within the initial seed ROI, representing the boundaries among distinct bundles. This information is not visible in the DEC map nor in the anatomical slice, as shown in Figure 6.9. The projection of AND ROI are also represented with a semi-transparent green overlay. It was noticed that the high sensitivity regions shown in the sensitivity map corresponded to fiber tract branches located in the anterior and posterior sides of FAT, which were not part of the desired bundle. This state corresponds to Scenario 3.3, as discussed in Section 6.5. To achieve the complete and correct Scenario 1.3, the suggested course of action involves shrinking the seed ROI to

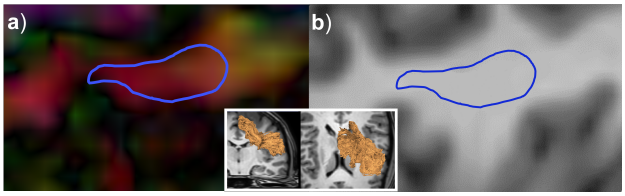

Figure 6.9: ROI used by the automatic pipeline, shown with the blue curve, overlaid on the a) DEC map and b) Anatomical slice. The region shows the uniform distribution, Inset: Coronal and Axial views of the resulting fiber tracts.

the low homogeneous sensitivity region while considering the sensitivity map and ROI projection. The resulting ROI and the fiber tracts are shown in Figure 6.10b. The resulting fiber tracts are validated by our collaborators. With the utilization of the sensitivity map, the user achieved the desired fiber tracts in just one iteration, which would otherwise take four iterations of ROIs adjustments and manipulations in the automatic pipeline.

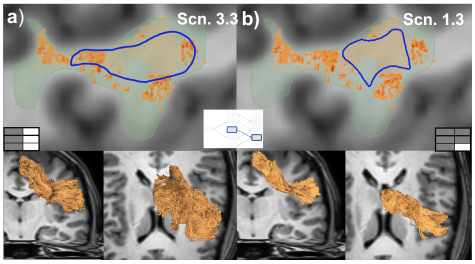

Figure 6.10: ROI definition for Frontal Aslant Tract (FAT) bundle using automatic pipeline. The definition starts with incorrect ROIs and is guided till the complete and correct bundle is generated based on the provided guidance. The inset refers to the action sequence shown in Figure 6.5.

We had a general feedback session with our collaborators regarding the proposed visualization and guidance strategies. They agreed that our proposed visualization strategy could improve their understanding of the sensitivities in the ROIs and help in defining the accurate ROI for the bundle by using the provided visual guidance. Our collaborators were enticed by the interactive definition of the ROIs and especially by the projection visualization of the AND region. However, it was remarked that usability needs to be further studied, which we plan to do in future work.

6.8. CONCLUSION AND FUTURE WORK

There are several parameters in the fiber tracking pipeline that considerably affect the results. In this chapter, we have presented an approach to use seed-point sensitivity to guide ROI definition in the fiber tracking pipeline. We have analyzed the use of sensitivity for ROI definition and presented various scenarios that users experience in the ROI definition process. Based on the provided scenarios, corresponding guidance has been addressed. We have developed an interactive visualization approach as a proof of concept that allows users to investigate the region-based sensitivities and enables sensitivity-aware ROI definition by utilizing the computed seed-point sensitivity feature and projection map. Being able to visualize the sensitivity based on seed-point placement provides additional information to choose the optimal ROI. We also integrated our visualization framework with the automatic pipeline used by our collaborators in their workflow. We explored the feasibility of using a sensitivity map to refine the automatically generated ROIs in a case where manual user input is required. The computed map provided guidance to the user in tuning the ROIs based on the sensitivity information and potentially saving various iterations for ROI adjustments.

While the utilization of color bins and transparency for the overlaid sensitivity map can help reduce clutter to some extent, the sensitivity map still overcrowds essential anatomical information, potentially impeding the user's ability to make accurate judgments. The enhancement of effectively integrating sensitivity information with anatom-

ical data could be contemplated as a prospect for future research. For this study, we limit our work to isotropic perturbation in the seed point. However, anisotropic variations in the seed point could also be explored. The selected distance measure used in sensitivity computation is capable of identifying bundle boundaries through proper bin selection. Nonetheless, there is room for exploring alternative measures to enhance the accuracy of bundle boundary detection even further.

We consider future work to develop a user study to evaluate our designed techniques and the effect of these sensitivities in the definition of ROIs. It would also be interesting to embed our work with other uncertainty visualizations [3, 39] of the DWI pipeline. This would facilitate gaining a better understanding of how uncertainties propagate through the whole system.

REFERENCES

[1] Helmut Alt and Michael Godau. "Computing the Fréchet distance between two polygonal curves". In: *International Journal of Computational Geometry & Applications* 5.01n02 (1995), pp. 75–91.

[2] Peter J Basser et al. "In vivo fiber tractography using DT-MRI data". In: *Magnetic resonance in medicine* 44.4 (2000), pp. 625–632.

[3] Timothy EJ Behrens et al. "Characterization and propagation of uncertainty in diffusion-weighted MR imaging". In: *Magnetic Resonance in Medicine: An Official Journal of the International Society for Magnetic Resonance in Medicine* 50.5 (2003), pp. 1077–1088.

[4] Ralph Brecheisen et al. "Parameter sensitivity visualization for DTI fiber tracking". In: *IEEE Transactions on Visualization and Computer Graphics* 15.6 (2009), pp. 1441–1448.

[5] Anders Brun et al. "Clustering fiber traces using normalized cuts". In: *Medical Image Computing and Computer-Assisted Intervention–MICCAI 2004: 7th International Conference, Saint-Malo, France, September 26-29, 2004. Proceedings, Part I 7*. Springer. 2004, pp. 368–375.

[6] Dan G Cacuci. "Sensitivity theory for nonlinear systems. I. Nonlinear functional analysis approach". In: *Journal of Mathematical Physics* 22.12 (1981), pp. 2794–2802.

[7] Guoning Chen et al. "Efficient Morse decompositions of vector fields". In: *IEEE Transactions on Visualization and Computer Graphics* 14.4 (2008), pp. 848–862.

[8] Isabelle Corouge, Sylvain Gouttard, and Guido Gerig. "Towards a shape model of white matter fiber bundles using diffusion tensor MRI". In: *2004 2nd IEEE international symposium on biomedical imaging: nano to macro (IEEE Cat No. 04EX821)*. IEEE. 2004, pp. 344–347.

[9] Isabelle Corouge et al. "Fiber tract-oriented statistics for quantitative diffusion tensor MRI analysis". In: *International Conference on Medical Image Computing and Computer-Assisted Intervention*. Springer. 2005, pp. 131–139.

[10] Isabelle Corouge et al. “Fiber tract-oriented statistics for quantitative diffusion tensor MRI analysis”. In: *Medical image analysis* 10.5 (2006), pp. 786–798.

[11] Jin Er et al. “Data-driven automatic segmentation algorithm for trigeminal nerve fiber”. In: *Chinese Journal of Biomedical Engineering* 39.4 (2020), pp. 385–393.

[12] Andriy Fedorov et al. “3D Slicer as an image computing platform for the Quantitative Imaging Network”. In: *Magnetic resonance imaging* 30.9 (2012), pp. 1323–1341.

[13] Christoph Garth et al. “Efficient computation and visualization of coherent structures in fluid flow applications”. In: *IEEE Transactions on Visualization and Computer Graphics* 13.6 (2007), pp. 1464–1471.

[14] Casey Brett Goodlett. “Computation of statistics for populations of diffusion tensor images”. PhD thesis. School of Computing, University of Utah, 2009.

[15] Carlos Enrique Gutierrez et al. “Optimization and validation of diffusion MRI-based fiber tracking with neural tracer data as a reference”. In: *Scientific reports* 10.1 (2020), pp. 1–18.

[16] Mark Harrower and Cynthia A Brewer. “ColorBrewer. org: an online tool for selecting colour schemes for maps”. In: *The Cartographic Journal* 40.1 (2003), pp. 27–37.

[17] Mario Hlawitschka et al. “Direct visualization of fiber information by coherence”. In: *International journal of computer assisted radiology and surgery* 5 (2010), pp. 125–131.

[18] Hao Huang et al. “Analysis of noise effects on DTI-based tractography using the brute-force and multi-ROI approach”. In: *Magnetic Resonance in Medicine: An Official Journal of the International Society for Magnetic Resonance in Medicine* 52.3 (2004), pp. 559–565.

[19] Jiahao Huang et al. “Automatic oculomotor nerve identification based on data-driven fiber clustering”. In: *Human Brain Mapping* 43.7 (2022), pp. 2164–2180.

[20] Yuankai Huo et al. “Spatially localized atlas network tiles enables 3D whole brain segmentation from limited data”. In: *Medical Image Computing and Computer Assisted Intervention–MICCAI 2018: 21st International Conference, Granada, Spain, September 16-20, 2018, Proceedings, Part III 11*. Springer. 2018, pp. 698–705.

[21] Anil K Jain and Richard C Dubes. *Algorithms for clustering data*. Prentice-Hall, Inc., 1988.

[22] Anil K Jain, M Narasimha Murty, and Patrick J Flynn. “Data clustering: a review”. In: *ACM computing surveys (CSUR)* 31.3 (1999), pp. 264–323.

[23] Ben Jeurissen et al. “Investigating the prevalence of complex fiber configurations in white matter tissue with diffusion magnetic resonance imaging”. In: *Human brain mapping* 34.11 (2013), pp. 2747–2766.

[24] Fangxiang Jiao et al. “Metrics for uncertainty analysis and visualization of diffusion tensor images”. In: *International Workshop on Medical Imaging and Virtual Reality*. Springer. 2010, pp. 179–190.

[25] Derek K Jones and Mara Cercignani. “Twenty-five pitfalls in the analysis of diffusion MRI data”. In: *NMR in Biomedicine* 23.7 (2010), pp. 803–820.

[26] Denis Le Bihan et al. “Diffusion tensor imaging: concepts and applications”. In: *Journal of Magnetic Resonance Imaging: An Official Journal of the International Society for Magnetic Resonance in Medicine* 13.4 (2001), pp. 534–546.

[27] Francois Lekien, Shawn C Shadden, and Jerrold E Marsden. “Lagrangian coherent structures in n-dimensional systems”. In: *Journal of Mathematical Physics* 48.6 (2007), p. 065404.

[28] Monique Meuschke et al. “Combined visualization of vessel deformation and hemodynamics in cerebral aneurysms”. In: *IEEE transactions on visualization and computer graphics* 23.1 (2016), pp. 761–770.

[29] Monique Meuschke et al. “Visual analysis of aneurysm data using statistical graphics”. In: *IEEE transactions on visualization and computer graphics* 25.1 (2018), pp. 997–1007.

[30] Bart Moberts, Anna Vilanova, and Jarke J Van Wijk. “Evaluation of fiber clustering methods for diffusion tensor imaging”. In: *Proceedings of IEEE Visualization*. IEEE. 2005, pp. 65–72.

[31] Susumu Mori and Peter CM Van Zijl. “Fiber tracking: principles and strategies–a technical review”. In: *NMR in Biomedicine: An International Journal Devoted to the Development and Application of Magnetic Resonance In Vivo* 15.7-8 (2002), pp. 468–480.

[32] Sinisa Pajevic and Carlo Pierpaoli. “Color schemes to represent the orientation of anisotropic tissues from diffusion tensor data: application to white matter fiber tract mapping in the human brain”. In: *Magnetic Resonance in Medicine: An Official Journal of the International Society for Magnetic Resonance in Medicine* 42.3 (1999), pp. 526–540.

[33] Arish A Qazi et al. “Resolving crossings in the corticospinal tract by two-tensor streamline tractography: Method and clinical assessment using fMRI”. In: *Neuroimage* 47 (2009), T98–T106.

[34] R Tyrrell Rockafellar and Roger J-B Wets. *Variational analysis*. Vol. 317. Springer Science & Business Media, 2009.

[35] Filip Sadlo and Ronald Peikert. “Efficient visualization of Lagrangian coherent structures by filtered AMR ridge extraction”. In: *IEEE Transactions on Visualization and Computer Graphics* 13.6 (2007), pp. 1456–1463.

[36] Juergen R Schlaier et al. “Probabilistic vs. deterministic fiber tracking and the influence of different seed regions to delineate cerebellar-thalamic fibers in deep brain stimulation”. In: *European Journal of Neuroscience* 45.12 (2017), pp. 1623–1633.

[37] Jeremy D Schmahmann et al. “Association fibre pathways of the brain: parallel observations from diffusion spectrum imaging and autoradiography”. In: *Brain* 130.3 (2007), pp. 630–653.

[38] Tom Schonberg et al. “Characterization of displaced white matter by brain tumors using combined DTI and fMRI”. In: *Neuroimage* 30.4 (2006), pp. 1100–1111.

[39] Thomas Schultz et al. “Fuzzy fibers: Uncertainty in dMRI tractography”. In: *Scientific Visualization*. Springer, 2014, pp. 79–92.

[40] Toshiaki Taoka et al. “Fractional anisotropy–threshold dependence in tract-based diffusion tensor analysis: evaluation of the uncinate fasciculus in Alzheimer disease”. In: *American Journal of Neuroradiology* 30.9 (2009), pp. 1700–1703.

[41] J-Donald Tournier, Fernando Calamante, and Alan Connelly. “Robust determination of the fibre orientation distribution in diffusion MRI: non-negativity constrained super-resolved spherical deconvolution”. In: *Neuroimage* 35.4 (2007), pp. 1459–1472.

[42] David S Tuch et al. “High angular resolution diffusion imaging reveals intravoxel white matter fiber heterogeneity”. In: *Magnetic Resonance in Medicine: An Official Journal of the International Society for Magnetic Resonance in Medicine* 48.4 (2002), pp. 577–582.

[43] Raphael Voltoline and Shin-Ting Wu. “Multimodal visualization of complementary color-coded FA map and tensor glyphs for interactive tractography ROI seeding”. In: *Computers & Graphics* 96 (2021), pp. 24–35. ISSN: 0097-8493.

[44] Florian Weiler and Horst K Hahn. “An interactive ROI tool for DTI fiber tracking”. In: *Medical Imaging 2011: Visualization, Image-Guided Procedures, and Modeling*. Vol. 7964. SPIE. 2011, pp. 941–947.

[45] Song Zhang, Cagatay Demiralp, and David H Laidlaw. “Visualizing diffusion tensor MR images using streamtubes and streamsurfaces”. In: *IEEE Transactions on Visualization and Computer Graphics* 9.4 (2003), pp. 454–462.

7

EFFECT OF WHITE MATTER UNCERTAINTY VISUALIZATION IN NEUROSURGICAL DECISION MAKING

In the previous chapters, we have addressed the key sources of uncertainties in DTI pipeline and proposed interactive techniques for the effective visualization of the uncertainties. This chapter changes focus where we assess the potential impact of uncertainty visualization on neurosurgical decision-making. In general, many techniques have been developed to visualize uncertainties, however, there is limited evidence to suggest whether these uncertainty visualization influences neurosurgical decision-making. In this chapter, we evaluate the hypothesis that uncertainty visualization in fiber tracking influences neurosurgeon's decisions and confidence in their decisions. We conducted a user study using an online interactive questionnaire to assess the impact of uncertainty visualization on neurosurgical decision-making with clinically relevant cases. The results indicate that uncertainty visualization affects participants' decisions, albeit its extent is also influenced by other factors. Additionally, our analysis found no clear relationship between the presented uncertainty intervals and participants' confidence in their decisions. This chapter is based on the paper:

> Siddiqui, F., Brouwers, H. B., Rutten, G. J., Höllt, T., and Vilanova, A. (2024). Effect of white matter uncertainty visualization in neurosurgical decision making. IEEE Computer Graphics and Applications, vol. 45, no. 1, pp. 106-121, Jan.-Feb. 2025. https://doi.org/10.1109/MCG.2024.3462926.

7.1. INTRODUCTION

Numerous techniques have been presented in the literature for visualizing uncertainties in the context of fiber tracking [20]. However, there are no studies to indicate how uncertainty visualization influences reasoning and decision-making. While some studies evaluate the impact of uncertainties on decision-making in general [14], extrapolating these results to the context of fiber tracking proves challenging. This difficulty arises due to the intricate task of representing uncertainty in complex objects like fiber tracts, which contrasts with the relative simplicity of handling uncertainty in scalar values like a vessel diameter.

In this work, we address this gap by designing and implementing a user study that provides insights into whether the visualization of uncertainty in fiber tracking results can affect neurosurgical decision-making. To facilitate this study, we implemented a framework to visualize uncertainty information within a fiber tracking visualization, based on previous work [21]. We use this framework to embed interactive 3D views in an online questionnaire, allowing participants to explore and interact with the uncertainty visualization. This implementation ensured that our questionnaire was grounded in practical and clinically relevant scenarios, and provided the necessary information to answer the questionnaire. Drawing from the hypotheses presented by Padilla et al. [14], we hypothesize that the representation of uncertainty will influence participants' judgments, leading them to make more cautious decisions as the presented uncertainty increases. In this work, we use different confidence intervals to show such varying levels of uncertainty. To not confuse these with the confidence of participants in their decision, that we also want to test, we call them *uncertainty intervals* in the remainder of this paper. Accordingly, we have formulated the following hypotheses based on the role of uncertainty in decision making:

- **H1:** Visualization of uncertainty will influence the participants' decision.
- **H2:** Participants will make a more cautious decision when a larger uncertainty interval is visualized.
- **H3:** Confidence of the participants in decision-making will be affected by the uncertainty visualization.

7.2. CLINICAL DECISION MAKING

We already discussed the clinical background relevant for this study in Section 2.2. In this section, we introduce the basic concepts related to understand the clinical decision making process.

While MRI-based fiber tractography is commonly used as a non-invasive tool to analyze white matter fiber tracts before surgery, intraoperative neuromonitoring [18] (IONM) is considered the gold standard method to identify white matter tracts. White matter tracts are not visible when the brain tissue is directly inspected during tumor resection. IONM keeps the patient awake and, through electrical stimulation, allows the surgeon to identify whether specific fiber tracts are present. For example, the patient is asked to speak; if, with direct stimulation of the tissue, the patient experiences

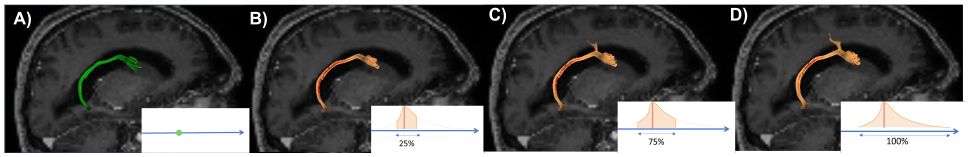

Figure 7.1: Uncertainty intervals for the Arcuate Fasciculus bundle. A) No uncertainty B) 25% interval visualization C) 75% interval visualization D) 100% interval visualization

difficulties speaking, it indicates that the language tract is in the stimulated area and, therefore, should be avoided. Although it has been shown that IONM in an awake setting improves both the surgical extent of resection and postoperative neurological status, it adds discomfort and complexity to the procedure and is avoided if possible. However, it is currently not known which patients will benefit from IONM [6]. Generally speaking, when there is a margin between the tumor border and specific critical functional brain regions or tracts, surgeons will refrain from using IONM. However, this is a qualitative judgement: margins are seldom specified in the literature, and there is significant variability in decision-making between neurosurgeons even within a neurosurgical center.

7.3. RELATED WORK

Decision making is a common goal for visualization, yet Dimara et al. [3] suggested that visualization studies largely lack explicit ties to decision making. In uncertainty visualization, Hullman [7] presented the complexities in the effective communication of the uncertainty results and highlighted the risk if the results are not properly communicated. Although uncertainty visualization has a strong tradition of empirical research in visual design and user comprehension, research into the effectiveness of uncertainty visualization as it relates to decision support remains critical and an important area of work [2]. Researchers have emphasized the need for empirical research to test the effectiveness of visual representations of uncertainty and their usefulness in the decision-making process [13].

A few studies in the field of psychology showed that providing uncertainty information has a positive influence on decision-making. In a study conducted by Roulston et al. [17], participants made more accurate decisions when standard errors were presented in addition to a point estimate. Joslyn et al. [9] evaluated decision making when involving uncertainty in weather forecasts, and the results suggest that uncertainty information improved decision quality overall and increased trust in the forecast. Padilla et al. [14] evaluated participants' judgment in the presence of direct and indirect uncertainties. The results suggest that participants could incorporate the communicated uncertainty into their judgments relatively accurately. Similar results were observed in other application scenarios, such as weather forecasting [16] or flood forecasting [15]. However, some studies suggest that uncertainty visualization has little to no effect compared to decisions made without uncertainty [10]. Overall, findings regarding the impact of uncertainty visualizations are varied, highlighting the substantial influence of visualization selection on comprehension.

Clinical decision-making is a unique process that involves the interplay between knowledge of pre-existing pathological conditions, explicit patient information, and the provided imaging data. Clinical decisions can have substantial consequences and involve many sources of uncertainties that may critically hamper the decision-making process. In a recent study, Gillmann et al. [5] provided a survey of uncertainty-aware visualization in medical imaging and emphasized the need for empirical research to analyze the effectiveness of the presented uncertainty visualization techniques. Galesic [4] presented icon arrays to communicate medical risk and the results suggested that this technique improved the accuracy of the understanding of the risk in wide range of patient groups. McDowell and Kause [11] investigated how different types of uncertainty in medical evidence affect perception when presented through tables, bar graphs, and icon arrays. They found that clear and well-designed displays of uncertainty did not negatively affect participants' understanding or trust in the information. This suggests that the way uncertainty is presented visually is more important than the specific type of uncertainty being communicated. To the best of our knowledge, there does not exist any research on the influence of uncertainty visualization in the decision making process that includes information from fiber tracking. In our work, we took inspiration from the studies on the effect of uncertainty visualization in decision-making from the field of psychology [14] and visualization [8] and designed our study to test the effectiveness and consequences of uncertainty visualization in neurosurgical decisions.

7.4. STUDY DESIGN

We embraced the context as employed in the study by Padilla et al. [14], where the impact of uncertainty visualization on decision-making is evaluated on the weather forecaster by manipulating uncertainty intervals in the results and analyzing how the decisions are changing based on these presented uncertainties. Padilla et al. [14], showed participants the distribution of possible variations in temperature based on an artificial scenario and were tasked to make a decision. They found that participants made more informed and cautious decisions when uncertainty was shown. Based this work, we aim to analyze the impact of uncertainty visualization on clinical decision making, specifically when showing uncertainty for fiber tracking results.

We want to test whether the participants have taken uncertainty visualization into account (H1), they made a more cautious decision when uncertainty was visualized (H2), and to whether their confidence was influenced (H3). To do so, we present eight patient/uncertainty combinations to each participant in a mixed-design setup. For each patient, four different uncertainty intervals were created (see Figure 7.1 for one example patient), from which two are randomly drawn for each participant. Each participant sees all four different clinical cases or patients (see Figure 7.2). The resulting eight patient/uncertainty combinations are then shown to the participants in random order (Figure 7.3). This allows us to track changes for the decision for a patient within-participant, but general claims over all uncertainty levels can only be done between-participants. We performed a formative user study using an interactive online questionnaire presented to surgeons who use fiber tracking in their clinical workflow. The design of the user study was an iterative process involving multiple meetings and interviews with a panel of neurosurgeons.

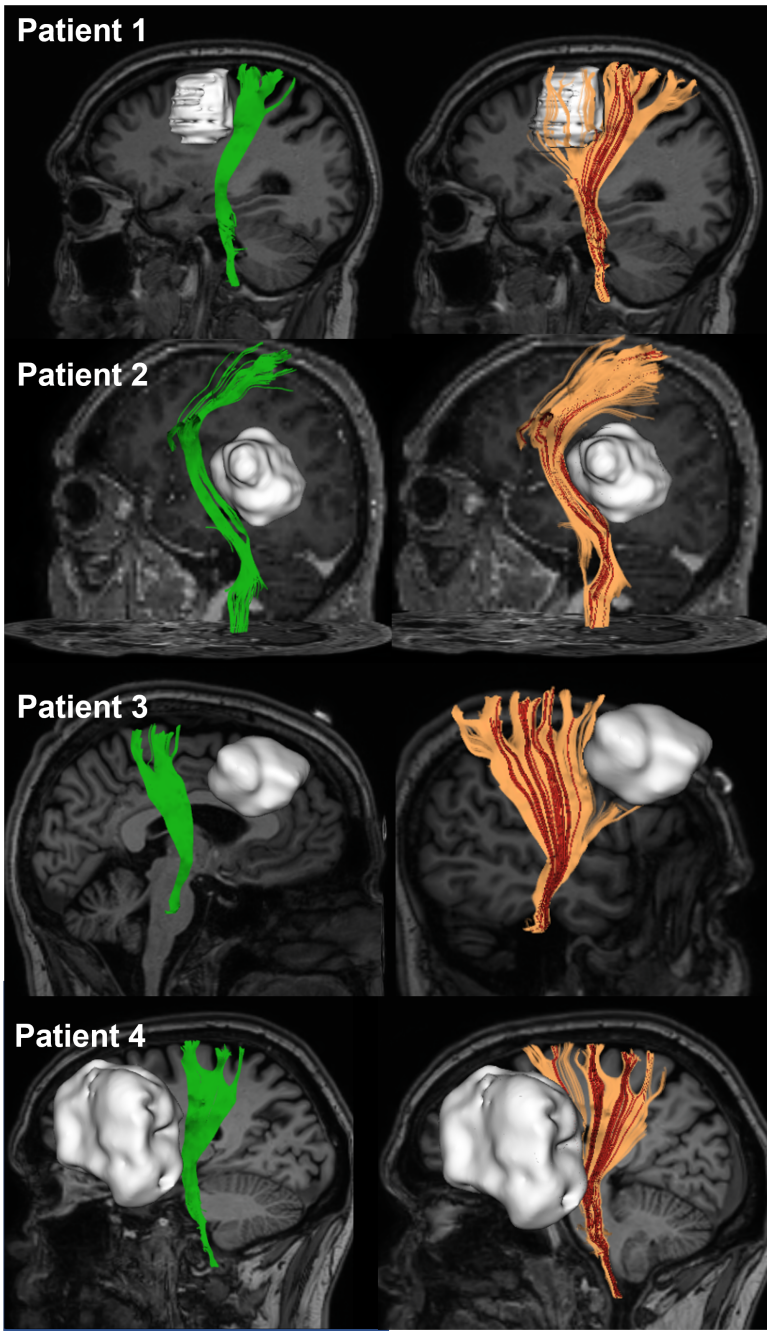

Figure 7.2: Cases of the four patient data sets used in the evaluation. Left: Fiber tracking results without uncertainty information. Right: Fiber tracking results with 100 % interval of uncertainty visualization

7.4.1. EXPERT INSIGHTS AND INITIAL INTERVIEWS

During the initial design phase of the study, we conducted the first round of interview sessions with four oncology neurosurgeons and two researchers in neurosurgery to gain insights into their approach to analyze fiber tracking results and to identify specific scenarios where uncertainty visualization would be relevant. We discussed how the resulting fiber tracts affect the neurosurgical decision-making process through semi-structured interviews. Decision making in neurosurgical context is complex. Different decisions are taking place and many factors beyond fiber tracking influence the decisions. We identify the scenarios, and the formulation of the questions such that the neurosurgeons answers would be focused on the fiber tracking uncertainty visualization and not in other external factors. For example, it was identified that the decision on IONM was the most appropriate for our purposes and that gliomas would be the type of tumors to study. The questionnaire was presented and refined in four feedback moments with our collaborators. During these feedback sessions, the information and interactions that should be provided to neurosurgeons to evaluate the cases were also discussed. Furthermore, together with the neurosurgeons and radiologists, we prepared clinically relevant data sets for the participants. The neurosurgeons suggested seven data sets from their past experiences, where fiber tracking results played an important role in decision-making. We prepared the results with uncertainty visualization which were discussed in the interactive sessions with the collaborators to select the most appropriate ones.

7.4.2. FIBER TRACKING AND UNCERTAINTY COMPUTATION

Our work involves assessing the impact of uncertainty on decision-making in brain tumor surgery where information from fiber tracking is available, regardless of the specific fiber tracking and uncertainty visualization techniques employed. For this purpose, the fiber ensembles were generated together with our collaborators. We followed the workflow that is currently used in their practice as close as possible. The fiber tracking process starts with the manual definition of the seed region from which the seed point for each fiber tract is drawn. In scenarios without uncertainty information, we employ deterministic fiber tracking [12], a widely utilized method in the standard clinical workflow. Conversely, when uncertainty information is integrated, we adopt the bootstrapping method [21]. The result of this process is an ensemble of tracts for each seed point, representing the possible variations for the corresponding fiber.

7.4.3. UNCERTAINTY VISUALIZATION

Without uncertainty, the fibers are visualized as green tubes, as shown in Figure 7.1A.

For the uncertainty visualization, we compute the median and uncertainty interval for each fiber by calculating the distances among fiber pairs based on a chosen measure, presented by Brecheisen et al. [1]. The median, termed as the representative fiber, is determined by considering the minimum accumulated distance to all the other fibers in the ensemble and, as such, can be seen as the most central fiber. In addition, all other fibers are ordered according to their distances to the representative fiber such that the uncertainty intervals can be defined on the resulting distribution. For example, a uncertainty interval of 25% includes the 25% fibers with lower distance to the representative

fiber. For the visualization, the representative fibers are shown as red tubes, and the remaining fiber samples that correspond to the selected interval, as illuminated polylines in orange (Figure 7.1B-D). This is a simple visualization, similar to the standard representation our collaborators are used to, where all fibers corresponding to one interval are shown, indicating the uncertainty interval also visually. The visualization makes sure that the representative fiber is always visible by drawing it on top [21]. The uncertainty intervals can be selected to understand the distribution better. To cover a meaningful variety of uncertainty information we chose several different uncertainty intervals for inclusion in the questionnaire, originally based on quartiles, including 0% and 100%. At the same time, after discussion with our collaborators, it also became clear that we must keep the number of different uncertainty intervals small to not overburden participants with too many cases. Thus, we removed the 50% uncertainty interval to reduce the number of tests. As a result we ended up with three uncertainty intervals in addition to no uncertainty: 25%, 75%, and 100%, shown in Figures 7.1B, C, and D, respectively.

7.4.4. PATIENT CASES

We chose four different anonymized patient datasets for testing our hypotheses shown in Figure 7.2 without uncertainty and with a 100% interval. Four cases were considered a good number to generalize from the nuances of each specific case. Given the complexity of the problem, more cases were seen as unfeasible. The cases were selected based on suggestions by our collaborating neurosurgeons. Specifically, we focus on cases where the tumor is present in the vicinity of the corticospinal tract, and the tracts are distorted with the presence of the tumor. This tract plays a critical role in motor functioning. Damage will very likely result in severe and permanent motor deficits. Neurosurgeons will not risk damaging the corticospinal tract to improve the extent of tumor resection. These cases were selected since for all of them it is not obvious, whether the procedure should be carried out using IONM or not. There is a balance of risks between full tumor resection and damage to the motor tract. Using IONM would be a conservative decision but it involves invasiveness and higher costs of the procedure. This means that it is not possible to know what is the correct choice before the procedure. I.e., there is no ground truth or correct answer. Note, testing for the correct answer is also not the goal of this study, but rather evaluating whether showing uncertainty has an impact in the decision making.

7.4.5. PATIENT/UNCERTAINTY COMBINATION

For each patient fiber tracking results are then prepared with the uncertainty intervals discussed above: no uncertainty 25% (Low interval), 75% (Medium interval), and 100% (High interval) as shown for one example in Figure 7.1. Combining the four patients with four uncertainty intervals creates a total of 16 cases. To not overburden the participants, we decided to draw eight pseudo-random cases to review for each participant in the study. As discussed above, each participant was presented with all four patients but only two randomly selected two uncertainty intervals per patient. Cases were shown in random order but the same patient was never shown consecutively to reduce further learning biases. The complete process is also illustrated in Figure 7.3. As a result, all participants had an equal opportunity to explore cases from all four patients with varying uncertainty intervals.

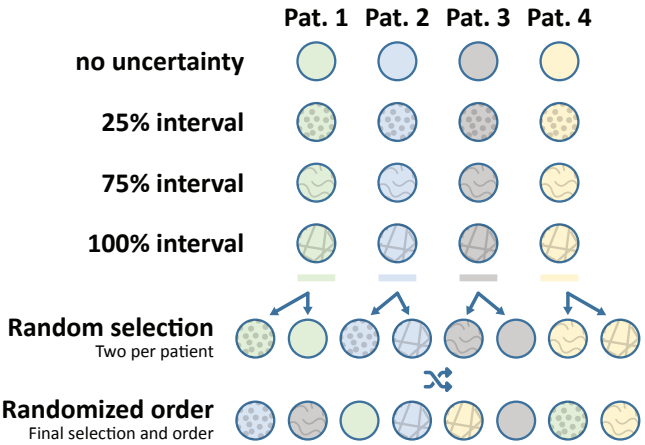

Figure 7.3: The distribution of the cases among participants.

7.5. QUESTIONNAIRE

In this section, we discuss the process behind formulating the evaluation questionnaire and elaborate on its integration into the interactive web app designed for the evaluation[a].

7.5.1. HYPOTHESIS DRIVEN QUESTION FORMULATION

One of the main aspects of the design of the questionnaire are the questions to be asked per presented case. We aim at concrete question(s) that can be used to compare and analyze the decision making of the participants. We held a number of meetings with collaborators. Here, we discussed the surgeons' routine decisions during fiber tracking analysis. These vital choices involve diverse aspects, like planning tumor resection paths, deciding on sleep or awake surgery, or utilizing Intraoperative Neurophysiological Monitoring (IONM) for surgical assistance, among others. It is important to note that these clinical decisions are also influenced by numerous other factors, including the patient's health condition, tumor type, preoperative counseling and patient preferences regarding the functional/oncological balance (operate more on the safe side or be more aggressive to maximize resection), and more. To mitigate their impact and isolate the influence of fiber tracking visualizations on decision-making, we provide the participants with specific clinical context conditions. We instructed participants, that the tumor should be assumed to be a glioma, and the patient is eligible for IONM/awake surgery, so no other factors influence the decision. We also emphasize that the quality of the generated fiber tracts and their anatomical representation is not part of the evaluation such that the answer does not diverge into the quality of the fiber tracking results or the used algorithm. It was advised by the neurosuregeons to pose only a single decision-making question per provided case to minimize the burden and potential study dropouts. Following the input from our collaborators, we defined the following main question:

[a]The questionnaire can be accessed online and is open source on GitHub.

Based on this visualization, will you recommend using Intraoperative Neurophysiological Monitoring (IONM) during the surgical procedure?

The participant has to make a binary decision, either Yes or No, based on the provided uncertainty visualization case. Participants might be inclined to utilize Intraoperative Neuromonitoring (IONM) if they believe that the tumor resection process could impact the integrity of healthy fiber bundles and if they require additional assistance throughout the procedure.

Moreover, we ask the user an optional open question to comment on their decision to understand the reasoning behind their decisions.

Would you like to comment on your decision? You may want to comment, for instance, what arguments led you to this decision?

After each question, participants were also asked about their confidence on a Likert scale ranging from 1 (not confident) to 5 (very confident):

How Confident are you about the decision?

7.5.2. INTERACTIVE 3D WEB VISUALIZATION

To be able to respond to the questions effectively based on the provided fiber tracking case results and uncertainty interval, 3D interaction with the results is necessary. We have added the needed interactions suggested by our collaborators such that the participants can effectively explore the fiber tracking and uncertainty results. The questionnaire was developed as a web application such that it could be distributed independently. In order to integrate the proposed interactions using VTKjs [19] and HTML. The basic requirement for surgeons to understand and analyze the fiber tracking results is to have an interactive 3D view in which a user can pan, rotate, and zoom. Furthermore, they need to manipulate the magnetic resonance T1-weighted slices to comprehend the relation to the anatomy. How users used those interactions was not part of the study and was not recorded to comply with data minimization goals of the host institutions' ethics guidelines for human studies.

7.5.3. QUESTIONNAIRE SETUP

To fill in the questionnaire and be a part of this study, participants were first requested to provide digital consent, indicating their willingness to partake in the study. This initial step ensured that participants were fully aware of their involvement and agreed to the terms of the study. Its to be noted that the participants were not asked for any Personal Identifiable Information (PII), such as name or email address. Once consent was obtained, the participants were asked for information about their experience with fiber tracking techniques, such as for how long they have been using fiber tracking results in their workflow. By obtaining this context, we aimed to gain insights into potential variations in the interpretation and utilization of the provided uncertainty visualization.

In the following step, participants were presented with a set of instructions that served to introduce them to the concepts of uncertainty visualization used in fiber tracking results and a description of the tasks they would undertake. These instructions were crucial in establishing a common understanding and setting the stage for the

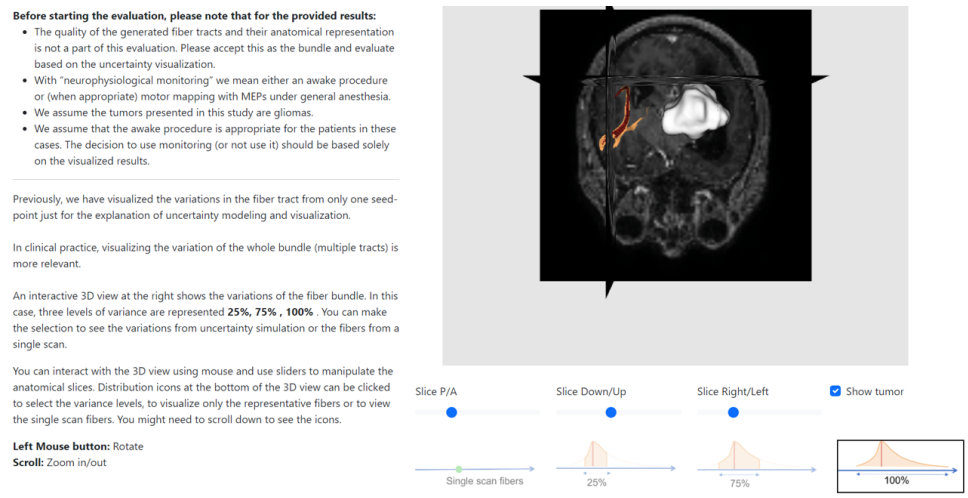

Figure 7.4: This screenshot captures the training page, delineating essential elements for the evaluation process. On the left side, detailed information regarding the assumptions made for the evaluation and instructions for utilizing the 3D interface is provided. The right side of the page features an interactive 3D interface seamlessly embedded, accompanied by controls located at the bottom for user interaction.

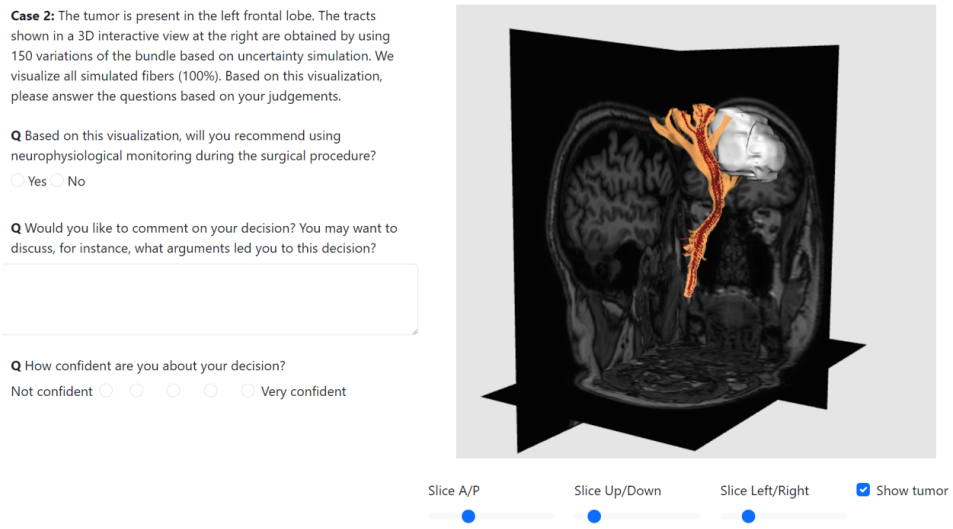

Figure 7.5: This screenshot encapsulates a specific case within the evaluation framework. On the left side, a set of questions related to the case is presented. Simultaneously, on the right side, an interactive 3D interface is integrated, facilitating a comprehensive exploration of the case, with user controls conveniently positioned at the bottom for enhanced interaction.

subsequent phases of the evaluation. Once the details are provided, participants are presented with the training page, depicted in Figure 7.4. This page served as a tangible introduction to the 3D interface participants would be utilizing throughout the evaluation process. The training page showcased the layout of the visualization and outline of how they could interact with the system, thereby allowing participants to become acquainted with the 3D interface and its features. In the training phase, participants were allowed to explore all the uncertainty intervals by selecting the corresponding icon. The participants could get familiar with the different uncertainty intervals as concepts and the consequences of making specific selections. After the training phase, participants were asked to answer questions to check if their understanding of the uncertainty visualizations presented.

In total, each participant was presented with eight different cases as discussed above. Each case was presented using an interactive 3D view showcasing the fiber tracking results, anatomical context, and the tumor on its own page, together with the corresponding questions as shown in Figure 7.5. Responses from participants were collected through the selection radio buttons and the dialog box.

By visualizing the results with and without uncertainty information along with different intervals, we were able to test if participants were switching their decision to using IONM. This allowed us to determine how the inclusion of uncertainty information changed the participant's response (H1). By analyzing their decisions based on the interval of visualized uncertainties, we can determine if the participants are making more cautious decisions with higher intervals of uncertainty visualization (H2). The question on the confidence rating allows analysis of the influence of uncertainty visualization on participants' confidence (H3). Following the participants' evaluation of all presented cases, we posed several open-ended questions concerning the uncertainty visualization in fiber tracking results. More precisely, we inquired whether the provided uncertainty information had any influence on any other clinical decisions beyond the application of IONM. Furthermore, we sought to determine whether the conveyed uncertainty information contributed to enhancing their decision-making confidence.

7.6. RESULTS

The developed web application for the questionnaire was distributed among neurosurgeons throughout the Netherlands through the Dutch Association for Neurosurgery (De Nederlandse Vereniging voor Neurochirurgie). The association includes nearly all neurosurgeons practicing in the Netherlands. However, not all of these neurosurgeons perform brain tumor surgery, and only a portion of those who do use fiber tracking in their workflow. We received responses from 16 participants who were utilizing fiber tracking for their neurosurgical planning. Among these participants, one response was incomplete, leading us to base our analysis on the data from 15 complete responses. All the participants' responses to the training phase were 100 % correct, which indicates that the participants were able to understand the uncertainty interval visualization. To assess the potential impact of distinct uncertainty visualization intervals on participants' decisions (H1 and H2) and their corresponding confidence (H3), we utilized the responses to the provided questions for each case. We refrain from quantitative statistical analysis given the limited amount of samples. Therefore, we opt for a qualitative analysis.

7.6.1. IMPACT ON DECISIONS (H1 AND H2)

We start our analysis by examining the choices made by participants in response to the question *"Will you recommend using Intraoperative Neurophysiological Monitoring (IONM) during the surgical procedure?"* across varying uncertainty interval visualizations. Figure 7.6 shows the percentage of decisions classified as **Yes**, use IONM, and **No**, do not use IONM, across the four different visualized uncertainty intervals. The results are summarized for all cases and participant responses. As can be observed in the plot, in the absence of uncertainty visualization (no uncertainty interval), a larger proportion of participants opted not to employ IONM for tumor resection procedures, and, therefore, taking a higher risk. However, as an uncertainty interval was visualized, an indication of a shift in the trend occurred, with participants displaying a greater inclination towards utilizing IONM, as depicted with the upward trend of the orange line in the plot, thereby supporting our hypothesis H1. This indicates that participants tend to adopt more conservative decisions when confronted with visualization of higher uncertainty intervals, providing support for hypothesis H2.

Figure 7.7 further divides the results into patient-specific trends to identify whether there were biases depending on the data sets (see Figure 7.2 as reference). The results depict the percentage of decisions classified of all participants for the four different patients. The results are similar to the overall results as shown in Figure 7.6. For Patient 1 and Patient 4, all participants opted for **Yes** for the 75% and 100% uncertainty interval visualizations. However, for Patient 2 and Patient 3, there is larger disagreement among participants. Independently of the visualized uncertainty interval, some participants chose **No**. This diversity in decisions can be attributed to the less clear margins of the tumor for Patients 2 and 3. The results indicate that uncertainty visualization impacts decision-making differently across different patients and participants.

For further analysis of the results, Figures 7.8 and 7.9 summarize the decisions and changes thereof for each participant individually. We want to account for participants intrinsic biases, for example, being prone to take more risks than others. We are interested in the changes in decision-making due to uncertainty visualization, not necessarily on the exact decision concerning IONM. Figure 7.8 depicts the count of the responses per

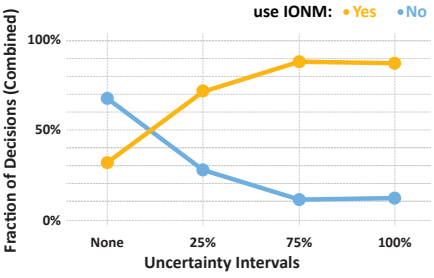

Figure 7.6: Overview of the trend of decisions taken by all participants (in percent) for the different uncertainty intervals.

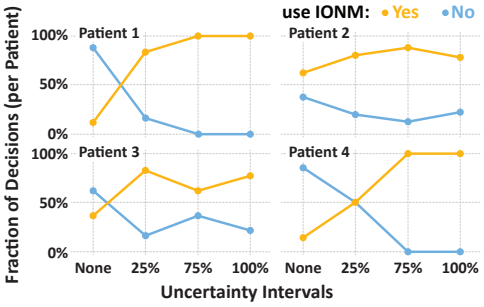

Figure 7.7: Combined result of the decision taken (in percent) versus uncertainty intervals per patient.

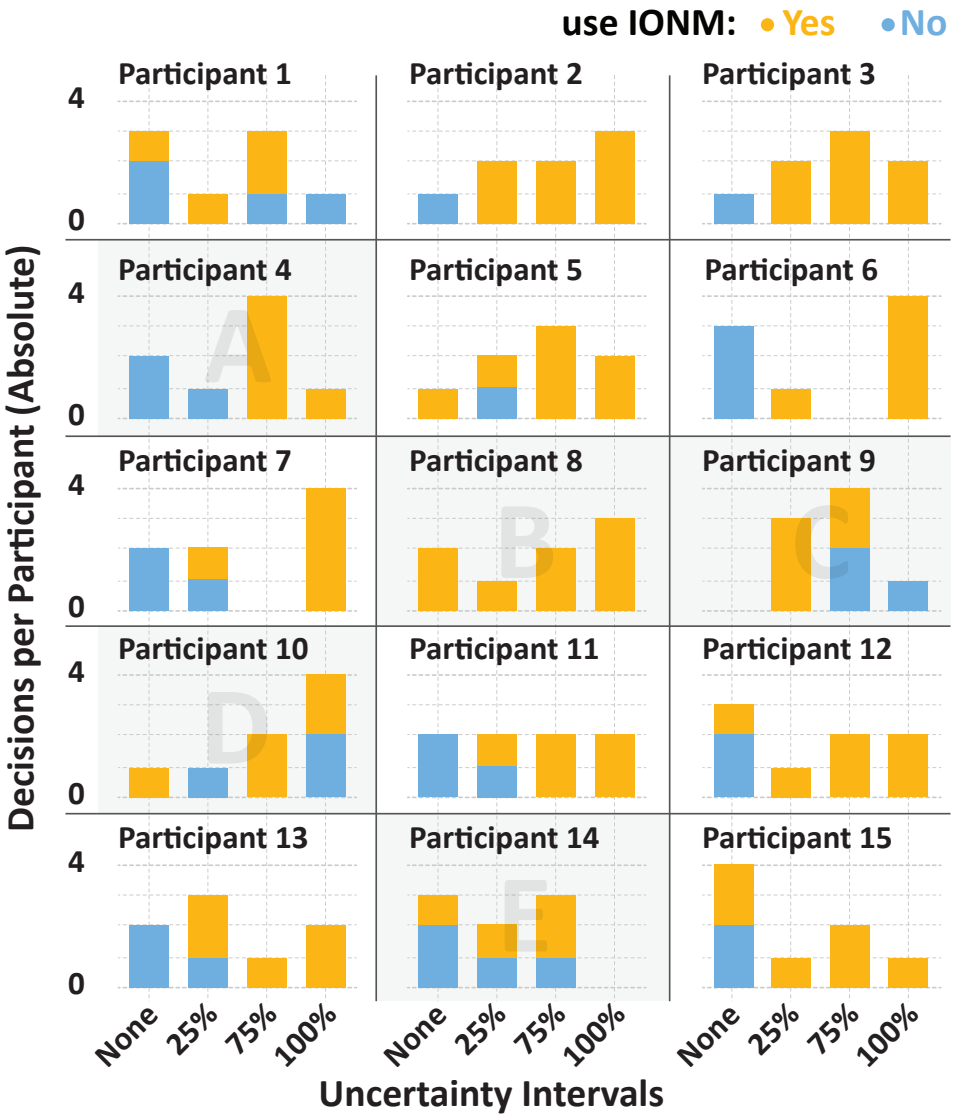

Figure 7.8: Count of the binary decisions versus uncertainty intervals for each participant.

participant for each uncertainty interval accumulating over the four presented patients (see *Section 7.4: Study Design*).

Figure 7.9 presents the individual decisions as dots to highlight variation in the decisions per participant for different uncertainty intervals and per patient data-set. Therefore, the participant panels are further subdivided into four quadrants for the four patients (same order as Figure 7.7). The two dots corresponding to the two different uncertainty intervals for the same patient are connected to indicate change in decision.

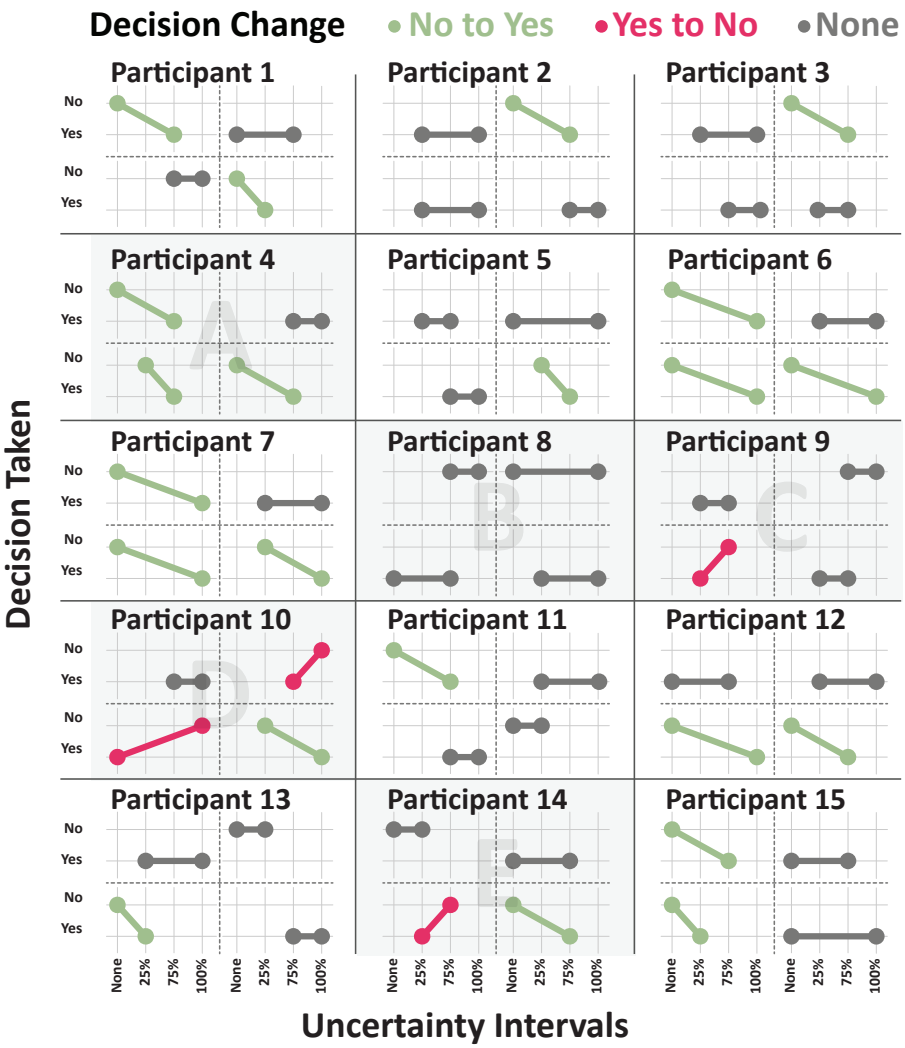

Figure 7.9: Change in participants' decision with uncertainty intervals. Dots represent the individual decision per participants for different uncertainty intervals and per patient data-set. The plots are further subdivided into four quadrants for the four patients. The dots are connected to indicate the change in decision.

Green lines denote instances where the decision changed from No to Yes meaning changing to a less risky decision, while red lines signify the opposite, indicating a shift towards a more risky decision which is less expected. Grey lines indicate no change in the decision. Figure 7.8 underscores the general trend of participants shifting their decisions from No to Yes in response to larger uncertainty intervals visualized, consistent with earlier observations.

Overall, these results exhibit a consistent pattern similar to the previous results, where participants tend to favor the Yes decision when a larger uncertainty interval is visualized. No answers are mainly present when no or 25% of uncertainty is presented. Similarly, we observe in Figure 7.9 that most participants either did not change their decision ( ) or changed from No to Yes ( ) when larger uncertainty intervals were presented.

We will illustrate the results with some examples marked as **A** and **B**; and participants that behave differently than the main trend, marked **C** and **D**.

Let us first consider Participant 4 marked **A** in Figures 7.8 and 7.9. Participant 4 only makes the more conservative decision Yes once presented with uncertainty intervals of 75% and larger (see **A** in Figure 7.8). For Patient 1 (see top left corner in the panel marked **A** in Figure 7.9), Participant 4 was faced with no uncertainty and a 75% uncertainty interval. With no uncertainty presented, Participant 4 opted for No. However, when presented the 75% uncertainty interval of the same patient their decision changed to Yes. A similar effect can be seen in the answers of Participant 4 with the other patients. Their responses align with the majority of participants.

Participant 8 (**B**) consistently selects Yes for all presented cases, regardless of the interval of uncertainty visualization or the patients involved. This would indicate that this participant favors minimal risk and it is more inclined to operate with IONM regardless.

The trend of either not changing the decision or changing towards a more conservative decision when presented with higher uncertainty intervals is present in the majority of the answers. However, Participants 9, 10, and 14 (**C**, **D**, and **E**, respectively) exhibit a distinct pattern concerning Patient 3 (i.e., bottom-left corner of the respective panels in Figure 7.9). They chose No for cases with high uncertainty interval visualization and Yes for low uncertainty intervals. It is unclear why these distinct choices were made by these participants. There might be some specifics of the Patient 3 data set that make this decision different. We also observe that Participant 10 (**D**) exhibits the same distinct pattern with Patient 2, although this is not observed in any other participant.

7.6.2. IMPACT ON CONFIDENCE (H3)

To test Hypothesis H3, we analyzed the relation between participants' confidence and the visualized uncertainty interval. Figure 7.10 displays the self-reported confidence per participant, case and uncertainty interval. Participants were requested to rate their decision confidence on a 5-point Likert scale. The results offer an overview of participants' confidence across different uncertainty scenarios. We can observe two main trends: participants have a rather constant confidence level that is not influenced by the presented uncertainty (i.e., Participants 1, 2, 3, 5, 10, 11, 12, 14, 15) or there is a slight correlation between confidence and intervals of uncertainty (i.e., Participants 4, 6, 7, 8, 13). Participant 9 (**C**) is the only participant that shows a negative correlation with the visualized uncertainty interval.

These results provide initial insights into how uncertainty visualization impacts confidence of participants in their decisions (H3). The visualized uncertainty intervals mostly seem to not influence the level of confidence, while for a few participants, they slightly correlate with the level of confidence positively.

Analogous to the previous section, we also want to examine whether the confidence

of the participants changes with increasing uncertainty intervals. Figure 7.11 presents the changes in the confidence level of each participant for all four patients along with the uncertainty interval. Similar to above, green lines indicate increasing confidence while red lines represent decreasing confidence. Flat grey lines indicate no change in confidence. The chart reveals that the dominant trend is no change

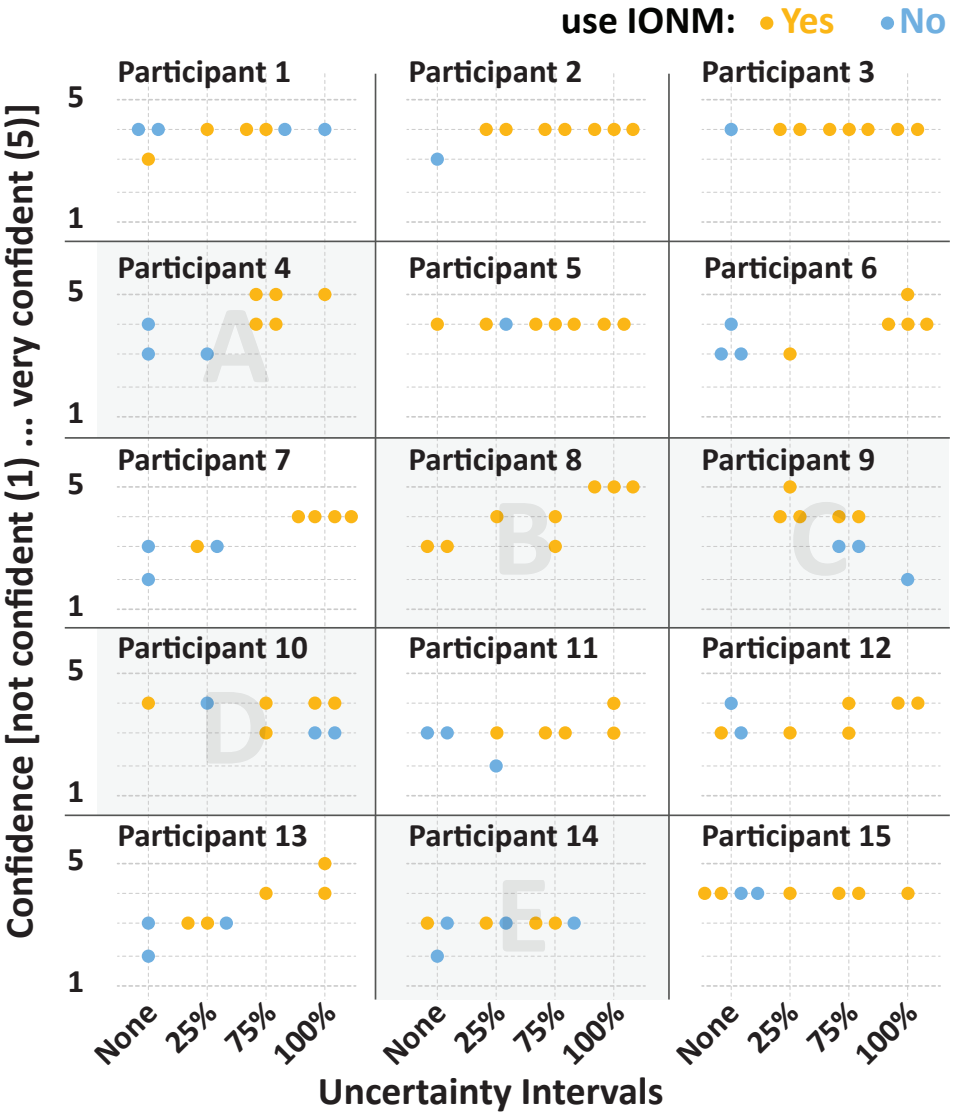

Figure 7.10: Overview of the participants' confidence across different uncertainty intervals visualizations and cases. Each point represents one of the eight cases that each participant addressed. The answer to the decision of using IONM is shown in orange for Yes and blue for No.

in confidence (38 cases), followed by increase in confidence (18 cases) and only four occurrences with a decrease in confidence. The confidence of Participants 9 and 10 (**C** and **D**, respectively) decreased, coinciding with the change of decision from **Yes** to **No** in Patient 3. These results confirm the results from Figure 7.10, although here we looked at the concrete change in confidence within the same decision context, i.e., patient.

7.6.3. FURTHER INFORMATION

We also compiled data regarding the years of professional experience of each participant to conduct an analysis of the relationship between their experience and decision-making processes. However, we did not identify any correlation between experience and the answers to the questionnaire and thus omit the data in this presentation.

Open-ended responses for each case were rather limited and focused mainly on clarifying the use of the distance from the tumor to the fiber tracts presented. A total of four participants responded to each open-ended question for all the cases, while others just responded once or twice. In total, we got 43 responses. Some examples being *"Too close, I would recommend using monitoring"*, *"In the results shown by DTI, the tracts are close proximity with edema and glioma"*, and *"there is enough space and window to remove the tumor."* These responses indicate that the decision making is highly dependent on the distance of the fibers to the tumor. However, the answers do not reveal any reasoning concerning uncertainty.

7.7. DISCUSSION

The findings from this study indicate that participants incorporate the uncertainty information presented alongside the fiber tracking results into their decision-making process. When faced with visualizations showing higher uncertainty, participants tended to make more cautious judgments, as depicted in Figure 7.6 and Figure 7.7. Both analyses provided support for the hypotheses, largely aligning with the expected patterns which also align with the results of the study by Padilla [14]. Nevertheless, certain individual responses displayed distinct behaviors. For instance, Participant 8 (**B**) consistently favored employing IONM. It is difficult to speculate about what accounts for the lack of an impact of uncertainty visualization in the participant's decision. Participants 9, 10, and 14 (**C**, **D**, and **E**) opted for not using IONM when presented with higher uncertainty intervals for Patient 3. However, the confidence of Participants 9 and 10 (**C** and **D**) also decreased. Possible reasons might be participants ignoring the uncertainty information or making extremely cautious decisions. There might be some particular context of Patient 3 that contributed to these decisions. However, we could not identify any such cause. Furthermore Participant 9 (**C**) seems to have an overall different behaviour changing the decision making to a more risky situation, i.e., **No** IONM, when presented with higher intervals of uncertainty. Furthermore, the participant was the only one that showed a negative correlation of uncertainty with confidence. The participant might be an outlier on the decision-making process, or other factors had influence. Some of these factors could be misunderstanding what was presented or how uncertainty influenced the decision process was different than the rest of participants. However, within this study, we could not identify any such factors. Given the limited number of participants, a statisti-

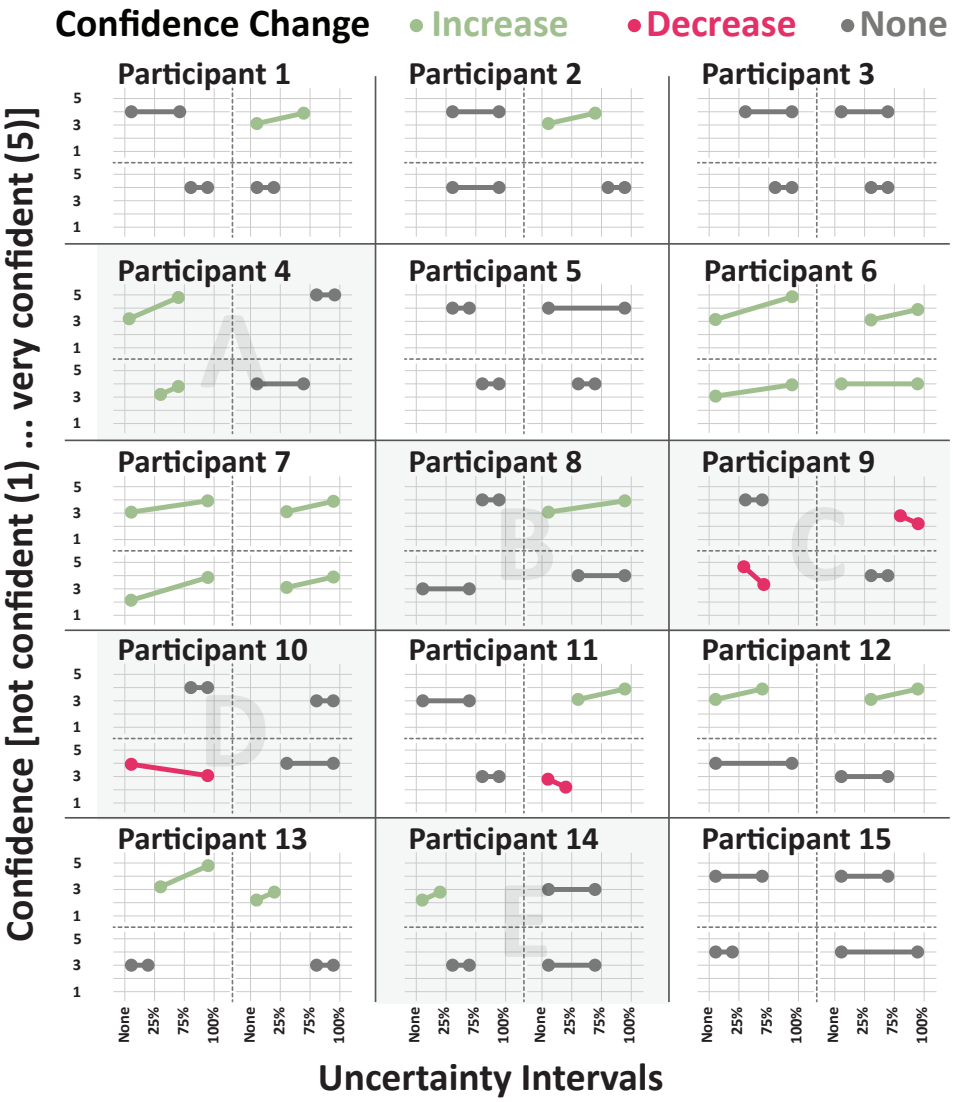

Figure 7.11: Change in participants' confidence with increasing uncertainty intervals. Dots represent the selected confidence per participant for different uncertainty intervals and per patient data-set. The plots are further subdivided into four quadrants for the four patients. The dots are connected to indicate the change in confidence.

cal analysis was not possible. However, the qualitative evaluation of the evidence shows the trends where uncertain information gives more cautious decisions.

It is important to acknowledge that numerous factors exert influence on neurosurgical decisions, including tumor type, or patient age. Despite our efforts to isolate uncertainty visualization from other variables and emphasize decision-making based on the provided visualization, it is not easy to judge that the decisions are purely based on the uncertainty visualization. Our conjecture was that presenting uncertainty information might impact participants' decisions. However, upon analyzing the limited open-ended responses, it indicates that those participants based their decisions on the proximity of resulting fiber tracts to the tumor. Consequently, our analysis suggests that while participants' decisions were influenced by provided uncertainty information, their focus predominantly might lay in assessing fiber tracking margins relative to the tumor and the number of fibers and potentially ignoring the statistical information of the uncertainty intervals of the fibers. Increasing uncertainty intervals also increases the total number of fibers shown. As a result more fibers closer to the tumor will be shown. However, we had very limited responses to our open questions, and our study was not designed to clarify the reasoning made by the participants when evaluating uncertainty. A full new study to evaluate this impact should be designed to make any conclusions.

Using a web-based questionnaire allows us to reach more participants, but at the same time, it discourages the answer to open-ended questions. These are essential to understand the reasoning aspects behind the decison-making of the participants. Exploring other user-study methods that include a stronger feedback loop could help increase responses to open-ended questions.

Lastly, our analysis delved into the influence of the presented uncertainty interval on the participants' confidence in their decision. Notably, the majority of responses indicate no change in confidence for different uncertainty intervals in the same patient, while an increase in confidence could be observed in a smaller amount of cases. A detailed examination of individual cases reveals a prevailing trend of either unaltered confidence or, for a few cases, a shift towards higher levels in scenarios with greater uncertainty. Our results are rather indecisive. A correlation is not evident, the findings indicate the partial influence of uncertainty for some participants. More extensive studies would be needed to achieve stronger statements.

7.8. CONCLUSIONS AND FUTURE DIRECTIONS

In this chapter, we presented the study that was built up upon the context and hypotheses established by Padilla et al. [14] to examine how uncertainty visualization affects decision-making when dealing with intricate fiber-tracking results in brain tumor patients. Collaborating with surgeons and radiologists, we designed and implemented a user study tailored to inquire about specific clinically relevant cases and analyze participants' decisions. Our investigation centered on exploring the impact of uncertainty visualization on neurosurgical decision-making through fiber tracking results. We carefully designed an interactive web-based questionnaire that allowed the participants to explore the necessary information to answer the decision-making questions. The evaluation, guided by the presented hypotheses, provides insights into the relationship between uncertainty presentation and participants' judgments. The findings underscore

that uncertainty visualization influences participants' decisions, albeit its extent is also influenced by other factors.

As hypothesized, participants exhibited a tendency to make more cautious decisions when confronted with larger uncertainty intervals in the visualization. It should be noted, however, that the participants' decisions seem to be influenced by the number of fibers present, regardless of the statistical significance of the uncertainty interval visualization. In future studies, this should be explored to better understand the reasoning behind the decisions made.

Moreover, our analysis could not identify any clear relationship between the uncertainty intervals presented and participants' confidence in the decision-making. There is an indication of a positive correlation for some participants. Further studies are needed, to better understand the possible influence of uncertainty presentation on confidence.

Our analysis is constrained by several limitations. These limitations encompass a restricted number of users, limited data sets, limited questions, difficulty to acquire responses to open questions, and constraints related to the visualization itself. Further studies are needed such that these limitations can be overcome. In essence, this study contributes to our understanding of how uncertainty visualization intertwines with neurosurgical decision-making. The findings underscore the need to consider uncertainty information as a valuable component in the decision-making process, yet also highlight the complex nature of clinical judgments, which are shaped by a multitude of factors. Future research could delve deeper into understanding participants' decision strategies and their ability to grasp and use the concept of uncertainty. Furthermore, the influence of the specific visualization technique in the decision-making process was out of the scope of our work, but would also be of interest for future work.

REFERENCES

[1] Ralph Brecheisen et al. "Illustrative uncertainty visualization of DTI fiber pathways". In: *The Visual Computer* 29.4 (2013), pp. 297–309.

[2] Stephanie Deitrick and Robert Edsall. "The influence of uncertainty visualization on decision making: An empirical evaluation". In: *Proceedings of International Symposium on Spatial Data Handling*. Springer. 2006, pp. 719–738. DOI: 10.1007/3-540-35589-8_45.

[3] Evanthia Dimara and John Stasko. "A Critical Reflection on Visualization Research: Where Do Decision Making Tasks Hide?" In: *IEEE Transactions on Visualization and Computer Graphics* 28.1 (Jan. 2022), pp. 1128–1138. DOI: 10.1109/tvcg.2021.3114813.

[4] Mirta Galesic, Rocio Garcia-Retamero, and Gerd Gigerenzer. "Using icon arrays to communicate medical risks: overcoming low numeracy." In: *Health psychology* 28.2 (2009), p. 210. DOI: 10.1037/a0014474.

[5] Christina Gillmann et al. "Uncertainty-aware Visualization in Medical Imaging-A Survey". In: *Computer Graphics Forum*. Vol. 40. 3. Wiley Online Library. 2021, pp. 665–689. DOI: 10.1111/cgf.14333.

[6] PC De Witt Hamer et al. “Impact of intraoperative stimulation brain mapping on glioma surgery outcome: a meta-analysis”. In: *J Clin Oncol* 30.20 (2012), pp. 2559–2565. DOI: 10.1200/JCO.2011.38.4818.

[7] Jessica Hullman. “Why authors don’t visualize uncertainty”. In: *IEEE Transactions on Visualization and Computer Graphics* 26.1 (2019), pp. 130–139. DOI: 10.1109/TVCG.2019.2934287.

[8] Jessica Hullman et al. “In pursuit of error: A survey of uncertainty visualization evaluation”. In: *IEEE Transactions on Visualization and Computer Graphics* 25.1 (2018), pp. 903–913. DOI: 10.1109/TVCG.2018.2864889.

[9] Susan L Joslyn and Jared E LeClerc. “Uncertainty forecasts improve weather-related decisions and attenuate the effects of forecast error.” In: *Journal of experimental psychology: applied* 18.1 (2012), p. 126. DOI: 10.1037/a0025185.

[10] Michelle Korporaal, Ian T Ruginski, and Sara Irina Fabrikant. “Effects of uncertainty visualization on map-based decision making under time pressure”. In: *Frontiers in Computer Science* 2 (2020), p. 32. DOI: 10.3389/fcomp.2020.00032.

[11] Michelle McDowell and Astrid Kause. “Communicating uncertainties about the effects of medical interventions using different display formats”. In: *Risk Analysis* 41.12 (2021), pp. 2220–2239. DOI: 10.1111/risa.13739.

[12] Susumu Mori et al. “Three-dimensional tracking of axonal projections in the brain by magnetic resonance imaging”. In: *Annals of Neurology: Official Journal of the American Neurological Association and the Child Neurology Society* 45.2 (1999), pp. 265–269.

[13] Lace M Padilla et al. “Decision making with visualizations: a cognitive framework across disciplines”. In: *Cognitive research: principles and implications* 3.1 (2018), pp. 1–25. DOI: 10.1186/s41235-018-0120-9.

[14] Lace MK Padilla et al. “Uncertain about uncertainty: How qualitative expressions of forecaster confidence impact decision-making with uncertainty visualizations”. In: *Frontiers in Psychology* 11 (2021), p. 579267. DOI: 10.3389/fpsyg.2020.579267.

[15] Maria H Ramos, Schalk J Van Andel, and Florian Pappenberger. “Do probabilistic forecasts lead to better decisions?” In: *Hydrology and Earth System Sciences* 17.6 (2013), pp. 2219–2232. DOI: 10.5194/hess-17-2219-2013.

[16] Mark S Roulston and Todd R Kaplan. “A laboratory-based study of understanding of uncertainty in 5-day site-specific temperature forecasts”. In: *Meteorological Applications: A journal of forecasting, practical applications, training techniques and modelling* 16.2 (2009), pp. 237–244. DOI: 10.1002/met.113.

[17] Mark S. Roulston et al. “A Laboratory Study of the Benefits of Including Uncertainty Information in Weather Forecasts”. In: *Weather and Forecasting* 21.1 (2006), pp. 116–122. DOI: 10.1175/WAF887.1.

[18] Geert-Jan M Rutten et al. “Executive functional deficits during electrical stimulation of the right frontal aslant tract”. In: *Brain Imaging and Behavior* 15.5 (2021), pp. 2731–2735. DOI: 10.1007/s11682-020-00439-8.

[19] Will Schroeder, Kenneth M Martin, and William E Lorensen. *The visualization toolkit an object-oriented approach to 3D graphics*. Prentice-Hall, Inc., 1998.

[20] Thomas Schultz and Anna Vilanova. “Diffusion MRI visualization”. In: *NMR in Biomedicine* (Jan. 2018), e3902–n/a. DOI: 10.1002/nbm.3902.

[21] Faizan Siddiqui, Thomas Höllt, and Anna Vilanova. “A Progressive Approach for Uncertainty Visualization in Diffusion Tensor Imaging”. In: *Computer Graphics Forum*. Vol. 40. 3. Wiley Online Library. 2021, pp. 411–422. DOI: 10.1111/cgf.14317.

8

CONCLUSION

This thesis focuses on advancing the understanding and practical application of uncertainty visualization in the DTI pipeline, with particular attention to its integration into neurosurgical workflows. In this chapter, we summarize our contribution (Section 8.1), and conclude with the future outlook (Section 8.2).

8.1. SUMMARY

The first three chapters of this thesis establish the clinical and technical background of DTI. We began by introducing the fundamental concepts of DTI, including its role in medical imaging and neurological applications. We then provided a detailed explanation of the DTI pipeline, covering each step from data acquisition, modeling, fiber tracking, and visualization.

In Chapter 4, we explore the sources and implications of uncertainty in the various stages of the DTI pipeline. We surveyed existing uncertainty modeling and visualization techniques, including those outside the diffusion-weighted imaging (DWI) domain. We identified a gap in clinical applicability, highlighting the need for uncertainty visualization techniques tailored to the clinical DTI pipeline. This analysis sets the stage for the development of interactive visualization strategies presented in subsequent chapters.

In Chapter 5, we introduced a progressive visual analytics framework for uncertainty visualization in the DTI pipeline that addresses interactive visualization and computational challenges. By integrating a local wild-bootstrapping approach with interactive fiber tracking, the framework facilitates real-time exploration of uncertainty, making it more accessible to clinicians. Although the feedback from clinical collaborators was encouraging, the chapter also acknowledged the challenges of integrating such tools into existing clinical workflows. This progressive framework marks a significant step toward bridging the gap between research and clinical practice, though further work was needed to evaluate its impact on decision-making processes, which we addressed in Chapter 7.

In Chapter 6, we present a solution to visualize the uncertainty that arises in the fiber tracking stage of the pipeline. This approach addresses the variability introduced by parameter selection during fiber tracking by providing users with information concerning parameter sensitivity that helps refine region of interest (ROI) boundaries. By incorporating sensitivity information, the framework reduces the need for repeated manual adjustments, improving both efficiency and accuracy. This chapter indicates the potential of sensitivity-based visualization to enhance clinical workflows, offering users intuitive means of navigating the complexities of ROI definition.

In Chapter 7, we designed a user study to analyze the influence of fiber tracking uncertainty visualization on neurosurgical decision-making for brain-tumor resection. The user study involving neurosurgeons indicated that uncertainty visualization encourages more cautious decision-making, particularly in cases with high uncertainty intervals. However, the findings also highlighted the complex nature of clinical judgments, which are shaped by factors such as fiber density and individual interpretation. This chapter contributes to how uncertainty visualization can support complex clinical decision.

8.2. CONCLUSION AND FUTURE OUTLOOK

Uncertainty visualization plays a crucial role in interpreting complex data by providing insights into its reliability and confidence. However, quantifying, communicating, and evaluating uncertainty remains challenging, particularly in medical applications, due to the complexity of the data and the interdisciplinary expertise required. This thesis has focused on developing and evaluating uncertainty visualization techniques for fiber tracking, based on diffusion tensor imaging (DTI), specifically tailored for neurosurgical workflows. While our work addresses some barriers to integrating uncertainty visualization into clinical practice, widespread adoption remains challenging and requires further research. Close collaboration between researchers and clinicians will be essential to refine these techniques, ensuring they align with clinical practice while maintaining usability and interpretability.

The interactive uncertainty visualization methods presented in this thesis have shown potential in supporting neurosurgical assessment and surgical planning by helping clinicians better understand the uncertainties involved in the results. However, additional research is needed to evaluate their practical applicability and effectiveness in real-world clinical settings. Moreover, clinical decision-making is a multifaceted process influenced by various factors, including patient history, physical condition, lesion characteristics, medication, intraoperative navigation, and surgical expertise. These factors often have a more direct impact on patient outcomes than fiber tracking results alone. As discussed in this thesis, isolating the specific contribution of uncertainty visualization to surgical decisions and patient recovery remains complex. Future research should explore how uncertainty visualization integrates with other decision-making factors to assess its broader clinical impact.

This research primarily focused on the computational aspects of uncertainty visualization rather than the development of new visual representations. The techniques and workflows developed in this thesis can be integrated into clinical practice using existing visualization methods. However, future research could explore the integration of more advanced visual representations to enhance the communication of uncertainty to neurosurgeons.

Like other studies on uncertainty visualization techniques in DTI, we have also presented the preoperative planning stage of the neurosurgical workflow as the primary application area. However, the presented methods could also be extended to intraoperative applications, such as tumor resection surgery. By visually conveying uncertainty information during the procedure, surgeons could assess the confidence levels associated with fiber tracking results, identify regions of potential ambiguity, and incorporate this knowledge into their decision-making process.

Additionally, more extensive validation studies are needed to assess the practical applicability of these methods in real-world clinical settings. Engaging neurosurgeons and other stakeholders in the evaluation process will be crucial to ensure that these techniques align with clinical needs and workflows. By addressing these challenges, future research can help bridge the gap between uncertainty visualization research and its practical application in neurosurgery, ultimately contributing to better-informed decision-making and improved patient outcomes.

ACKNOWLEDGEMENTS

What a journey it has been.

It all began in Istanbul, where I had just completed my master's thesis and was searching for PhD opportunities. I came across an advertisement that caught my attention and decided to apply. Little did I know that I was stepping into one of the most transformative and unforgettable journeys of my life.

From that very first *Skype* interview (Yes, pre-covid times) to this moment, writing the final words of my thesis, so much has changed. Over the course of my PhD, I moved cities, the world faced a global pandemic, I got married, I lost my father, and I became a parent.

Through all these highs and lows, one thing remained constant: the unwavering support from my supervisors and promotors, Anna and Thomas. I would like to express my deepest gratitude to you both. Thank you for your thoughtful suggestions, insightful feedback, and countless reviews. Thank you for keeping me on track and reigniting my motivation, especially during the more difficult final years. Most of all, thank you for believing in me.

Anna, your kindness, patience, and steady encouragement have been a source of strength throughout this journey. Your ability to listen, guide, and offer thoughtful advice made a profound difference. Your deep expertise in visualization, particularly in exploring innovative ways to represent complex data, has been both inspiring and instrumental in shaping my work. Your visionary approach to bridging fundamental visualization techniques with real-world applications, and your leadership in advancing the field, have provided me with a unique perspective on how impactful research can be.

Thomas, your critical eye, depth of knowledge, and meticulous attention to detail have pushed my work to a higher level. Your insightful questions, clear thinking, and dedication to research have been both inspiring and motivating.

To you both, thank you for your trust, your guidance, and the freedom you gave me throughout this journey.

Thank you, Elmar, for cultivating the CGV group into such a vibrant and supportive research environment. Your guidance, thoughtful comments, and continuous encouragement have been a real source of motivation for me. You are not only an excellent researcher but also a remarkable communicator. I am truly grateful for the opportunity to be part of your inspiring group.

I would also like to extend my heartfelt thanks to everyone involved in TTW project at TU/e and ETZ hospital. Special thanks to Prof. Luc for your support and guidance,! I have always appreciated your enthusiasm and your deep understanding of the intricate world of numbers and equations. Thank you for making me part of this meaningful collaboration.

A very special thank you to Dr. Geert-Jan and Dr. Bart. I'm deeply grateful for the opportunity you gave me to familiarize myself with the neurosurgical workflow. Your guidance, support, and patience in answering all my questions during this learning phase were truly invaluable. Thank you for your clinical input and expert feedback on my research papers. I also appreciate your efforts in connecting us with a broader network of neurosurgeons, which enabled us to evaluate the relevance and impact of our visualizations in real clinical scenarios. I will never forget the once-in-a-lifetime opportunity to witness a live tumor resection surgery, an experience that profoundly shaped my understanding of the clinical environment and the real-world challenges faced by users. Thanks Stephan, Rick, Maud and Lars for all the collaborations and discussions.

I am truly grateful to all the talented PhD colleagues and the faculty members in the Computer Graphics and Visualization (CGV) group at TU Delft. I would particularly like to thank Rafael for making the time to meet me in person in Eindhoven, for always remembering special occasions, and for encouraging me to keep going. Your kindness and motivation meant a lot — Thank you!

To my first office mate and now dear friend Marcos, thank you for enduring all my non-work-related ramblings and for all the shared laughs. Thanks also to Alex and Nicolas for our "reading group" sessions, which often turned into fun and thought-provoking discussions. And to Baran — one of my paranymphs — I fondly remember our deep conversations in the pre-COVID days.

About seven months into my PhD, Anna moved to Eindhoven and suggested I join her there, as most of my project collaborators were based at TU/e. Although I wasn't quite ready to relocate again, I'm so glad I did. It turned out to be one of the best decisions of my PhD journey.

At TU/e, I had the privilege of working with an amazing group of colleagues and faculty. Thank you to Jack, Andrei, Huub, Stef, Fernando, and Maxime for your guidance and insights throughout my PhD. A special thanks to Dennis and Bram — your humility, enthusiasm, and deep expertise were incredibly valuable. From Dutch integration to administrative hassles, to visualization topics, you were always there to help, and I can't thank you enough.

To my office mates Astrid and Kirsten, thank you for your positivity, and all the conversations that brightened up long office days. And to Sanne, Vidya, Linhao, Leonardo, and Tom — thank you for your energy and dedication. You all made work genuinely enjoyable.

During this journey, I've been fortunate to meet colleagues who became friends — and a few friends who became like family. Saher and Talqeeb, your support during my early days in the Netherlands meant the world to me. Thank you for your guidance, for helping me settle into a new country, and for making me feel at home away from home. I'll always cherish our late-night *chaye (tea) and biryani* sessions in your apartment, and the long walks through Delft's quiet streets. Thank you both — for everything.

I would like to thank my parents for their unconditional love and for trusting me enough to let me carve my own path. Your sacrifices, values, and encouragement laid the foundation for everything I've been able to achieve. To my father, I wish you were here to witness this moment. Your quiet strength, support, and belief in me continue to guide me, and this milestone is as much yours as it is mine.

To my wonderful siblings, Adnan, Sobia, and Anum, thank you for bearing with me through all the ups and downs, the video calls, the missed family events, and the endless "Weekend mai baat krte hain" (Lets talk in the weekend) replies. Your constant encouragement, humor, and presence, even from afar, have meant more to me than I can put into words. This one is for you all.

Finally, I would like to dedicate this work to the love of my life, my wife, Nusrah. Your unwavering support, patience, and love have been the anchor that kept me grounded through the highs and lows of this PhD journey. You've seen me at my best and, more often, at my most stressed-state, yet you stood by me with unwavering support. Your incredible social skills, optimism, and ability to connect with everyone around you have always inspired me, and, I must admit, you're the reason I even have a social life. Thank you for filling our home with laughter, for believing in me when I didn't, and for reminding me that there's more to life than simulations, writing and reading. I am endlessly grateful for you. You've been my partner, my strength, and my calm in the chaos. I couldn't have done this without you.

And to our son, Rayan, you may be too young to understand any of this right now, but your laughter, curiosity, and hugs have been my greatest source of light during the most stressful days. Watching you grow over these past two and a half years has put everything into perspective and reminded me of what truly matters. I look forward to the day you read this and realize that, in your own way, you helped me finish this thesis too.

"It is good to have an end to journey towards; but it is the journey that matters, in the end." — *Ursula K. Le Guin*

CURRICULUM VITÆ

Faizan Pervez SIDDIQUI

21-04-1991 Born in Karachi, Pakistan.

EDUCATION

2010–2014 Bachelor's Degree in Electronic Engineering
NED University of Engineering and Technology
Karachi, Pakistan

2016–2018 Master's Degree in Electrical and Electronic Engineering
Özyeğin University
Istanbul, Turkey
Thesis: Development of an accelerated Monte Carlo ray tracing based radiation heat transfer solver
Supervisor: Dr. A. Basol

2019–2023 PhD. in Data Visualization and Visual Analytics
Delft University of Technology
Delft, Netherlands
Thesis: Fiber tracking uncertainty visualization for neurosurgery
Supervisors: Prof. Dr. A. Vilanova
Dr. T. Höllt

AWARDS

2016 Best R&D project in International Aeronautics and Space Technology
AeroX 2016
Istanbul, Turkey

List of Publications

Publications in this dissertation

4. **Siddiqui, F.**, Brouwers, H. B., Rutten, G. J., Höllt, T., and Vilanova, A. (2024). Effect of white matter uncertainty visualization in neurosurgical decision making. IEEE Computer Graphics and Applications, vol. 45, no. 1, pp. 106-121. 2025. https://doi.org/10.1109/MCG.2024.3462926.

3. **Siddiqui, F.**, Höllt, T., and Vilanova, A. (2023). Interactive visual exploration of region-based sensitivities in fiber tracking. In Eurographics Workshop on Visual Computing for Biology and Medicine 2023, pp. 13-22. https://doi.org/10.2312/vcbm.20231208

2. **Siddiqui, F.**, Höllt, T., and Vilanova, A. (2021, June). A progressive approach for uncertainty visualization in diffusion tensor imaging. In Computer Graphics Forum, Vol. 40, No. 3, pp. 411-422. https://doi.org/10.1111/cgf.14317.

1. **Siddiqui, F.**, Höllt, T., and Vilanova, A. (2021). Uncertainty in the DTI Visualization Pipeline. In Anisotropy Across Fields and Scales, pp. 125-148. https://doi.org/10.1007/978-3-030-56215-1_6.

Other publications:

5. Poster: **Siddiqui, F.**, Höllt, T., Vilanova, A. (2022). Parameter Sensitivity and Uncertainty Visualization in DTI. In EuroVis 2022 - Posters, pp. 131-133. https://doi.org/10.2312/evp.20221138.

4. **Siddiqui, F.**, Meneksedag, K., Basol, A. M., Menguc, M. P. (2019). Segregated approach for the modeling of continuous heat treatment furnaces. In Proceedings of the 9th International Symposium on Radiative Transfer, RAD-19. Begell House Inc. pp 65-72. https://doi.org/10.1615/RAD-19.90.

3. **Siddiqui, F.**, Meneksedag, K., Basol, A. M., Mengüç, M. P. (2018). Combined radiation and conduction heat transfer solver on hybrid CPU-GPU architectures. In Proceedings of Eurotherm Seminar 110 - Computational Thermal Radiation in Participating Media -VI.

2. **Siddiqui, F.** , Basol, A. M., Menguc, M. P. (2016). Ray tracing on graphic processors: Towards high fidelity radiative transfer solvers. In Proceedings of the 8 th International Symposium on Radiative Transfer RAD-16. Begell House Inc. pp 236-243. https://doi.org/10.1615/RAD-16.290.

1. Göçer, Ö., Göçer, K., Başol, A. M., Kıraç, M. F., Özbil, A., Bakovic, M., **Siddiqui, F.** , Özcan, B. (2018). Introduction of a spatio-temporal mapping based POE method for outdoor spaces: Suburban university campus as a case study. Building and environment, vol. 145, pp. 125-139. https://doi.org/10.1016/j.buildenv.2018.09.012.